

Analytical approaches to physicochemical characterization of colloidal drug carriers

Dissertation

zur Erlangung des akademischen Grades
Doctor rerum naturalium (Dr. rer. nat.)

vorgelegt der

Naturwissenschaftlichen Fakultät I - Biowissenschaften
der Martin-Luther-Universität Halle-Wittenberg

von

Herrn Mustafa Mohammed Abdelaziz Elsayed
geboren am 13.07.1981 in Alexandria, Ägypten

Gutachter /in

1. Prof. Dr. Dr. Reinhard Neubert
2. Prof. Dr. Gregor Cevc
3. Prof. Dr. Alfred Blume

Halle (Saale), Tag der Verteidigung: 26.05.2011

Analytical approaches to physicochemical characterization of colloidal drug carriers

Dissertation

for attainment of the academic degree of
Doctor of natural science (Dr. rer. nat.)

Submitted to

Faculty of Natural Science I - Biological Science
Martin Luther University Halle-Wittenberg

by

Mustafa Mohammed Abdelaziz Elsayed

born on 13.07.1981 in Alexandria, Egypt

Examiners

1. Prof. Dr. Dr. Reinhard Neubert
2. Prof. Dr. Gregor Cevc
3. Prof. Dr. Alfred Blume

Halle (Saale), date of defense: 26.05.2011

وَقُلْ رَبِّ زِدْنِي عِلْمًا

سورة طه: الآية ١١٤

“And say: My Lord! Increase me in knowledge”

Holy Quran 14:114 (English translation)

TABLE OF CONTENTS

Table of contents	i
1 Introduction and Objectives	01
1.1 Biomedical applications of colloidal aggregates	03
1.1.1 Drug delivery	03
1.1.2 Therapeutic techniques	04
1.1.3 In vivo imaging	07
1.1.4 Biomaterials and tissue engineering	07
1.2 Key characteristics of colloidal drug carriers.....	07
1.2.1 Size and size distribution	07
1.2.2 Surface charge	08
1.2.3 Surface hydrophobicity	08
1.2.4 Lamellarity (lipid bilayer vesicles)	09
1.2.5 Lipid composition (lipid bilayer vesicles)	09
1.2.6 Structure and crystallinity	09
1.3 Objectives and structure of the thesis	10
2 Accurate potentiometric determination of lipid membrane-water partition coefficients and apparent dissociation constants of ionizable drugs: Electrostatic corrections	12
2.1 Introduction	13
2.2 Materials and Methods	15
2.2.1 Materials	15
2.2.2 Preparation of the liposomes	15
2.2.3 Potentiometric titration measurements	16
2.2.4 Potentiometric data analysis	16
2.3 Theoretical considerations	17
2.4 Results and Discussion	22
2.5 Experimental recommendations	29
2.6 Conclusions	30
Appendix 2.A	30
3 The vesicle-to-micelle transformation of phospholipid-cholate	

mixed aggregates: A state of the art analysis including membrane curvature effects	34
3.1 Introduction	35
3.2 Materials and Methods	36
3.2.1 Materials	36
3.2.2 Preparation of lipid vesicles	37
3.2.3 Preparation of samples	37
3.2.4 The static light scattering (turbidimetry)	38
3.2.5 The dynamic light scattering (photon correlation spectroscopy)	38
3.2.6 Data analysis	39
3.3 Results	39
3.3.1 The quasi-steady state light scattering	39
3.3.2 The time-resolved light scattering	44
3.3.3 Quantitative analysis of the cholate-facilitated bilayer fluctuations	45
3.4 Discussion	47
3.4.1 Experimental considerations	47
3.4.2 Supramolecular view of the vesicle-to-micelle transformation	49
3.5 Conclusions	57
Appendix 3.A	59
Appendix 3.B	62
Appendix 3.C	64
4 Turbidity spectroscopy for characterization of submicroscopic drug carriers, such as nanoparticles and small lipid vesicles	66
4.1 Introduction	67
4.2 Theory	69
4.2.1 Description of a light scattering particle suspension	69
4.2.2 Theory of light scattering	70
4.2.3 Size-distribution	73
4.3 Materials and Methods	74
4.3.1 Materials	74
4.3.2 Preparation of lipid vesicles	74
4.3.3 Monitoring effect of cholate on lipid vesicles	75
4.3.4 Turbidity/optical density measurements	76

4.3.5	Dynamic light scattering (photon correlation spectroscopy)	76
4.4	Results and Discussion	77
4.4.1	Characteristics affecting turbidity of a nanosized particle suspension	77
4.4.2	Characterization of real lipid vesicle suspensions	86
4.4.3	Monitoring small size changes	89
4.4.4	Experimental recommendations and limitations	89
4.5	Conclusions	91
	Appendix 4.A	92
	Appendix 4.B	93
	Appendix 4.C	94
5	Summary	96
6	Zusammenfassung	99
7	References	103
	List of Tables	120
	List of Figures	121
	Erklärung	124
	Acknowledgement	125
	Curriculum Vitae	126
	List of Publications	127

1 Introduction and Objectives

Contents

1.1	Biomedical applications of colloidal aggregates	03
1.1.1	Drug delivery	03
1.1.2	Therapeutic techniques	04
1.1.3	In vivo imaging	07
1.1.4	Biomaterials and tissue engineering	07
1.2.	Key characteristics of colloidal drug carriers.....	07
1.2.1	Size and size distribution	07
1.2.2	Surface charge	08
1.2.3	Surface hydrophobicity	08
1.2.4	Lamellarity (lipid bilayer vesicles)	09
1.2.5	Lipid composition (lipid bilayer vesicles)	09
1.2.6	Structure and crystallinity	09
1.3	Objectives and structure of the thesis	10

Fast developing nanotechnology is expected to have a dramatic impact on medicine. In the late 1990s the term “nanomedicine”, referring to applications of nanotechnology in medicine, has emerged. The nanomedicine field, in its wide context, encompasses several varieties of molecular and supramolecular, nanoscale or nanostructured materials/objects/devices. With the recent advances in nanotechnology, nanomedicine applications currently include, but are not limited to, drug and protein delivery, gene therapy, in vitro diagnostics, in vivo imaging, therapeutic techniques, biomaterials, and tissue engineering^[1, 2].

Nanomedicines are expected to elicit significant therapeutic benefits. The number of articles and patents published in the field has been exponentially increasing since 2000^[3]. So far, there are over two dozen nanotechnology-based therapeutic products approved for clinical use, and more are in clinical trials^[1, 4]. Drug delivery applications dominate, accounting for three-quarters of the research activity in the field and of the market^[1]. A market analysis published by NanoMarkets in 2005 suggested that colloidal, nano-sized drug delivery systems will generate over \$4.8 billion in 2012^[5]. A more recent report, published in 2007 by Cientifica Ltd., suggested that this market reached \$3.39 billion in 2007, will reach \$26 billion by 2012, and could steeply rise after 2012, reaching potentially \$220 billion by 2015^[6].

Among approaches exploiting nanotechnology developments in medicine, the nanostructured colloidal drug carriers have attracted growing attention. Several varieties of colloidal carriers have been designed, explored, and investigated for their biomedical applications during the past few decades^[7-9] (Fig. 1.1). Lipid bilayer vesicles (liposomes)^[10, 11], polymeric micelles^[12], dendrimers^[13, 14], solid lipid nanoparticles^[15, 16], microemulsions^[17], and nanoemulsions^[18-20] are the most extensively studied examples.

The growing biomedical interest in colloidal carriers raises the need for development of advanced characterization approaches to assist in product development processes. Understanding physical and physicochemical properties of such aggregates allows carrier design, formulation development, and process troubleshooting to be carried out in a rational fashion. The pharmaceutical research industry is still in crucial need of reliable characterization techniques that routinely provide detailed information about such carriers and that are also simple and inexpensive. Lack of physicochemical characterization techniques that are acceptable to the regulatory authorities can critically delay product registration and introduction into the market.

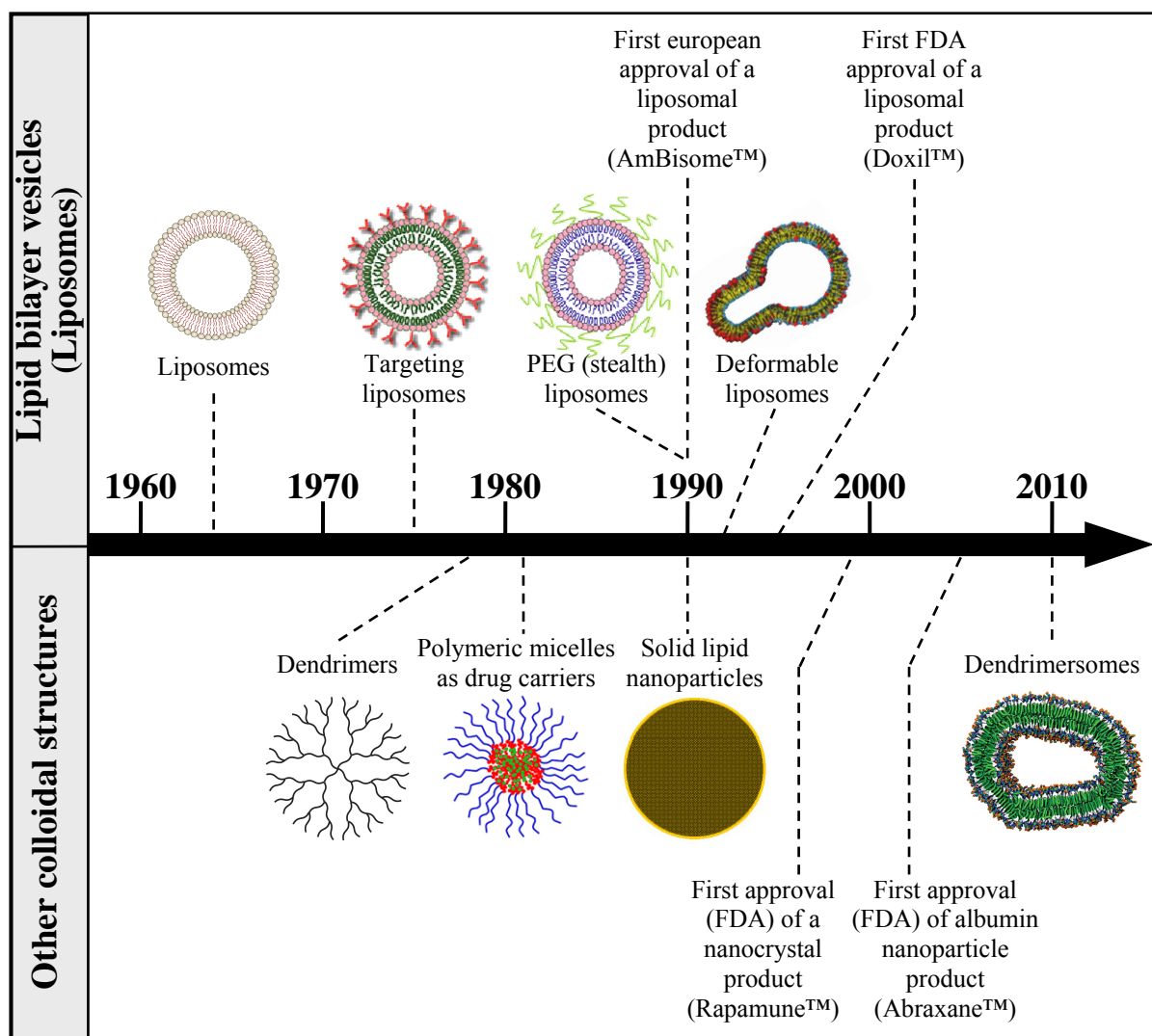


Figure 1.1 Development of selected colloidal aggregates of pharmaceutical interest as drug delivery carriers over the past five decades. Assigned dates refer to the first published report describing (invention of) the colloidal structure or the specified application.

The next introductory sections briefly review several pertinent nanotechnology biomedical applications and the key characteristics of the colloidal structures involved. Subsequently, the objectives and the organization of this thesis are defined.

1.1 Biomedical applications of colloidal aggregates

1.1.1 Drug delivery

Colloidal carriers can enhance *in vivo* therapeutic efficiency of drugs. More specifically, they can be used to: *i*) improve drug bioavailability and pharmacokinetics (for this purpose, carriers can be designed to improve dissolution of poorly soluble drugs, to release drug in a sustained or stimulus-triggered fashion, or to prolong circulation time, e.g.

using protective PEG coating ^[21]); *ii*) enhance drug accumulation in pathological areas (for example, surface-attached specific ligands, e.g. monoclonal antibodies, can enable drug carriers to recognize and bind to a target tissue or a specific kind of cells ^[22, 23]; furthermore, pH- or temperature-sensitive polymers can make carriers responsive to local stimulus specific to the targeted pathological site, e.g. a lower pH or higher temperature at the diseased site triggers the entrapped drug release ^[24]; *iii*) prevent undesirable side effects (for example, passive or active targeting can reduce drug burden on a healthy tissue); and *iv*) minimize in vivo drug degradation (carriers can protect drug from premature degradation/metabolism). Several therapeutic products that rely on colloidal carriers for drug delivery are approved for clinical use (Table 1.1) and many more are under development.

1.1.2 Therapeutic techniques

Certain colloidal particles have unique therapeutic properties allowing direct use for treating diseases. Hafnium oxide and gold nanoparticles, for example, can greatly enhance X-ray cancer therapy ^[25]. Such particles enhance electromagnetic radiation absorption and thus promote localized damage to DNA or other cellular structures.

Nanoparticle-mediated hyperthermia ^[26] is a new and minimally invasive tool for cancer treatment. The technique involves direct injection of special metal nanoparticles into tumours (or more elegantly using particles that preferentially accumulate in tumours, either passively or via active targeting, following systemic administration). When appropriate electromagnetic stimulation is then applied, such particles generate heat. Antitumour effects of hyperthermia include induction of apoptosis, activation of immunological processes, and enhancing effectiveness of other conventional treatments, such as radiotherapy and chemotherapy. The technique most commonly employs magnetic nanoparticles, gold nanoparticles, or carbon nanotubes. Magnetic nanoparticles generate heat when subjected to an oscillating magnetic field. Gold nanoparticles generate hyperthermia via light absorption. The characteristic extinction spectrum of gold nanoparticles can be tuned by adjusting particle structure. Gold nanoshells/nanorods, for example, have an absorption peak in the near-infrared (NIR) region; this allows hyperthermia induction within deep tumors. Carbon nanotubes can likewise generate local hyperthermia after NIR light absorption.

Nano-Cancer (Nanostart AG, Germany) was approved for medical use in the European Union in June 2010 and thus became the world's first nanoparticle-based cancer treatment. The therapy relies on magnetic nanoparticle (iron oxide) mediated hyperthermia.

Table 1.1 Selected marketing authorization holding therapeutics employing colloidal carriers for drug delivery ^{a,b}.

Trade name ^c	Composition/ Colloidal structure	Route of administration	Indication	Company/ Alliance ^d	Approval date
Lipid bilayer vesicles (liposomes)					
Ambisome	Amphotericin B liposomes	Intravenous infusion	Fungal infections	Gilead Sciences, Inc. (CA, USA)	1990 (Europe) 1997 (FDA)
Caelyx Doxil	Doxorubicin HCl pegylated liposomes	Intravenous infusion	Cancer, Kaposi sarcoma	Ortho Biotech Products, LP (NJ, USA); Janssen (Belgium)	1996 (Europe) 1995 (FDA)
DepoCyte Depocyt	Cytarabine liposomes	Intrathecal	Lymphomatous meningitis	Pacira Pharmaceuticals, Inc. (CA, USA); Sigma-Tau Pharmaceuticals, Inc. (MD, USA); Mundipharma International Ltd. (UK)	2001 (Europe) 1999 (FDA)
DepoDur	Morphine sulfate liposomes	Lumbar epidural	Analgesia (post-surgical pain)	Pacira Pharmaceuticals, Inc. (CA, USA); EKR Therapeutics, Inc. (NJ, USA); Flynn Pharma (UK)	2006 (Europe) ^{e,f} 2004 (FDA)
DaunoXome	Daunorubicin citrate liposomes	Intravenous infusion	Kaposi sarcoma	Diatos S.A. (France)	1996 (Europe) ^e 1996 (FDA)
Myocet	Doxorubicin citrate liposomes	Intravenous infusion	Metastatic breast cancer	Cephalon, Inc. (PA, USA); Sopherion Therapeutics, LLC (NJ, USA)	2000 (Europe) 2001 (Canada) Not yet (FDA)
Visudyne	Verteporfin liposomes	Intravenous infusion followed by photoactivation	Predominantly classic subfoveal choroidal neovascularization	Novartis AG (Switzerland); QLT, Inc. (BC, Canada)	2000 (Europe) 2000 (FDA)
Virosomes					
Epaxal HAVpur VIROHEP-A	Hepatitis A vaccine virosomes	Intramuscular	Hepatitis A vaccine	Crucell (Netherlands)	1994 ^g
Inflexal V InfectoVac Flu Isiflu V Viroflu	Influenza (subunit) vaccine virosomes	Intramuscular/ deep subcutaneous	Influenza vaccine	Crucell (Netherlands)	1997 ^h
Lipid complexes					
Abelcet	Amphotericin B lipid complex	Intravenous infusion	Fungal infections	Sigma-Tau Pharmaceuticals, Inc. (MD, USA); Cephalon (UK)	1995 (Europe) ^e 1995 (FDA)
Amphocil Amphotec	amphotericin B-cholesteryl sulfate complex	Intravenous infusion	Fungal infections	Three Rivers Pharmaceuticals, LLC, (PA, USA)	1994 (Europe) ^e 1996 (FDA)
Mixed micelles					
Konakion MM	Phytomenadione in glycocholic acid- lecithin mixed micelles	Oral/ intramuscular/ intravenous	Vitamin K deficiency bleeding	Roche (Switzerland)	-- ⁱ
Valium MM	Diazepam in glycocholic acid- lecithin mixed micelles	Intravenous	Anxiolytic/ sedative	Roche (Switzerland)	-- ⁱ

Nanocrystals					
Emend	Aprepitant nanocrystals	Oral	Nausea and vomiting associated with cancer chemotherapy	Merck Sharp & Dohme Corp. (NJ, USA)	2003 (Europe) 2003 (FDA)
Megace ES	Megestrol acetate nanocrystals	Oral	Anorexia or cachexia in AIDS patients	Par Pharmaceutical Companies, Inc. (NY, USA)	2005 (FDA)
Rapamune	Sirolimus nanocrystals	Oral	Organ rejection in kidney transplant (immunosuppressive)	Wyeth Pharmaceuticals Inc. (PA, USA)	2002 (Europe) 2000 (FDA)
Tricor	Fenofibrate nanocrystals	Oral	Hypercholesterolemia/hypertriglyceridemia	Abbott Laboratories (IL, USA)	2004 (FDA)
Triglide	Fenofibrate nanocrystals	Oral	Hypercholesterolemia/hypertriglyceridemia	Shionogi Pharma, Inc. (NJ, USA); SkyePharma PLC (UK)	2005 (FDA)
Invega Sustenna	Paliperidone palmitate nanocrystals	Intramuscular	Schizophrenia (antipsychotic)	Janssen (NJ, USA)	2009 (FDA)
Albumin nanoparticles					
Abraxane	paclitaxel albumin-bound nanoparticles	Intravenous infusion	Breast cancer	Celgene (NJ, USA)	2008 (Europe) 2005 (FDA)

^a The table focuses only on products employing colloidal structures as drug delivery carriers. Clinically approved products employing nanotechnology-based colloidal structures for other biomedical applications ^[1] are not included.

^b Marketing authorization does not necessarily indicate that the product is in the market.

^c Multiple trade names are given when a product is marketed in different countries under different trade names.

^d Current name of developing company and/or current license/marketing authorization holder/s.

^e Product approved for clinical use in European countries following a decentralized/multi-state approval procedure.

^f Only in the UK.

^g Epaxal was first launched in Switzerland in 1994. It is currently licensed in more than 40 countries.

^h Inflexal V was first introduced to the Swiss market in 1997. It is currently approved in 43 countries.

ⁱ Reliable information about approval date was not available.

Table 1.2 Key characteristics of colloidal drug carriers.

Characteristic	Analytical techniques
Size, size distribution, and morphology	Transmission electron microscopy, scanning electron microscopy, atomic force microscopy Dynamic light scattering ^[27-29] , static light scattering Small-angle X-ray scattering, small-angle neutron scattering ^[30-35] Field flow fractionation, size exclusion chromatography
Surface charge and zeta potential	Electrophoretic light scattering ^[36] Electroacoustic techniques ^[37, 38]
Surface hydrophobicity	Hydrophobic interaction chromatography ^[39, 40] Adsorption of Rose Bengal (a hydrophobic dye) ^[41]
Lamellarity (liposomes)	³¹ P NMR ^[42, 43] Fluorescence of NBD (7-nitro-2,1,3-benzoxadiazol-4-yl) labeled lipid ^[43] Small-angle X-ray scattering, small-angle neutron scattering
Structure and crystallinity	Differential scanning calorimetry X-ray scattering Infrared and Raman spectroscopy
Density	Isopycnic centrifugation

1.1.3 *In vivo* imaging

Recently developed colloidal probes/contrast agents, particularly for magnetic resonance imaging (e.g. magnetic nanoparticles ^[44]), ultrasound (e.g. carbon nanotubes ^[45]), and NIR fluorescence imaging (e.g. quantum dots ^[46, 47]), have been shown to provide high resolution, sensitivity, specificity, and reliability. Such probes thus enable early diagnosis of a disease and monitoring of its progression. They can also help surgeons to locate tumors and their margins, to identify important adjacent structures, and to map sentinel lymph nodes. Tracking colloidal carrier biodistribution is another promising application. Combining diagnostic/imaging and therapeutic functions into a single, clinically effective, formulation is further development target. This “find, fight, and follow” concept (early diagnosis, therapy, and follow-up), recently coined as nanotheranostics, will boost nanomedicine developments ^[48, 49].

The first approved colloidal contrast agent is Lumirem (ferumoxsil; marketed in USA as Gastromark). Lumirem is an aqueous suspension of silicone coated superparamagnetic iron oxide indicated for oral administration as a magnetic resonance imaging contrast medium. It was approved in 1993 in Europe and in 1996 in the United States of America.

1.1.4 Biomaterials and tissue engineering

Nanomaterials can improve mechanical properties and biocompatibility of biomaterials for medical implants, such as dental restoratives and bone substitutes. Nanocoatings can improve biocompatibility and adhesion of biomaterials. Recent advances in nanotechnology enable design and fabrication of biocompatible scaffolds, which can control spatiotemporal release of biological factors, resembling native extracellular matrix, to direct cellular behavior ^[2, 50].

1.2 Key characteristics of colloidal drug carriers

Understanding physical and physicochemical properties of colloidal drug carriers is a key prerequisite for rational development and use. Characteristics, such as size and size distribution, morphology, surface properties, lamellarity (for lipid vesicles), and drug encapsulation efficiency influence pharmaceutical applications of such carriers (Table 1.2).

1.2.1 Size and size distribution

Size and size distribution are the main parameters controlling performance of a colloidal drug carrier. Size influences colloidal carrier distribution, toxicity, and *in vivo* drug

release ^[51, 52]. Size control is crucial to safety, especially for intravenous systems. An overview of the analytical techniques used for size characterization of colloidal carriers is given in Chapter 4 introduction.

1.2.2 Surface charge

Surface charge is another key property influencing both physical stability and *in vivo* performance of colloidal carriers ^[36]. Surface charge of colloidal particles affects their clearance from circulation and their tissue disposition. It can also affect performance and disposition of colloidal particles after topical application ^[53, 54]. In the pharmaceutical field, zeta potential is commonly used as an indicator of surface charge. Zeta potential is defined as the electrostatic potential at the slipping plane of the interfacial electric double layer. In other words, it is the potential difference between the dispersion medium and the stationary layer of fluid firmly associated with the dispersed particle. Zeta potential serves as an important parameter in characterizing the electrostatic interaction between particles in dispersed systems. Some researchers therefore use zeta potential as a proxy for electrostatic interaction between particles, which is not generally justified, however.

Zeta potential is commonly determined ^[36] with electrophoresis, in which electrophoretic mobility of particles in an electric field is measured. Electrostatic theory links the resulting electrophoretic mobility with the moving particle zeta potential. The most common experimental electrophoretic technique used to determine zeta potential of colloidal carriers is electrophoretic light scattering, which is based on dynamic light scattering. Electrophoresis usually requires sample dilution, which might affect the tested sample properties. Electroacoustics is another option ^[37, 38], which has the advantage of requiring no dilution.

1.2.3 Surface hydrophobicity

Surface hydrophobicity can also influence physical stability as well as *in vivo* distribution of colloidal carriers. For example, amount and composition of plasma proteins adsorbing on particle surface after intravenous administration is affected by surface hydrophobicity ^[41]. Such proteins might then function as opsonins or dysopsonins, controlling the particle *in vivo* disposition and clearance from the circulation ^[40]. Surface hydrophobicity is most commonly characterized using hydrophobic interaction chromatography ^[39, 40] or Rose Bengal (a hydrophobic dye) adsorption ^[41].

1.2.4 Lamellarity (lipid bilayer vesicles)

Lamellarity of lipid bilayer vesicles often crucially influences drug release. Lamellarity also controls encapsulation efficiency. It plays an important role for ultradeformable lipid vesicles as skin drug-delivery vehicles; oligolamellarity reduces bilayer deformability and thus adversely influences therapeutic performance of such carriers. Moreover, only unilamellar vesicles provide good biological membrane models.

Several methods are available for determination of vesicle lamellarity^[43, 55]. They mostly depend on monitoring change in a signal, originating from lipid molecules, upon addition of a reagent that interacts only with lipid molecules exposed to the external aqueous phase. The signal may originate from a native lipid component, e.g. the ³¹P NMR signal from phospholipids, which is quenched or shifted by paramagnetic ions, such as Mn²⁺^[42]. The signal may alternatively originate from a marker lipid incorporated into lipid bilayers, e.g. fluorescence of NBD (*N*-(7-nitrobenz-2-oxa-1,3-diazol-4-yl))-labeled lipids, which is quenched by reducing agents, such as sodium dithionite^[55]. The degree of lamellarity is determined from the signal ratio before and after addition of the appropriate reagent. Other techniques, such as the small-angle neutron^[56] and X-ray^[57] scattering, can be also employed for the purpose.

1.2.5 Lipid composition (lipid bilayer vesicles)

Lipid composition affects bilayer fluidity (or rigidity) and permeability. Inclusion of phospholipids with long, saturated acyl chains or cholesterol, for example, reduces bilayer fluidity. In contrast, inclusion of bilayer perturbing amphiphats, which favour aggregates with a high radius of curvature, enhances bilayer fluidity. Bilayer composition and rigidity affect carrier distribution, pharmacokinetics, toxicity, and drug release^[52]. Ultradeformable lipid vesicles (Transfersomes®) are vesicles comprising a minimum of two amphiphiles with different packing characteristics, usually a bilayer former, such as a double-chain phospholipid, and a single-chain amphiphat, such as a surfactant (an edge activator). The resulting vesicles are therefore sufficiently deformable to pass even through pores appreciably smaller than their own size; this allows them to act as carriers for skin delivery of drugs.

1.2.6 Structure and crystallinity

Lipid crystallinity in solid lipid nanoparticles is strongly correlated with drug incorporation and release rates^[16, 58]. Gains in lipid crystallinity, during production or during

long-term storage, lead to drug expulsion, causing a burst effect. Differential scanning calorimetry and X-ray scattering are widely used to check lipid crystallinity.

1.3 Objectives and structure of the thesis

The main objectives of the present thesis are to improve the understanding of physicochemical interactions in complex colloidal systems and to develop simple characterization techniques useful in colloidal carrier product development. The investigations employ mainly, but are not limited to, lipid bilayer vesicles as exemplary colloidal drug carriers.

The thesis is organized in three independent chapters, which are, nevertheless, interrelated with regard to the objectives of this work. Each chapter starts with a short introduction, followed by theoretical background and an experimental section that describes used material and methods. The results are thereafter presented, illustrated, and discussed in sufficient detail to highlight importance and applications of the individual findings.

Chapter 2 aims mainly at improving understanding of potentiometric titrations in complex biphasic systems. It advances the potentiometric partition coefficient determination method by developing an improved analytical approach which takes Coulombic electrostatic interactions into account. The resulting improved method is valuable for reliable assessment of drug association with colloidal aggregates, such as lipid bilayer vesicles, mixed micelles, micro-, and nano-emulsions, in suspension. The improved method is moreover applicable for characterization of ionized drug lipophilicity using phospholipid bilayers as model biological membranes.

Chapter 3 revisits vesicle-to-micelle transformation in phosphatidylcholine–cholate mixtures paying special attention to the lipid bilayer curvature effects. Several colloidal drug carriers, such as mixed micelles (e.g. Konakion® MM, Valium® MM) and ultradeformable lipid vesicles, are composed of phosphatidylcholine-bile salt mixtures. The transformation process also forms the basis for various biomedical applications ^[59-62]. Investigations described in Chapter 3 are thus both fundamentally and practically worthwhile. In Chapter 3 the transformation process is studied with static and dynamic light scattering. Measurements were quantitatively analyzed using various analytical approaches. The result is a refined and generalized picture of vesicle-to-micelle transformation.

Chapter 4 deals with UV/Vis spectrometry as a means for characterization of colloidal

carriers, relying on the Rayleigh-Gans-Debye approximation. Chapter 4 first scrutinizes the theoretical background of the method and discusses its value and limitations. It studies effects of colloidal suspension characteristics on turbidity spectra and provides all equations necessary for extracting the most relevant characteristics from such spectra. It illustrates the advocated analytical method using suspensions of lipid bilayer vesicles, addressing also bilayer thickness and lamellarity effects on turbidity spectra.

2 Accurate potentiometric determination of lipid membrane-water partition coefficients and apparent dissociation constants of ionizable drugs: Electrostatic corrections*

Contents

2.1	Introduction	13
2.2	Materials and Methods	15
2.2.1	Materials	15
2.2.2	Preparation of the liposomes	15
2.2.3	Potentiometric titration measurements	16
2.2.4	Potentiometric data analysis	16
2.3	Theoretical considerations	17
2.4	Results and Discussion	22
2.5	Experimental recommendations	29
2.6	Conclusions	30
	Appendix 2.A	30

* This chapter was published as: M.M.A. Elsayed, U. Vierl, G. Cevc. Accurate potentiometric determination of lipid membrane-water partition coefficients and apparent dissociation constants of ionizable drugs: Electrostatic corrections. Pharm. Res. 26 (2009) 1332-1343.

2.1 Introduction

Lipophilicity and ionization are key physicochemical characteristics that control bioavailability and pharmacokinetics of drugs. They often play an important role in the pharmacodynamics of drugs, as well. They are influential in some analytical studies, e.g. reverse-phase chromatography, where they influence drugs retention by the matrix.

Traditionally, drug lipophilicity was characterized by studying the partitioning between octanol and water. Expressed in terms of partition coefficient, $P_{o/w}$, such lipophilicity parameter was then correlated with the drugs pharmacokinetics and pharmacodynamics. The octanol-water partition coefficients may be misleading, however. Octanol is a medium with a low dielectric constant, which can only model the hydrophobic molecular interactions. Biological membranes have more complex structure and interact with drugs through more diverse mechanisms, including hydrogen bonding and electrostatic interactions. Octanol thus favors partitioning of the neutral form of ionizable drugs and underestimates partitioning of the ionized drug forms. Phospholipid bilayer membranes, preferably in the form of biomimetic phospholipid bilayer vesicles (liposomes), were therefore introduced as a better model than octanol to study biologically relevant drug partitioning^[63-66].

Several methods are available to study drug association with lipid membranes or lipid membrane-water partition coefficients, $P_{mem/w}$. Potentiometric titration^[67-69], ultrafiltration^[64, 66], equilibrium dialysis^[70, 71], spectroscopy^[72-74], isothermal titration calorimetry^[75], and immobilized-liposome chromatography^[68, 76, 77] are particularly popular, but other methods can be used as well^[78-80].

Due to its experimental simplicity, the potentiometric titration method has gained special interest. The method employs a two-phase titration approach (Fig. 2.1). First, the test substance is titrated in an aqueous solution against a standard acid or base, to deduce the drug aqueous ionization/dissociation constant, expressed as pK_a . Second, the titration is repeated in presence of a second compartment (e.g. lipid membranes). A minimum of two titrations with different organic-aqueous compartment volumes ratios are needed. They yield apparent dissociation constants, pK_a^{app} , that differ from the aqueous pK_a as a function of the employed organic-aqueous compartment volumes ratio (Figs. 2.1–2.2). From the difference $\Delta pK_a = pK_a^{app} - pK_a$ one can calculate the partition coefficient of the neutral, P^N , as well as the ionized, P^I , test substance forms^[67, 69]. Simultaneously, one can also calculate the test substance dissociation constant in the membrane, pK_a^{mem} .

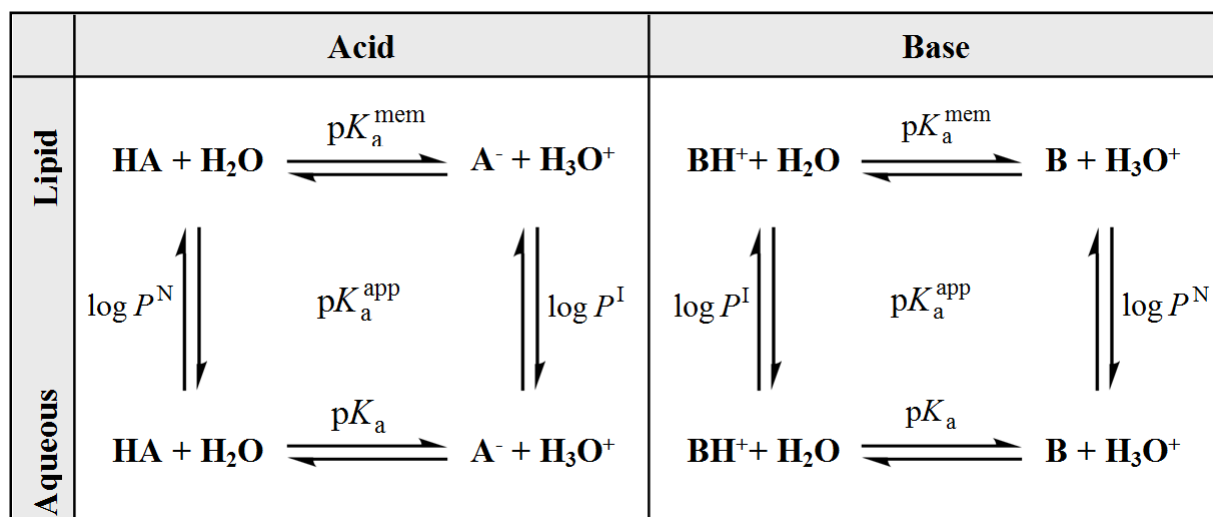


Figure 2.1 Schematic illustration of dissociation and partitioning equilibria for acids and bases in a lipid membrane-water system.

The potentiometric titration method has many advantages. It requires no phase separation, a time consuming process that can disturb the equilibrium state of samples [72, 81]. It can be used over a wide range of partition coefficients. It affords complete lipophilicity profiles of ionizable drugs in the partition system, since being a continuous method (as opposed to the point-by-point methods, such as dialysis). Gaining information on the apparent dissociation constant of the drug in the membrane, in addition to the partition coefficients, is attractive as well. The method gained popularity with the introduction of Sirius pH-metric $\log P$ titration equipment, which includes analytical software (Sirius Analytical Instruments Ltd., United Kingdom). It is equally possible, however, to use any common titrator or a simple pH-meter to get the necessary experimental data, if one can write an own analytical program.

Interpretation of potentiometric titration results must be done with utmost prudence. Incorporation of an ionized drug into a neutral phospholipid membrane charges-up the membrane (or modifies the membrane's surface charge density, if the membrane is intrinsically charged). This hinders further drug incorporation and affects the observed drug distribution [66, 68, 82] and pK_a^{app} . Potentiometrically determined P^{I} values of different organic acids and bases were thus somewhat smaller than the corresponding values determined with alternative methods [68]. The assumption that P^{I} is constant over the employed range of lipid-aqueous compartment volumes ratios (Eq. 2.3) is therefore also inevitably inaccurate. As a consequence, the published uncorrected P^{I} values, derived potentiometrically, are often doubtful. The corresponding P^{N} values are usually more reliable as they are not directly affected by electrostatic interactions, which cause the P^{I} variability (when P^{N} is close to P^{I} ,

the wrong assumption of a constant P^I can also affect the calculated P^N value, as the two parameters are typically derived simultaneously from the same data set).

The aim of this work was to improve the understanding of potentiometric titrations in complex systems and to progress the potentiometric partition coefficient determination by developing an improved analytical approach. We specifically intended to improve the method reliability by taking Coulombic electrostatic interactions into account. This should deliver intrinsic P_0^N and P_0^I values rather than experiment conditions dependent apparent P^N and P^I values. To the effect, we potentiometrically studied the partitioning of four ionizable drugs, the cationic bupivacaine and terbinafine and the anionic diclofenac and ketoprofen, into neutral, phosphatidylcholine, and/or negatively charged, mixed phosphatidylcholine-phosphatidylglycerol, bilayer membranes.

2.2 Materials and Methods

2.2.1 Materials

We obtained soybean phosphatidylcholine (SPC, Lipoid S 100, purity > 95%, the assumed average molecular weight \sim 800 g/mol) from Lipoid GmbH (Ludwigshafen, Germany). The sodium salt of 1,2-dimyristoyl-*sn*-glycero-3-phosphoglycerol (DMPG, Na, purity > 99.5%, molecular weight = 688.86 g/mol) was from Genzyme Pharmaceuticals (Liestal, Switzerland). Bupivacaine hydrochloride monohydrate was purchased from Heumann PCS GmbH (Feucht, Germany), diclofenac sodium from Fagron GmbH & Co. KG (Barsbüttel, Germany), ketoprofen from Bidachem (Fornovo S. Giovanni, Italy), and terbinafine hydrochloride from Amino Chemicals Ltd. (Marsa, Malta). All were of pharmaceutical quality. All other chemicals and reagents were of analytical grade.

2.2.2 Preparation of the liposomes

We prepared large unilamellar vesicles (LUV) by extrusion. In brief, we dissolved the selected lipids (SPC for the neutral membranes or SPC/DMPG⁻ (93.36/6.74 mol/mol) for the negatively charged membranes) in chloroform (SPC) or 3/1 v/v chloroform/methanol mixture (SPC/ DMPG-) in a 500 mL round-bottom flask. Vacuum evaporation of solvents at 50 °C in a rotary evaporator yielded a thin lipid film, which we hydrated at the same temperature with 150 mM aqueous sodium chloride solution. This produced multilamellar vesicles (MLV) suspension with a total phospholipid concentration of 120 mg/mL. We then prepared LUV suspension by extruding such MLV suspension eight times through 0.1 μ m polycarbonate

membranes (GE Water & Process Technologies, Trevose, PA, U.S.A.) under 1.2 MPa nitrogen gas pressure. The mean diameter of the neutral LUVs was 145 nm and of the charged LUVs 130 nm, as determined by dynamic light scattering (ALV-NIBS/HPPS particle sizer, ALV-Laser Vertriebsgesellschaft mbH, Langen, Germany). The polydispersity index was in either case smaller than 0.1.

2.2.3 Potentiometric titration measurements

For sample preparation, we dissolved the drug in aqueous NaCl solution adjusted to pH \sim 3.5 with HCl (for bupivacaine and terbinafine) or to pH \sim 9.0 with NaOH (for diclofenac and ketoprofen). We then mixed the drug solution with the LUV suspension and thoroughly stirred the mixture for 15 minutes. Additional equilibration for up to 3 hours did not affect the results. For diclofenac and ketoprofen, we finally adjusted the mixture pH to \sim 3.5 with HCl. For each set of experiments, we used samples with at least four different lipid-water volumes ratios (between 0.006 and 0.11, corresponding to SPC concentrations between 7 and 126 mM) and maintained total drug concentration at 5 mM and ionic strength at either 150 mM or 600 mM.

For titrations, we used Mettler DL 67 and DL50 graphix automatic titrators (Mettler-Toledo, Switzerland), equipped with Lab X pro version 2.a instrument controlling software. We conducted all titrations alkalimetrically at 37 °C. We adjusted the titrant (0.1 M NaOH) with NaCl to maintain constant ionic strength during titrations. The titrant volume per addition was automatically adjusted within the range of 0.005-0.020 mL to limit the pH change to about 0.04 pH units. The sample was allowed to equilibrate under stirring for 1-10 minutes after each titration step.

We determined bupivacaine's and ketoprofen's aqueous pK_a by fitting the measured potentiometric titration curves, over the pH range in which the tested drug is soluble, with the conventional titration equations. For diclofenac and terbinafine we used the published aqueous pK_a values of 4.01 and 7.05, respectively^[83].

2.2.4 Potentiometric data analysis

We programmed a Mathcad calculation sheet (Mathcad version 11.0b, Mathsoft Engineering & Education, Inc., Cambridge, MA, USA) with the set of equations given in Results and Discussion section and in Appendix 2.A. This included expressions for the intrinsic (lipid-dependent) membrane surface charge density, σ_{mem} , the surface charge density due to membrane associated drug (drug-dependent), σ_{D} , and the resulting membrane

electrostatic potential, ψ . We used the program to extract the test drugs partition coefficients from the measured pH titration data with non-linear regression analysis using Mathcad's equations solving routine (Levenberg-Marquardt algorithm). We checked analytical sensitivity by determining the lower and upper limit values for each parameter that yielded residual sum of squares 10% higher than the optimum parameters values. We confirmed that starting parameters variation over a reasonable range had no effect on final analytical results. We used the same program to model the theoretical cases illustrated in some of the figures.

2.3 Theoretical considerations

We used the partition coefficient most conventional expression, as the ratio of the molar drug concentration in the membrane, $C_{\text{mem},V}$, and in the aqueous compartment, $C_{\text{aq},V}$:

$$P = \frac{C_{\text{mem},V}}{C_{\text{aq},V}} \quad (2.1)$$

The subscript V denotes concentrations based on the lipid, V_{mem} , and the aqueous, V_{aq} , compartments volumes. The often used alternative definition:

$$P = \frac{C_{\text{mem}}V_{\text{aq}}}{C_{\text{aq}}V_{\text{mem}}} = \frac{C_{\text{mem}}}{C_{\text{aq}}r} \quad (2.2)$$

relies on C_{mem} and C_{aq} , defined analogously but based on the total suspension volumes, with r is the lipid-aqueous compartment volumes ratio. Both definitions presume a large excess of lipid over the lipid-associated drug fraction (limiting case). It is noteworthy that numeric partition coefficient values depend on the concentration units used^[84].

Introduction of a second compartment (e.g. octanol) influences the dissociation behavior of the tested compound (Fig. 2.2) and shifts its dissociation constant from $\text{p}K_{\text{a}}$ to $\text{p}K_{\text{a}}^{\text{app}\#}$. The shift mainly reflects the different local dielectric constants around drug molecules in different compartments. The shift depends also on the organic-aqueous compartment volumes ratio, r . One can accordingly deduce the partition coefficient of the protonated drug form, P^{XH} , and of the deprotonated drug form, P^{X} , from^[69, 85, 86]:

$$\text{p}K_{\text{a}}^{\text{app}\#} = \text{p}K_{\text{a}} + \log(1 + P^{\text{XH}}r^{\#}) - \log(1 + P^{\text{X}}r^{\#}) \quad (2.3)$$

which can be rewritten simply as:

$$\Delta\text{p}K_{\text{a}}^{\#}(r^{\#}, P^{\text{X}}, P^{\text{XH}}) = \log(1 + P^{\text{XH}}r^{\#}) - \log(1 + P^{\text{X}}r^{\#}) \quad (2.4)$$

$\text{p}K_{\text{a}}$ represents the aqueous dissociation constant and $\text{p}K_{\text{a}}^{\text{app}\#}$ the apparent dissociation constant

determined in the two-compartment mixture with an organic-aqueous compartment volumes ratio $r^\#$. Eqs. 2.3–2.4 are commonly used for potentiometric determination of partition coefficients. At least two $\text{p}K_a^{\text{app}\#}$ - $r^\#$ data pairs are needed to deduce P^{XH} and P^{X} .

The problem with Eq. 2.4 lies on the fact that the dissociation constant shift, $\Delta\text{p}K_a$, of a drug molecule bound to a surface (e.g. a lipid membrane or a micelle) is affected by electrostatic and other non-hydrophobic interactions at the drug binding sites, as well (Fig. 2.2). Eq. 2.4 neglects such interactions and fails to capture the potentially influential Coulombic electrostatic effects. This raises at least two problems. First, protons attraction into vicinity of a negatively charged surface and repulsion from a positively charged surface shifts the interfacial pH down and up, respectively. The interfacial pH experienced by the bound drug molecules consequently differs from the experimentally measured bulk pH (“local pH shift”). Second, the surface electrostatic potential directly influences the ionized drugs distribution, analogous to its effect on the protons distribution.

The local pH shift can be accounted for simply by introducing an electrostatic correction term, based on the Gouy-Chapman approximation, $\Delta\text{p}K_a^{\text{el}} = \log [\exp(-\Phi)] = -\Phi \log e = -\Phi / 2.3$ into Eq. 2.4, to get:

$$\Delta\text{p}K_a^\#(r^\#, P^{\text{X}}, P^{\text{XH}}, \Phi) = \log(1 + P^{\text{XH}}r^\#) - \log(1 + P^{\text{X}}r^\#) - \frac{\Phi}{2.3} \quad (2.5)$$

Φ is the normalized dimensionless electrostatic potential (cf. Appendix 2.A).

The membrane electrostatic potential originates from two sources. The first is the charged lipid membrane components, creating an intrinsic (lipid-dependent) membrane surface charge density, σ_{mem} . One can easily calculate such contribution from the known membrane composition (cf. Appendix 2.A). The second source of the membrane electrostatic potential is the ionized drug molecules partitioned into the membrane, which yields the drug-dependent surface charge density, σ_{D} . This density is, in the first approximation, proportional to the number of membrane associated ionized drug molecules per unit area (cf. Appendix 2.A), as has been also demonstrated directly with zeta potential measurements^[87, 88].

Despite awareness of the drug-dependent electrostatic potential existence and recognition of its possible influence on titration curves^[65, 68, 89], most researchers in the field continue to work with uncorrected potentiometric data. In contrast, it is now customary to include corrections for the drug-dependent electrostatic effects in the analyses of drug-membrane association measurements conducted at a constant pH, where it is admittedly easier

to achieve the task. Table 2.1 provides a summary of some drug distribution studies [66, 82, 88, 90-93], in which analysts have applied these corrections. The drug-dependent electrostatic contribution results in distribution coefficient values that are sensitive to experimental conditions and can be up to more than 90% below the correct value (Table 2.1).

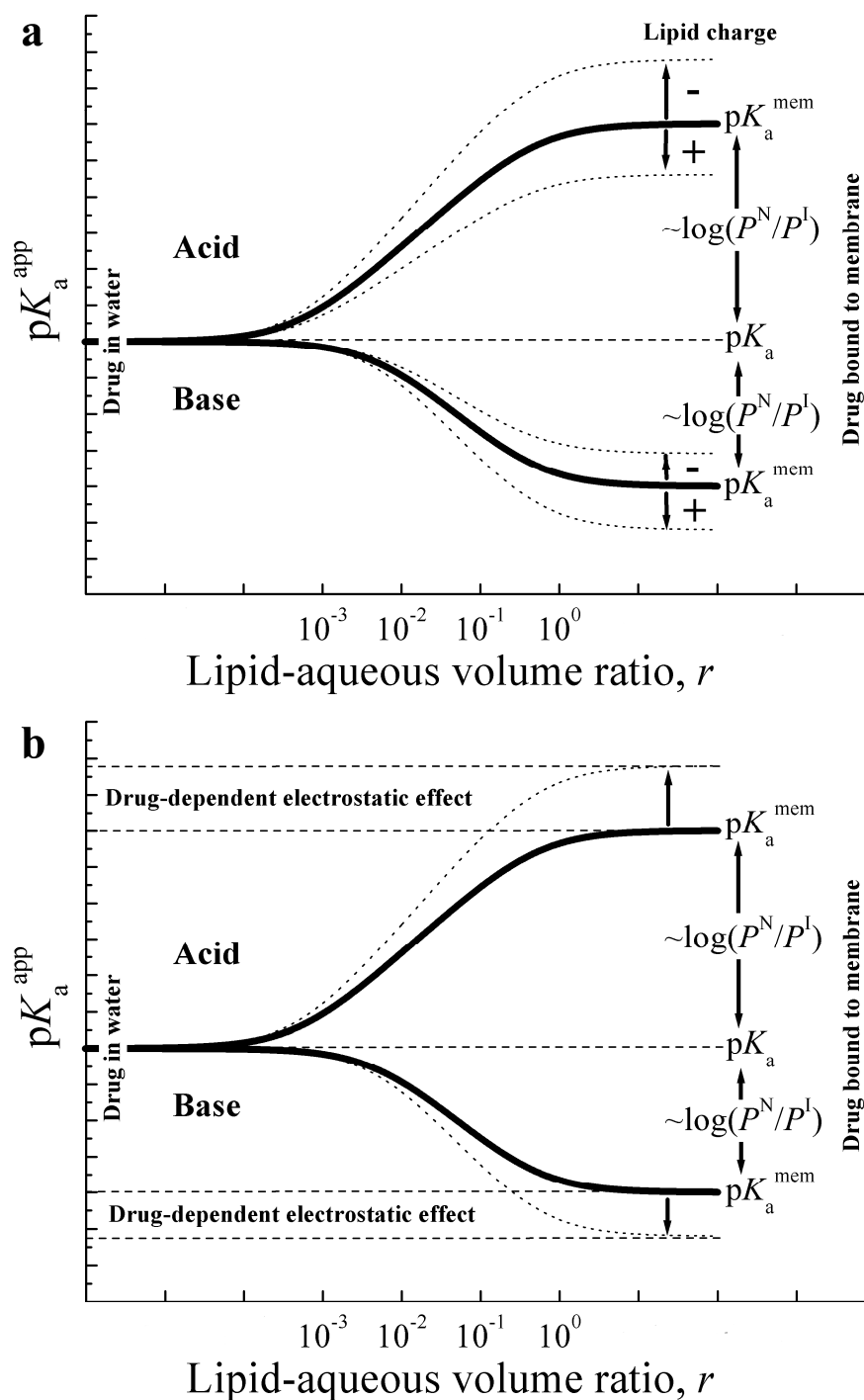


Figure 2.2 The apparent dissociation constant, pK_a^{app} , of acidic and basic drugs as a function of the lipid-aqueous compartment volumes ratio, r . The practically usable range is $10^{-3} < r < 10^{-1}$. a) Effect of intrinsic membrane charges. b) Effect of drug-dependent membrane charging.

Table 2.1 Effect of the drug-dependent electrostatic potential on measured apparent lipid membrane-water distribution coefficient, D .

Compound	Analytical technique	Distribution coefficient, D		D/D_0
		Neglecting electrostatics	Considering electrostatics	
Dibucaine ^[93]	Ultracentrifugation Using α -deuterated POPC vesicles: 0.1 M NaCl, 50 mM buffer, at pH = 5.5, 25 °C.	$52.6-259.5 \text{ M}^{-1}$ ^{a,b,f}	$660 \pm 80 \text{ M}^{-1}$ ^{a,f}	0.080–0.393
Etidocaine ^[93]	Ultracentrifugation Using α -deuterated POPC vesicles: 0.1 M NaCl, 50 mM buffer, at pH = 5.5, 25 °C.	$3.2-7.9 \text{ M}^{-1}$ ^{a,b,f}	$11 \pm 2 \text{ M}^{-1}$ ^{a,f}	0.290–0.716
Melittin ^[90]	Ultracentrifugation Using POPC vesicles: 40 mM buffer, at pH 6.8-6.9, 25 °C.	$(0.4-1.6) \times 10^3 \text{ M}^{-1}$ ^{b,f}	$(2.1 \pm 0.2) \times 10^3 \text{ M}^{-1}$ ^f	0.177–0.779
Flunarizine ^[88]	Ultracentrifugation Using POPC vesicles: 0.1 M NaCl, 30 mM buffer, at pH = 5.0, 20 °C.	$6885-19430 \text{ M}^{-1}$ ^{a,b,f}	$28700 \pm 3350 \text{ M}^{-1}$ ^{a,f}	0.240–0.677
Amlodipine ^[91]	Ultracentrifugation Using POPC vesicles: 0.1 M NaCl, 10 mM buffer, at pH = 7.25, 25 °C.	$3984-10476 \text{ M}^{-1}$ ^{a,b,f}	$15500 \pm 1000 \text{ M}^{-1}$ ^{a,f}	0.257–0.672
Proxycromil ^[66]	Ultrafiltration Using DOPC vesicles at pH = 7.4, 25 °C.	$1650-7172$ ^{a,c,e}	8154 ^{a,e}	0.202–0.880
Salmeterol ^[66]	Ultrafiltration Using DOPC vesicles at pH = 7.4, 25 °C.	$3640-11674$ ^{c,e}	9552 ^e	0.381–1.222
Sodium cholate ^[92]	Isothermal titration calorimetry Using DPPC vesicles: water at pH = 7.4, 60 °C	7750 ^{a,d,g}	6.4×10^6 ^{a,g}	0.001
Sodium cholate ^[92]	Isothermal titration calorimetry Using DPPC vesicles: 0.1 M NaCl at pH = 7.4, 60 °C	2.0×10^5 ^{a,d,g}	9.8×10^5 ^{a,g}	0.204

^a Experiments were carried out at pH values where the compounds are assumed by the authors to be more than 99% ionized (i.e. $D \approx P^I$).

^b Range of D values measured through different drug concentrations.

^c Range of D values measured through different ionic strengths and drug concentrations.

^d Average partition coefficient through the whole concentration range used.

^e D calculated using molar concentration units.

^f D calculated is lipid membrane related concentration units.

^g D calculated using mole fraction concentration units.

In the above-mentioned studies, the correction was done simply as an iterative, post hoc correction. More specifically, analysts first determined apparent drug distribution coefficients. They then calculated drug-dependent electrostatic potentials, based on bound drug concentration and used the results to correct originally measured apparent distribution coefficients. Point-by-point methods, where each experiment is carried out at a constant pH value and a constant lipid-drug ratio, allow such iterative post-correction. Potentiometric studies need complex correction procedure, however. The drug-dependent electrostatic potential changes during each single titration as a function of pH. Lipid-water volume ratio varies within each set of experiments, which affects the drug-dependent electrostatic potential as well. One must therefore apply electrostatic correction consistently to all data points.

To this end, we developed an analytical approach that explicitly considers Coulombic interactions and thus provides accurate intrinsic partition coefficient values for ionized as well as neutral drug forms independent of experimental conditions. The underlying principle is that binding of an ionized drug charges-up membranes and consequently affects the ionized drug apparent partition coefficient. The relationship between the observed apparent partition coefficient, P^I , and the real intrinsic partition coefficient, P_0^I , is given by the Boltzmann factor:

$$P^I = P_0^I \exp[-\Phi] \quad (2.6)$$

The membrane normalized dimensionless electrostatic potential, Φ , or the corresponding electrostatic potential at the drug binding site, $\psi = \Phi k_B T / z e_0$, is a function of the net surface charge density, σ , given by the sum of the lipid-dependent membrane surface charge density, σ_{mem} , and the drug-dependent surface charge density, σ_D . Eq. 2.4 therefore has to be replaced with Eq. 2.7 for acidic or Eq. 2.8 for basic drugs:

$$\Delta pK_a^\# = \log(1 + P_0^{\text{XH}} r^\#) - \log\left\{1 + P_0^{\text{X}} r^\# \exp[-\Phi(\sigma_{\text{mem}} + \sigma_D^\#)]\right\} \quad (2.7) \text{ For an acid}$$

$$\Delta pK_a^\# = \log\left\{1 + P_0^{\text{XH}} r^\# \exp[-\Phi(\sigma_{\text{mem}} + \sigma_D^\#)]\right\} - \log(1 + P_0^{\text{X}} r^\#) \quad (2.8) \text{ For a base}$$

These equations are self-consistent, i.e. contain interdependent parameters. The procedure for calculating Φ as a function of σ_{mem} and σ_D , and for solving such self-consistency problem, is described in appendix 2.A. The dissociation constant shift caused by Coulombic interactions, ΔpK_a^{el} , is positive or negative depending on the net membrane charge sign and the drug charge sign (cf. Fig. 2.2).

Table 2.2 The aqueous dissociation constants (pK_a) of tested drugs at 37 °C.

	Ionic strength [mM]	pK_a
Bupivacaine	150	8.02 ± 0.01
	600	8.10 ± 0.00
Ketoprofen	150	4.01 ± 0.02
	600	3.88 ± 0.03
Terbinafine ^[83]	150	7.05
Diclofenac ^[83]	150	4.01
Cholic acid	150	4.80 ± 0.00

2.4 Results and Discussion

The aqueous ionization/dissociation constants of bupivacaine and ketoprofen, measured at 37 °C, are given in Table 2.2. They agree with published data ^[94-96].

For the neutral membranes, simple use of the conventional model (Eq. 2.4), which neglects electrostatic interactions, leads to apparent partition coefficient values of the ionized drug forms that are typically lower than the correct intrinsic values (Eqs. 2.7-2.8). This is due to drug-dependent electrostatic potentials. We found the error to be around 12% (0.05 difference on the log scale) for bupivacaine and ketoprofen and around 17% (0.08 difference on the log scale) for cholate, under the experimental conditions used in this work (Table 2.3).

Partition coefficients of neutral drug forms should be unaffected by Coulombic interactions. For ketoprofen, with widely different P^N and P^I values, this is true. In contrast, the directly calculated P^N value of bupivacaine, with relatively close P^N and P^I values, is approximately 11% wrong (0.04 difference on the log scale), owing to the error-spillover from the uncorrected, and thus erroneous, P^I .

Ionic strength influences apparent P^I values; comparison of data measured for bupivacaine and ketoprofen in 150 mM and 600 mM electrolyte solutions shows that. We generally find that apparent P^I values are higher in more concentrated electrolyte solutions (Table 2.3), arguably due to decreasing surface electrostatic potentials with increasing ionic strength (electrostatic repulsion shielding caused by electrolyte counter-ions, see Appendix 2.A). Ionic strength thus relatively little affects potentiometrically derived partition coefficient values corrected for Coulombic interactions. It is noteworthy that simple adjustment of test medium ionic strength to biological salt concentrations does not ensure getting biologically relevant partition coefficients. One must in any case correct for drug-dependent membrane

Table 2.3 The lipid membrane-water partition coefficients of tested drugs at 37 °C.

Ionic strength [mM]	Lipid	Neglecting electrostatics		Considering electrostatics		
		$\log P^N$	$\log P^I$	$\log P_0^N$	$\log P_0^I$	
Bupivacaine	150	SPC	2.715 (2.693 – 2.738)	1.483 (1.443 – 1.522)	2.671 (2.657 – 2.684)	1.534 (1.505 – 1.562)
	600	SPC	2.846 (2.826 – 2.866)	1.688 (1.656 – 1.721)	2.787 (2.770 – 2.803)	1.680 (1.649 – 1.711)
	150	SPC / PG	2.715 ^a	1.710 (1.697 – 1.723)	2.671 ^a	1.534 ^b [1.377 (1.355 – 1.398)] ^d
Ketoprofen	150	SPC	3.284 (3.268 – 3.300)	0.940 (0.890 – 0.987)	3.280 (3.266 – 3.294)	0.997 (0.948 – 1.043)
	600	SPC	3.410 (3.390 – 3.431)	0.994 (0.932 – 1.052)	3.407 (3.388 – 3.427)	1.023 (0.963 – 1.081)
	150	SPC / PG	3.317 (3.304 – 3.330)	0.788 (0.737 – 0.836)	3.316 (3.304 – 3.328)	1.010 ^c [1.247 (1.196 – 1.295)] ^d
Terbinafine	150	SPC	---	---	5.194 (5.122 – 5.398)	3.775 (3.697 – 3.989)
	600	SPC	---	---	5.298 (4.996 – ∞)	3.917 (3.610 – ∞)
Diclofenac	150	SPC	---	---	3.924 (3.902 – 3.946)	2.356 (2.326 – 2.387)
Cholic acid	150	SPC	3.529 (3.494 – 3.567)	1.330 (1.253 – 1.405)	3.508 (3.481 – 3.534)	1.411 (1.342 – 1.476)

^a Fixed to the value observed for neutral membrane (SPC) at 150 mM ionic strength.^b Using interchange distance = 0.228 nm.^c Using interchange distance = 0.461 nm.^d Without allowing for separation between intrinsic membrane charges and drug-dependent charges.^e The conventional analytical approach, neglecting electrostatic interactions, fails to describe terbinafine and diclofenac titration (cf. Fig. 2.3) and delivers no sensible partition coefficient values.

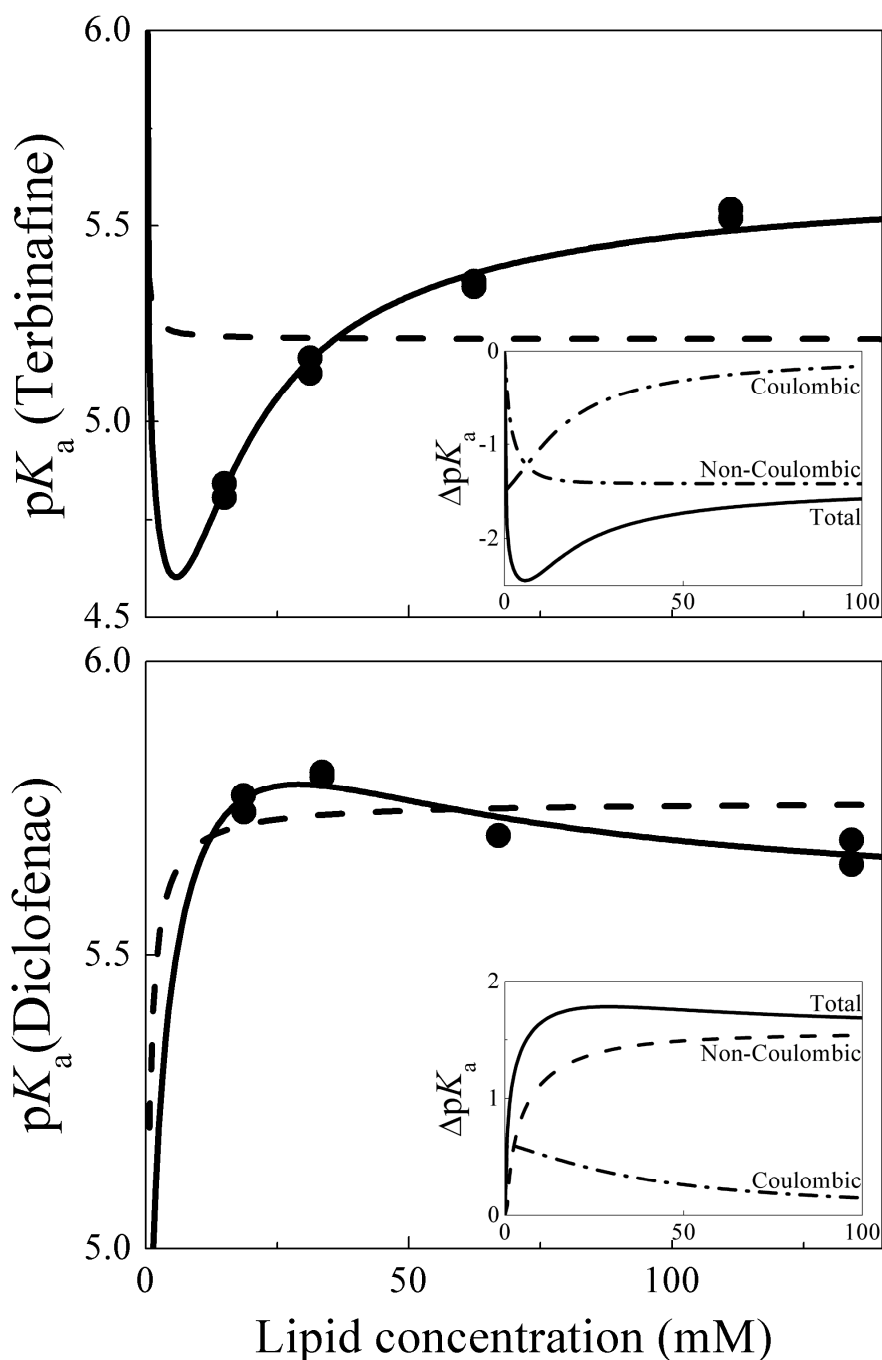


Figure 2.3. Terbinafine and diclofenac apparent dissociation constant, pK_a^{app} , as a function of the lipid-aqueous compartment volumes ratio, r , at 37 °C and 150 mM bulk ionic strength. The symbols show results of individual potentiometric titration experiments. The dashed curve describes the best fitting results using conventional data analysis that neglects electrostatic interactions (Eq. 2.4). The thick curve describes the best fitting results using the proposed analytical approach (Eqs. 2.7-2.8). Inset: The Coulombic and non-Coulombic contributions to the overall dissociation constant shift.

charging effects. The ionic strength effect, which is small in the current study for bupivacaine and ketoprofen, depends on drug P_0^I and lipid-drug molar ratio (up to 27 in the current work).

The effect is greater for drugs with higher P_0^I , for experiments conducted with lower lipid-drug molar ratios, or for experiments conducted with more dilute electrolyte solutions.

For terbinafine titrated in 600 mM electrolyte solution inclusion of the correction for Coulombic interactions was insufficient for a sensitive derivation of P_0^N and P_0^I values; we could only determine the lower parameters limit under such experimental conditions (Table 2.3). To get more meaningful data, experiments would have to be done with very low r values, i.e. in the steep part of the $pK_a^{\text{app}}-r$ curve (cf. Fig. 2.3), which is practically precluded by membrane saturation with the drug. The problem is less evident in 150 mM electrolyte, where stronger Coulombic effects shift the steep part of the $pK_a^{\text{app}}-r$ curve towards the higher, and thus experimentally accessible, r values (cf. Fig. 2.3).

To further explore the drug-dependent electrostatic effects, we calculated the error resulting from neglect of Coulombic interactions (Figs. 2.4-2.5). Avdeef et al. [67] suggested that drugs with high P^N require use of high lipid-drug molar ratios to ensure an excess of the available drug partitioning sites. They suggested the optimum lipid-drug molar ratios to be ≥ 5 , ≥ 2 , and ≥ 1 for drugs with $\log P^N > 5$, within 3-4, and < 3 , respectively [67]. Such recommendation considers the possible membrane saturation with the drug neutral form but neglects the equally possible “electrostatic saturation” due to the drug-dependent membrane charging. We addressed this latter problem by calculating the error (expressed as the ratio of the ionized drug form apparent and intrinsic partition coefficients, P^I/P_0^I), resulting from neglect of Coulombic interactions, as a function of the intrinsic ionized drug form partition coefficient and the selected lipid-drug molar ratio, at 150 mM ionic strength and 37 °C (Fig. 2.4). The difference between the correct intrinsic P_0^I and the apparent P^I can be quite large. Fig. 2.4 implies that the selected lipid-drug molar ratio should be > 31 for drugs with $\log P_0^I = 1$ and > 63 for drugs with $\log P_0^I = 2$ to keep the error in the derived P^I below 10 %. Using such a high lipid-drug molar ratio is impractical, however, as it precludes accurate potentiometric measurements. Moreover, even if a high lipid-drug molar ratio is used (by using a very large sample volume containing a considerable drug amount while maintaining a high lipid-drug molar ratio), the electrostatic correction is a prerequisite for analytical accuracy. Increasing the bulk ionic strength diminishes this need and reduces the error (cf. Fig. 2.5), but the error still exists even in a 1 M solution at lipid-drug molar ratio of 5. Electrostatic interactions must therefore be properly allowed for to ensure accurate potentiometric data analysis.

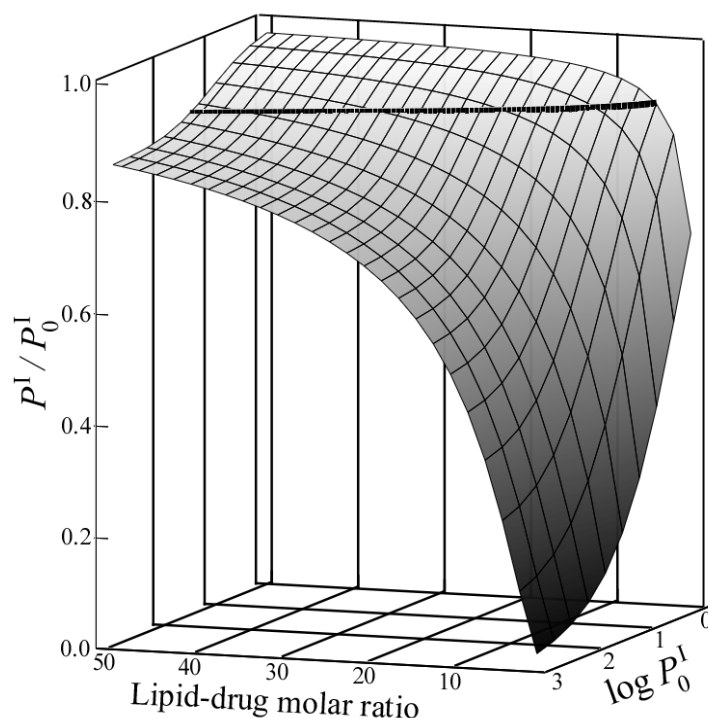


Figure 2.4 The effect of the drug-dependent Coulombic electrostatic interactions on the ionized drug form partitioning as a function of the drug-lipid molar ratio and the intrinsic partition coefficient of the ionized drug form, expressed as $\log P_0^I$. The curve gives the calculated error, expressed as the ratio of the ionized drug form apparent and intrinsic partition coefficients, P^I/P_0^I , at 150 mM bulk ionic strength and 37 °C. The thick curve shows the 0.9 limit, i.e. the 10% error boundary.

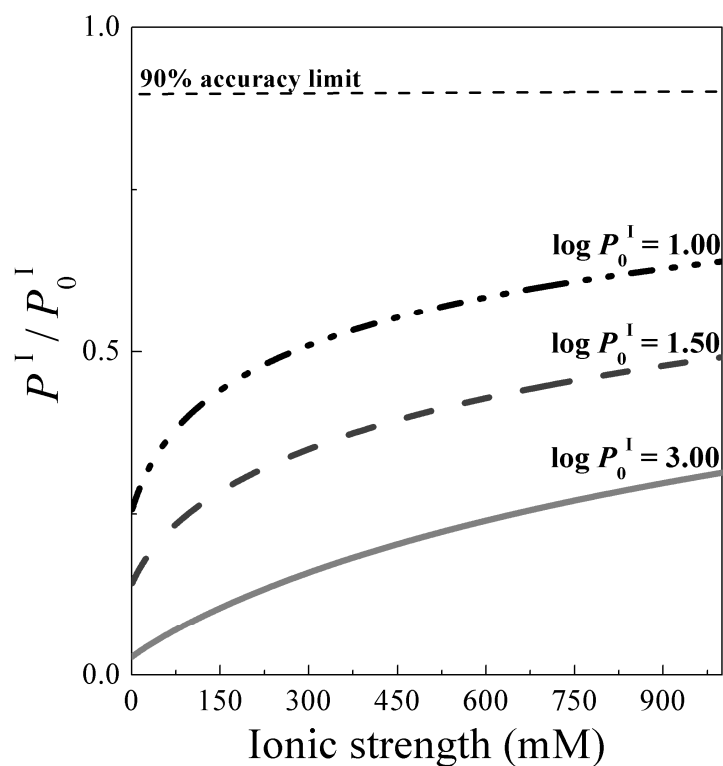


Figure 2.5 The effect of the bulk ionic strength on the ionized drug form apparent partition coefficient, P^I , modeled for a lipid-drug molar ratio of 5 at 37 °C.

We collected complementary evidence by studying test drugs partitioning into anionic liposomes prepared from a SPC/DMPG⁻ 93.36/6.74 mol/mol mixture. We expected more binding of the cationic bupivacaine and less binding of the anionic ketoprofen to such negatively charged membranes surfaces; the directly measured ΔpK_a^{app} values should be accordingly lower for bupivacaine and higher for ketoprofen relative to the neutral membranes (cf. Fig. 2.2). Fig. 2.6 shows that this was indeed the case. Similar results were reported for tetracaine, where increasing the percentage of anionic lipids in bilayer membranes from 0% to 30% lowered ΔpK_a^{app} from 0.43 to 0.24 pH units^[97]. This confirms the membrane electrostatics effect on drug partitioning.

Simple allowance for Coulombic interactions expressed through bilayer “surface potential” is reasonably accurate for the intrinsically neutral membranes, where $\Phi = \Phi(\sigma_D)$. The surface potential $\Phi = \Phi(\sigma_D + \sigma_{\text{mem}})$, calculated from the known negatively charged lipids concentration in the membrane, is often too high, however. It thus gives too low intrinsic P_0^I values for bupivacaine and too high such values for ketoprofen in the negatively charged membranes relative to the corresponding neutral membranes values (Table 2.3). Two most likely explanations are: i) the charged drug molecules bind at some distance from lipid charges, which lowers the effective electrostatic potential experienced by the former and diminishes discrepancy between P^I and P_0^I (cf. Eq. 2.19); ii) the assumed interfacial dielectric constant is too low. Assuming the highest possible interfacial dielectric constant ($\epsilon_r = 78$ for water) was not enough to correct the results, suggesting that the first explanation is more likely.

To test the hypothesis, we reanalyzed the data allowing for a finite distance between the charges on DMPG⁻ and on the bound drug molecules. We derived the effective electrostatic potential experienced by the drug molecules at their binding sites from the P_0^I values pertaining to the neutral membranes. This gave -16.6 mV for bupivacaine and -10.9 mV for ketoprofen. For comparison, the nominal surface potential calculated based on the known membrane composition is -25.8 mV. To experience such potential values, the distance between DMPG⁻ charges and bound drug charges should be 0.228 nm for bupivacaine and 0.461 nm for ketoprofen. Other factors, such as membrane hydration, could influence the calculated distance, but would change not the fundamental conclusion that intrinsic membrane and drug charges are dislocated. The calculated distances thus give an estimate of the relative drug positions in the membrane.

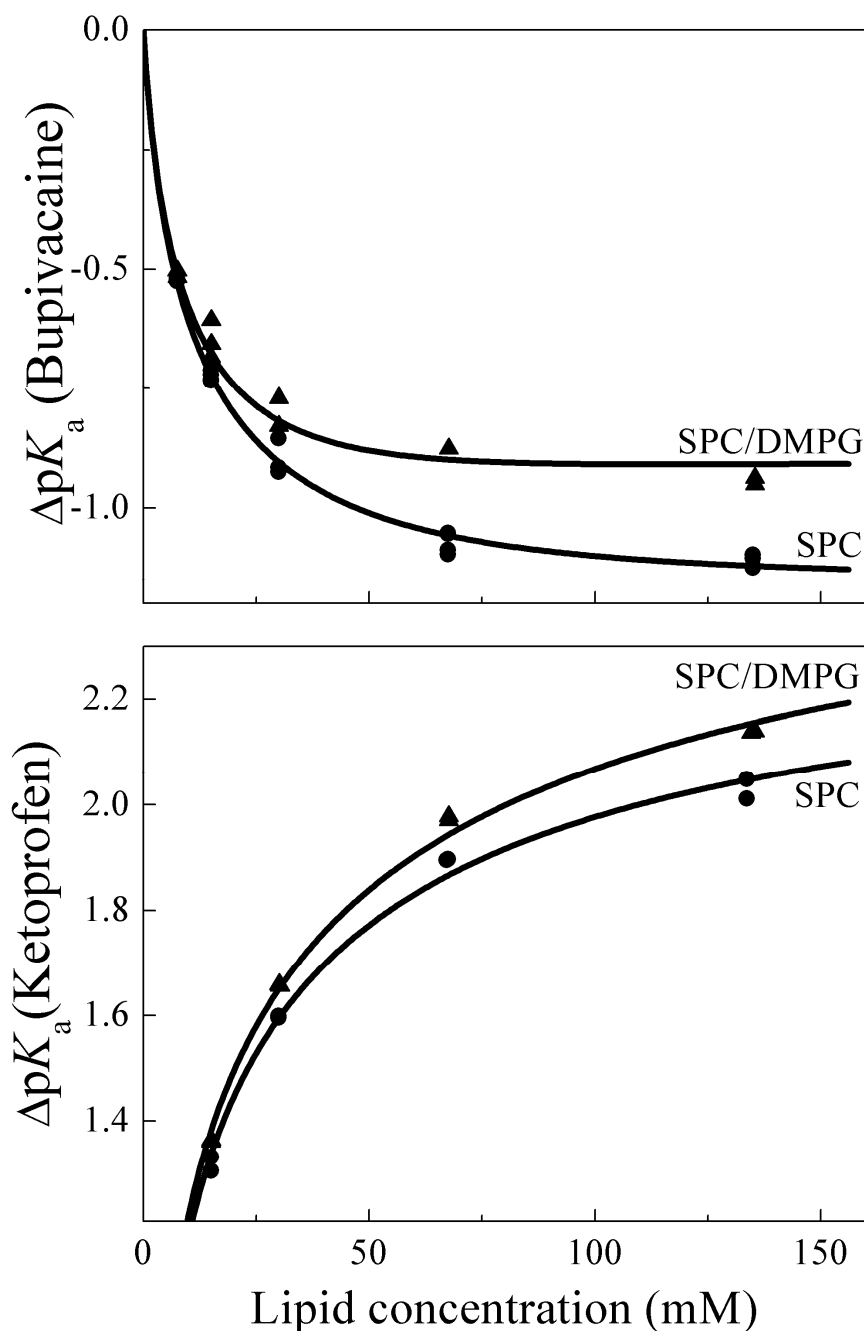


Figure 2.6 The effect of membrane charges on the apparent dissociation constant, pK_a^{app} , of bupivacaine and ketoprofen at 37 °C. The symbols show results of individual potentiometric titration experiments and the curve describe the best fitting results (Eq. 2.7-2.8).

Biological membranes bear a net negative surface charge [65, 98] that affects drug partitioning [99, 100]. For example, the negative surface charges on intestinal brush border membranes [98, 100] reportedly affect partitioning of different anionic and cationic drugs [100]. To deduce biologically relevant P^I values, one can take various approaches. The first is to use artificial membranes with a surface charge density similar to the biological membranes of interest. One can then use the analytical approach proposed in this publication to correct only

for the drug-dependent electrostatic effects. The second possible approach is to use neutral membranes and then employ the analytical approach proposed in this article to correct for drug-dependent electrostatic effects. As a side benefit one then gets the correct intrinsic P_0^I value, from which one can finally calculate the apparent partition coefficient in the biological membrane of interest (cf. Eq. 2.6).

2.5 Experimental recommendations

An earlier suggestion ^[69] is to cover experimentally a range of lipid-water compartment volumes ratios starting between the inverse partition coefficients values, i.e. $1/P^N < r < 1/P^I$, and ending at ratios $> 1/P^I$, for optimum data fitting and partition coefficients values resolution; this covers the steep part of the $pK_a^{\text{app}}-r$ curve shown in Fig. 2.2. We advocate testing the range of $1/P^N < r < \text{approx. } 1.5/P^I$, and to preselect the most useful specific r -values, such that ultimately should deliver quasi-equidistant pK_a^{app} values; the proposed analytical model, used in predictive fashion, is helpful to select such r -values. We furthermore recommend carrying out experiments with at least four different lipid-water compartment volumes ratios, and suggest repeating each measurement independently at least twice. For drugs with a relatively small $\log P^N - \log P^I$ difference, more r -values may be needed to resolve P_0^N and P_0^I values.

We counsel against using the method for drugs with too similar partition coefficients of the charged and uncharged drug forms (when $\log P^N - \log P^I < 0.5$). We also remind that experimental range at and nearly above $r = 1/P^N$ is practically inaccessible for the lipophilic drugs. Especially the drugs with a high P^N as well as P^I value have often the optimum $1/P^I$ and $1/P^N$ values below the lowest practically achievable r unburdened with membrane saturation. The Coulombic repulsion may help testing such drugs, as it reduces the apparent P^I value and thus widens the $1/P^I - 1/P^N$ range. To enhance the effect, one could try to increase the drug concentration, but this can provoke membrane saturation with the tested substance and ultimately fails (increasing the drug concentration raises the lowest practically achievable r unburdened with membrane saturation). A better option is to decrease ionic strength of the suspending electrolyte, which is normally feasible. In the current study we were, indeed, able to sensitively determine lipid membrane-water partition coefficients of the highly lipophilic terbinafine from experimental data with 150 mM but not with 600 mM electrolyte (Table 2.3).

The ‘electrostatically enhanced’ potentiometric method, which we are describing, is really useful – even at intermediate ionic strengths (~ 0.1 M) – just for the drugs with $\log P_0^I <$

4 and not higher; for the drugs with $\log P_0^I > 4$ the method can only afford the lower limit for each partition coefficient. We recommend using the bulk ionic strength of 150 mM, which is quasi-physiological and resolution enhancing, for the typical potentiometric partition coefficient measurements.

In general, the tested drug concentration should be high enough to ensure accurate potentiometric results. One should in any case keep temperature constant and adjust ionic strength of the titrant solution to that of the sample to avoid ionic strength changes during the titration experiment. The same ionic strength and temperature should be used with simple aqueous (for aqueous pK_a determination) and bi-compartment aqueous/lipid mixed systems.

We accept aqueous pK_a literature values only if they were published with sufficient experimental detail and reliable information on the used ionic strength and temperature. We prefer doing alkalimetric titrations, which are relatively more reliable, as they minimize the problem of CO_2 absorption (when starting an experiment at high pH); working under an inert gas atmosphere further reduces the problem.

2.6 Conclusions

We proposed and explained a new analytical approach suitable for analyzing results of potentiometric measurements. The model delivers accurate and reliable lipid membrane-water partition coefficients for the ionized and the neutral drug forms. In contrast to the conventional analytical approach, the new approach is essentially insensitive to experimental conditions, as it properly considers the Coulombic electrostatic interactions, which is responsible for ionic strength and surface charge density effects.

If one corrects experimental results for the drug-dependent electrostatic contributions, one can deal successfully with both neutral and charged lipid membranes, to which the tested drugs are binding. The improved analytical procedure thus lends itself to applications beyond the potentiometric determination of partition coefficients, especially in bio-analytics, and in studies with bio-mimetic systems, having a composition similar to biologically interesting membranes.

Appendix 2.A

The intrinsic (lipid-dependent) membrane surface charge density, σ_{mem} , is calculated based on the membrane composition:

$$\sigma_{\text{mem}} = z_L e_0 \cdot \frac{x_C}{(1-x_C) \cdot A_N + x_C \cdot A_C} \approx \frac{z_L e_0 x_C}{A_L}, \quad (2.9)$$

where z_L is the charged lipid valence, e_0 the elementary electric charge, x_C the molar fraction of the charged lipids with molecular area A_C , and A_N the average surface area of the neutral lipid molecules. In the current study, we used $A_N \approx A_C \approx 0.65 \text{ nm}^2$, which is a good approximation for typical fluid-phase phospholipids. During potentiometric titration, the relative proportion of the charged lipids may vary, if the employed pH range overlaps with the lipid titration range. If so, the resulting surface charge density variation must be considered.

The average drug-dependent membrane surface charge density, σ_D , is calculated analogously:

$$\sigma_D = z_D e_0 \frac{C_{\text{mem}}^I}{C_L A_L + (C_{\text{mem}}^I + C_{\text{mem}}^N) A_D} \approx z_D e_0 \frac{C_{\text{mem}}^I}{C_L A_L}. \quad (2.10)$$

z_D is the bound drug valence, C_L the membrane-forming lipid concentration, C_{mem}^I and C_{mem}^N the concentrations of the membrane associated ionized and neutral drug forms, respectively. The contribution of the membrane associated drug molecules to the lipid bilayer surface area, A_D , is normally relatively small. It can thus be neglected. We can now calculate σ_D once C_{mem}^I is known.

To calculate C_{mem}^I , we will start with the total drug concentration $C_{\text{tot}} = C_{\text{mem}} + C_{\text{aq}}$. Substitution of C_{aq} from Eq. 2.2 and rearrangement allow calculation of the total membrane bound drug concentration:

$$C_{\text{mem}} = C_{\text{tot}} \frac{P r}{1 + P r}. \quad (2.11)$$

The ionized drug fraction, α , is:

$$\alpha = \begin{cases} \frac{10^{\text{pH} - \text{p}K_a^{\text{app}}}}{10^{\text{pH} - \text{p}K_a^{\text{app}}} + 1} & \text{for an acid} \\ \frac{10^{\text{p}K_a^{\text{app}} - \text{pH}}}{10^{\text{p}K_a^{\text{app}} - \text{pH}} + 1} & \text{for a base} \end{cases}. \quad (2.12)$$

Combining Eqs. 2.6, 2.11, and 2.12 yields:

$$C_{\text{mem}}^{\text{N}} = C_{\text{tot}} \cdot (1 - \alpha) \cdot \frac{P_0^{\text{N}} r}{1 + P_0^{\text{N}} r} \quad (2.13)$$

$$C_{\text{mem}}^{\text{I}} = C_{\text{tot}} \alpha \frac{P_0^{\text{I}} r \exp[-\Phi(\sigma_{\text{mem}} + \sigma_{\text{D}}^{\#})]}{1 + P_0^{\text{I}} r \exp[-\Phi(\sigma_{\text{mem}} + \sigma_{\text{D}}^{\#})]}, \quad (2.14)$$

which takes into account the Coulombic electrostatic contributions from both σ_{D} and σ_{mem} . The superscript I denotes the deprotonated form, X, for an acidic drug and the protonated form, XH, for a basic drug (cf. Eq. 2.7-2.8). All concentrations are defined relative to the total suspension volume. Combining Eqs. 2.10 and 2.14 finally yields the drug-dependent surface charge density:

$$\sigma_{\text{D}} \approx \frac{z_{\text{D}} e_0 C_{\text{tot}} \alpha}{C_{\text{L}} A_{\text{L}}} \cdot \frac{P_0^{\text{I}} r \exp[-\Phi(\sigma_{\text{mem}} + \sigma_{\text{D}}^{\#})]}{1 + P_0^{\text{I}} r \exp[-\Phi(\sigma_{\text{mem}} + \sigma_{\text{D}}^{\#})]} \quad (2.15)$$

The procedure is applicable at any pH value and ideally should involve the entire titration curve. σ_{D} is a function of Φ (or ψ) and vice versa, i.e. they are interdependent. The equation must thus be solved in a self-consistent fashion, and typically numerically (we used Mathcad, which employs Secant and Mueller method for numerical solving).

The Debye ion screening length, λ_{D} , is a property of the electrolyte solution and is given for 1:1 electrolytes by:

$$\lambda_{\text{D}} = \sqrt{\frac{\varepsilon_0 \varepsilon_{\text{r}} k_{\text{B}} T}{2000 e_0^2 N_{\text{A}} C_{\text{el}}}} \quad (2.16)$$

ε_0 is the permittivity of free space (8.8542 10⁻¹² As/Vm), ε_{r} the dielectric constant at the drug binding site (an average value of 40 for the lipid head group was used), k_{B} the Boltzmann constant (1.38 10⁻²³ JK⁻¹), T the absolute temperature, e_0 the elementary electric charge (1.602 10⁻¹⁹ C), N_{A} Avogadro's number (6.02205×10²³ mol⁻¹), C_{el} the bulk molar electrolyte concentration.

The electrostatic potential, ψ , of a uniformly charged surface in contact with a 1:1 electrolyte is given within the framework of Gouy-Chapman approximation^[101], as a function of the total surface charge density, $\sigma = \sigma_{\text{D}} + \sigma_{\text{mem}}$, by:

$$\psi(\sigma) = \frac{2k_{\text{B}}T}{e_0} \operatorname{asinh}\left(\frac{\lambda_{\text{D}} e_0 \sigma}{2\varepsilon_0 \varepsilon_{\text{r}} k_{\text{B}} T}\right) \quad (2.17)$$

σ is the surface charge density in Cm^{-2} and asinh the inverse hyperbolic sine (*areasinushyperbolicus*). The normalized dimensionless electrostatic potential, Φ , is defined as the ratio of electrostatic potential energy, $ze_0\psi$, and thermal energy, $k_B T$:

$$\Phi(\sigma) = \frac{ze_0 \psi(\sigma)}{k_B T} \quad (2.18)$$

According to the Gouy-Chapman model, the relationship between the electrostatic potential $\psi(x)$ at distance x from a uniformly charged surface and the electrostatic surface potential $\psi(x=0)$, is:

$$x = \ln \left\{ \frac{\tanh [e_0 \psi(x=0, \sigma) / 4k_B T]}{\tanh [e_0 \psi(x, \sigma) / 4k_B T]} \right\} \cdot \lambda_D \quad (2.19)$$

This provides means for estimating the effective distance between the lipid and the drug charges in a membrane.

The electrostatic correction described in this article allows only for the Coulombic, i.e. charge-charge interactions. Other contributions, such as hydration (polarity) effects, can be influential as well. If they are not small, such interactions should be considered, following the basic, self-consistent approach described in this work.

3 The vesicle-to-micelle transformation of phospholipid-cholate mixed aggregates: A state of the art analysis including membrane curvature effects*

Contents

3.1	Introduction	35
3.2	Materials and Methods	36
3.2.1	Materials	36
3.2.2	Preparation of lipid vesicles	37
3.2.3	Preparation of samples	37
3.2.4	The static light scattering (turbidimetry)	38
3.2.5	The dynamic light scattering (photon correlation spectroscopy)	38
3.2.6	Data analysis	39
3.3	Results	39
3.3.1	The quasi-steady state light scattering	39
3.3.2	The time-resolved light scattering	44
3.3.3	Quantitative analysis of the cholate-facilitated bilayer fluctuations	45
3.4	Discussion	47
3.4.1	Experimental considerations	47
3.4.2	Supramolecular view of the vesicle-to-micelle transformation	49
3.5	Conclusions	57
	Appendix 3.A	59
	Appendix 3.B	62
	Appendix 3.C	64

* This chapter was published as: M.M.A. Elsayed, G. Cevc. The vesicle-to-micelle transformation of phospholipid–cholate mixed aggregates: A state of the art analysis including membrane curvature effects. *Biochim. Biophys. Acta.* 1808 (2011) 140-153.

3.1 Introduction

Bile salts are a special group of physiological detergents, or bio-surfactants, with a major role in lipid absorption in the intestine. The chemical structure of bile salts differs from that of the typical head-tail surfactants (e.g. alkyl glucosides, alkyl sulphates, fatty acid polysorbates), which consist of a polar “head” with one or several hydrophilic groups attached to a separate hydrophobic chain/s, or a “tail”. In contrast, each bile salt molecule has a rigid steroid core with one lipophilic, convex surface and one hydrophilic, polyhydroxylated, concave surface^[102] (Fig. 3.1). The ring system is central in bile salt interactions with other molecules. The self- and hetero (with various lipids)-aggregation of bile salts and head-tail surfactants therefore differ in detail.

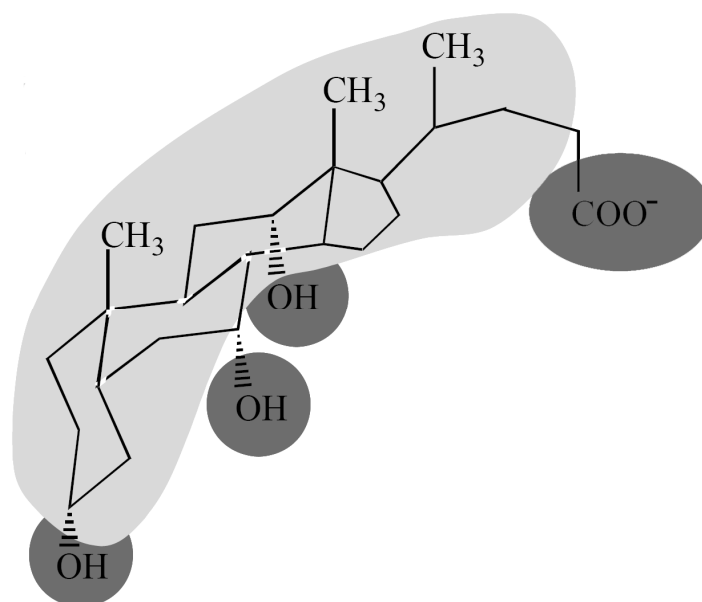


Figure 3.1 The structural and chemical formula of a cholate molecule, showing the hydrophobic surface (light grey) and the hydrophilic groups (dark grey) on the other molecular side (modified from^[102]).

Bile salt-lipid interactions are of physiological and fundamental interest. They are a key to understanding intestinal fat digestion and absorption^[103] and the basis for various applications. In biochemistry, for example, bile salts are used to isolate membrane proteins and to reconstitute such proteins into lipid bilayers^[59-62]. In pharmaceuticals, bile salts are included into some drug delivery systems, such as mixed micelles^[104] (e.g. Konakion® MM, Valium® MM) or ultradeformable mixed lipid vesicles^[105-113]. The self-assembly, i.e. the homo-aggregation, of bile salts into micelles and their hetero-aggregation with other lipids that tend to form bilayers, such as the ubiquitous phosphatidylcholines, are of physicochemical significance as well.

Phospholipid-bile salt mixtures were extensively investigated for decades, with focus on lipid/cholesterol solubilisation and vesicle-to-micelle transformation [59, 61, 92, 102, 103, 114-127]. A large body of experimental data was collected over the years, but some important questions remain open. To our knowledge, the mixed aggregates detailed morphology, molecular composition, and their interrelationship in the transition region, are not yet fully elucidated. We herein pay full attention to the previously neglected curvature effects on bilayer solubilisation and on the comparability of vesicle-to-micelle with micelle-to-vesicle transformation. Unlike previous researchers in the field we also ensure complete cholate ionisation during the process, as cholate like other ionic surfactants is (maximally) active in its ionised form.

In this report we address the complete sequence of structural and morphological changes occurring during the vesicle-to-micelle transformation in phosphatidylcholine-sodium cholate mixtures under consideration of (local) bilayer curvature effects. For this purpose, we studied the initial vesicle size effects on natural phosphatidylcholine vesicle transformation into cholate dominated mixed micelles, relying on static and dynamic light scattering. We analyzed the results with several theoretical models to explain the experimental observations quantitatively. The emerging picture of vesicle-to-micelle transformation is richer but also more complex than previously known, raising some experimental caveats. To list but the most important ones: the very popular optically measured “bilayer-saturating concentration” is an ill-defined “descriptor” with an assay-, preparation history-, and size-dependent value; the “three-step solubilisation” model is pedagogically useful but never strictly applicable to reality, where continuous solubilisation prevails; the bilayer solubilising concentration is the only robust descriptor of lipid solubilisation in the tested mixtures, but it also depends on the starting aggregate size and is potentially burdened with the slow transition kinetics; the results measured with only partially ionized surfactant molecules are questionable due to interfacial effects on molecular charge, and vice versa.

3.2 Materials and Methods

3.2.1 Materials

We obtained soybean phosphatidylcholine (SPC, Lipoid S 100, purity = 97.8%, the assumed average molecular weight \sim 800 g/mol) from Lipoid GmbH (Ludwigshafen, Germany). Sodium cholate hydrate (purity \geq 97 %) was from Sigma-Aldrich (Steinheim, Germany). All the other chemicals and reagents were of analytical grade. Polycarbonate

membranes were from GE Water & Process Technologies (Trevose, PA, U.S.A.).

3.2.2 Preparation of lipid vesicles

In brief, we dissolved the necessary amount of phosphatidylcholine in a sufficient amount of chloroform in a 500 mL round-bottom flask. We evaporated the solvent under vacuum at 50 °C in a rotary evaporator. This yielded a thin lipid film, which we hydrated at the same temperature with bidistilled water. The ensuing suspension of multilamellar vesicles (MLV) had a total phospholipid concentration of 120 mg g⁻¹ (~ 150 mmol kg⁻¹). We then produced large unilamellar vesicles (LUV) from such MLV by extruding the original “crude” suspension 10 times through a set of polycarbonate membranes with 80 nm pores under 1.75 MPa (254 psi) nitrogen gas pressure. To gain intermediate-size unilamellar vesicles (IUV), we further extruded the LUV suspension eight times through a set of polycarbonate membranes with 30 nm pores under nitrogen gas pressure of 2.50 MPa (363 psi). To obtain the smallest achievable unilamellar vesicles (SUV), we sonicated the IUV suspension on ice with a Sonopuls HD 3100 ultrasonic probe homogenizer (Bandelin electronic, Berlin, Germany) until the suspension became opalescent (using an MS 73 tip and a sonication power of 20 W, this took approximately 150 min for a 25 g sample). Finally, we filtered the sonicated SUV suspensions through a polycarbonate membrane with 80 nm pores under 1.75 MPa nitrogen gas pressure to remove the titanium particles originating from the ultrasound transducing tip. We measured the final phospholipid concentration with HPLC to confirm that no lipid material was lost during preparation. For this purpose, we used an in-house modification of the method described by Nasner and Kraus^[128], with refractive index detection^[129].

3.2.3 Preparation of samples

We prepared vesicle suspensions with different lipid concentrations in an aqueous carbonate buffer (50 mM, pH = 10.25) adjusted with NaCl to a final ionic strength of 150 mM. For this purpose, we diluted the original LUV, IUV, or SUV suspensions, prepared in distilled water, with appropriate volumes of the buffer. We always prepared fresh samples immediately before starting an experiment to minimize lipid degradation/hydrolysis at the high chosen pH. We also prepared a series of sodium cholate solutions/suspensions with different concentrations in a similar buffer and adjusted each preparation to 150 mM ionic strength with NaCl. We then mixed an aliquot of the tested vesicles suspension with an equal volume of the appropriate sodium cholate solution/suspension by stirring the blend thoroughly. For the steady state experiments, we left the mixtures to equilibrate at room

temperature (~ 25 °C), until its optical density became constant. We then recorded the static and the dynamic light scattering data of each separately prepared mixture. To conduct the time-resolved measurements, we mixed the individual components in a jacketed (25 °C) glass reservoir connected to a flow-through quartz cuvette with peristaltic pump tubing. An eight-channel Gilson (Villiers le Bel, France) Minipuls-3 peristaltic pump maintained a steady suspension flow through the cuvette, in which we recorded the optical density continuously until reaching a constant value. To assess phosphatidylcholine hydrolysis during experiments, we checked phosphatidylcholine and lysophosphatidylcholine concentrations in representative samples with the described HPLC method.

3.2.4 The static light scattering (turbidimetry)

We measured the static light scattering (optical density) with a Shimadzu UV-1601 double-beam UV-VIS spectrophotometer equipped with a 6 position, automated sample changer and the Shimadzu UVProbe version 2.0 software (Shimadzu Corporation, Kyoto, Japan). We first confirmed that the light absorbed by SPC in the employed concentration range is negligible between 400 nm and 500 nm. We then read the optical density of the tested LUV and IUV mixtures at 500 nm. For the SUV mixtures we recorded the optical density at 400 nm to increase sensitivity and allowed for the difference in the final data analysis.

3.2.5 The dynamic light scattering (photon correlation spectroscopy)

We used an ALV-NIBS/HPSS particle sizer (ALV-Laser *Vertriebsgesellschaft mbH*, Langen, Germany) for the dynamic light scattering measurements. We characterised each sample at 25 °C in three individual measurements and then analyzed the results with the ALV-5000/E/EPP software (version 3.0, regularized fit routine) based on the CONTIN 2DP method^[130, 131]. In so doing, we also accounted for temperature, salt, and cholate effects on the dispersion medium viscosity. In brief, we started with the dynamic viscosity of water at 25 °C, being 0.89038 cP^[132]. We then calculated the dynamic viscosity of the employed aqueous carbonate buffer following Pereira et al.^[132], to be 0.91711 cP. We allowed for sodium cholate effects on the dispersion medium viscosity, relying on the data of Wang, et al.^[133]. Lacking any reliable information on cholate binding under our experimental conditions, we assumed for the purpose that all cholate molecules are dissolved in the aqueous medium; this may have overestimated the surfactant effects. This revealed that sodium cholate in the studied concentration range affects the dispersion medium viscosity, and thus our analytical results, only little (< 3%). For better accuracy we included the correction in our analyses.

Allowance for cholate binding effect would introduce a practically negligible correction.

3.2.6 Data analysis

We analyzed all experimental data either with Microcal Origin (version 6.0, Microcal Software, Inc., Northampton, MA, USA) or with a suitable Mathcad (version 11.0b, Mathsoft Engineering & Education, Inc., Cambridge, MA, USA) programme.

3.3 Results

To explore bilayer curvature effects on phospholipid–cholate interactions and bilayer solubilisation we first prepared essentially unilamellar soybean phosphatidylcholine bilayer vesicles with the different sizes summarized in Table 3.1.

3.3.1 The quasi-steady state light scattering

Large unilamellar vesicles (LUV) change their optical density promptly after addition of sodium cholate, but ultimately attain a constant optical density. The upper panel in Fig. 3.2 shows such final constant molar optical density value as a function of total phospholipid and total cholate concentrations. The lower panel gives the corresponding mean diameter of the mixed aggregates as determined with the dynamic light scattering. The figure also contains information on the intensity-normalized fraction of the peak pertaining to the mixed lipid vesicles and/or to other large mixed aggregates in each preparation.

As is evident from Fig. 3.2, increasing total cholate concentration alters optical density of the studied suspensions non-monotonously. The initial optical density change is negative and relatively sharp ($\sim -30\%$ per mmol total cholate kg^{-1}). The change then turns positive, with a flatter slope, and finally becomes negative again. The final slope is steep in the first part and flatter towards the end of each solubilisation curve. Lipid concentration can enhance or suppress this sequence of changes and slopes.

Table 3.1 The average diameter of the studied SPC vesicles ^a, as determined with the dynamic light scattering.

	Mean diameter (nm)	Polydispersity index
LUV	121.8	≤ 0.13
IUV	82.8	≤ 0.16
SUV	44.1	≤ 0.24

^a Concluding from the published information pertaining to the used preparation method ^[56, 134], less than 10% of the vesicles were oligolamellar.

The dynamic light scattering yields qualitatively similar but quantitatively different results compared with the static light scattering (see Fig. 3.2). The dynamic light scattering curve pertaining to the LUV is generally shifted towards higher cholate concentrations relative to the static light scattering curve (cf. Fig. 3.2 lower vs. upper panel).

The dynamic light scattering uncovers coexistence of relatively small mixed micelles and much larger aggregates over a broad range of total cholate concentrations (Fig. 3.2, lower panel). The position of the peak pertaining to the large scatterers (including mixed amphipat vesicles, thread-like mixed aggregates, etc.) varies among the replicates of the same sample at high cholate concentration, as is reflected in the relatively large standard deviations illustrated in Fig. 3.2 (lower panel). We moreover detected an additional size-peak between 400 nm and 900 nm with dynamic light scattering in an appreciable number of samples (data not included into Fig. 3.2 for better clarity). Taken together, this implies that large aggregate with different sizes and/or various shapes coexist during lipid (partial) solubilisation. They are not resolvable with dynamic light scattering. The available mathematical models for analysing dynamic light scattering data presume similar geometry for all scatterers. We calculated various size values assuming spherical, rather than discoidal or thread-like, micellar shapes. The average mixed micelle size generally decreases from ~ 14 nm to ~ 5 nm with raising total cholate concentration in the vesicle-micelle coexistence range.

Small unilamellar vesicles (SUV) become slightly more optically dense after addition of small cholate amounts (optical density increases approx. 4–10 % per 1 mmol total cholate kg^{-1} , see Fig. 3.3), in contrast to the situation found with the LUV. Further raising cholate concentration steeply increases the suspension optical density; the maximum value corresponds to nearly three times higher optical density for the cholate-containing *vs.* the original cholate-free preparation (Fig. 3.3). Increasing cholate concentration beyond such optical density maximum decreases the suspension optical density sharply to a quasi “plateau”. This indicates essentially complete bilayer vesicle solubilisation into small mixed amphipat micelles. The solubilisation curve measured with the SUV shows no tailing in contrast to the LUV or the IUV curves (Figs. 3.2–3.4).

The average hydrodynamic diameter of the studied aggregates and the suspension optical density depend qualitatively similarly on total cholate concentration. Exceptional are only low cholate concentrations: addition of a small cholate amount changes little the hydrodynamic diameter of the mixed amphipat vesicles derived from the SUV ($- 2.0$ nm); the

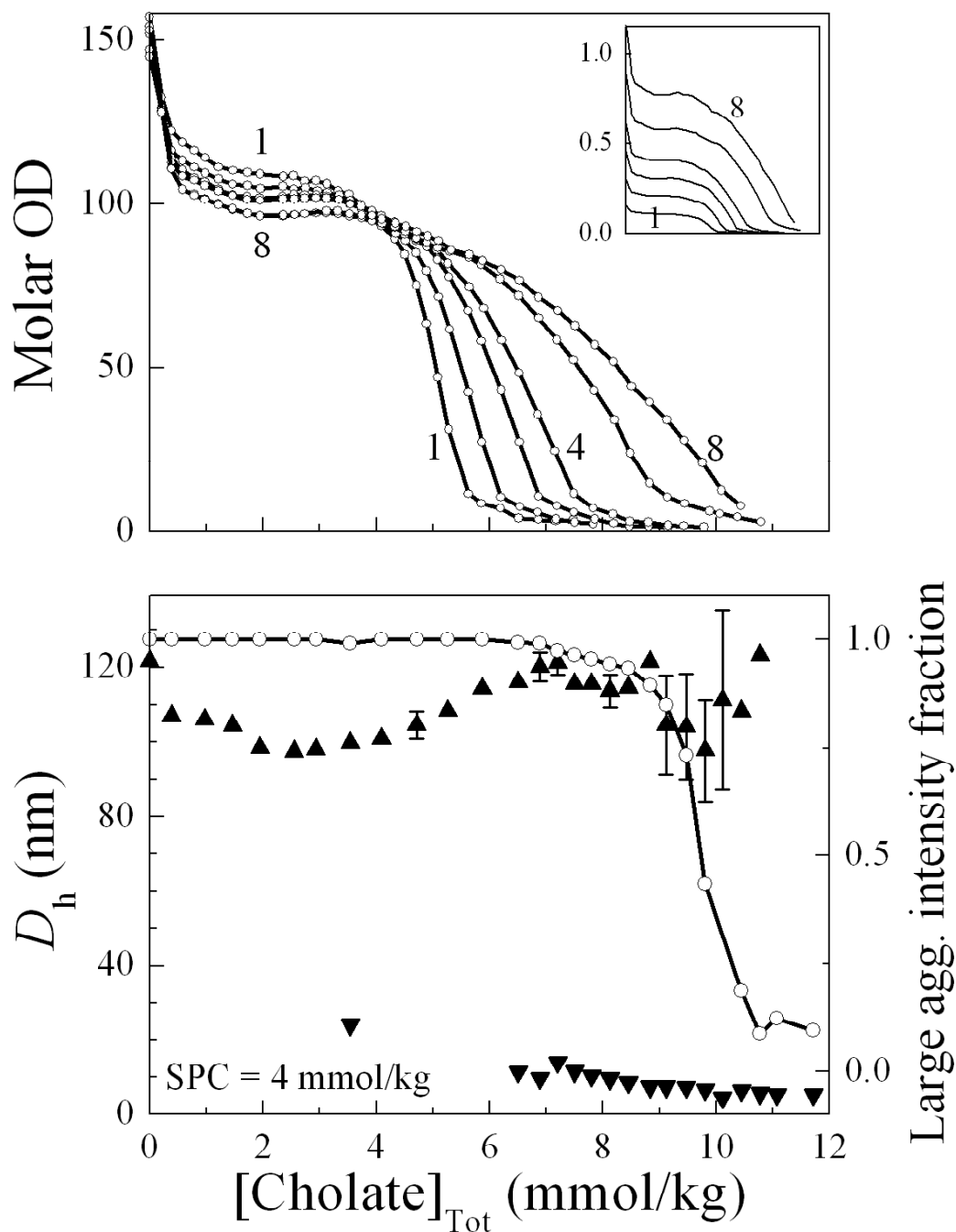


Figure 3.2 Upper panel: The molar optical density (quasi-steady state, $\lambda = 500$ nm) of the mixed aggregate suspension resulting from the LUV after addition of sodium cholate to the given total concentration. The numbers next to curves give the corresponding final phospholipid concentrations, which were 1, 2, 3, 4, 6, and 8 mmol SPC kg^{-1} . Inset: The corresponding absolute optical density. Lower panel: The mean hydrodynamic diameter of the mixed aggregates formed from the LUV (final concentration = 4.00 mmol SPC kg^{-1}) after addition of sodium cholate to the given total concentration (quasi-steady state, triangles, left axis). The diameter implied by an additional peak occurring at various positions between 300 nm and 900 nm, which is detectable in some samples with total cholate concentration above 9.00 mmol kg^{-1} , is not shown for better clarity. Circles give the intensity-normalized fraction of the peak corresponding to mixed lipid vesicles and/or to other large mixed aggregates (right axis). In both panels, each data point represents a separate preparation. The standard deviation bars are only shown when they are larger than the corresponding symbol.

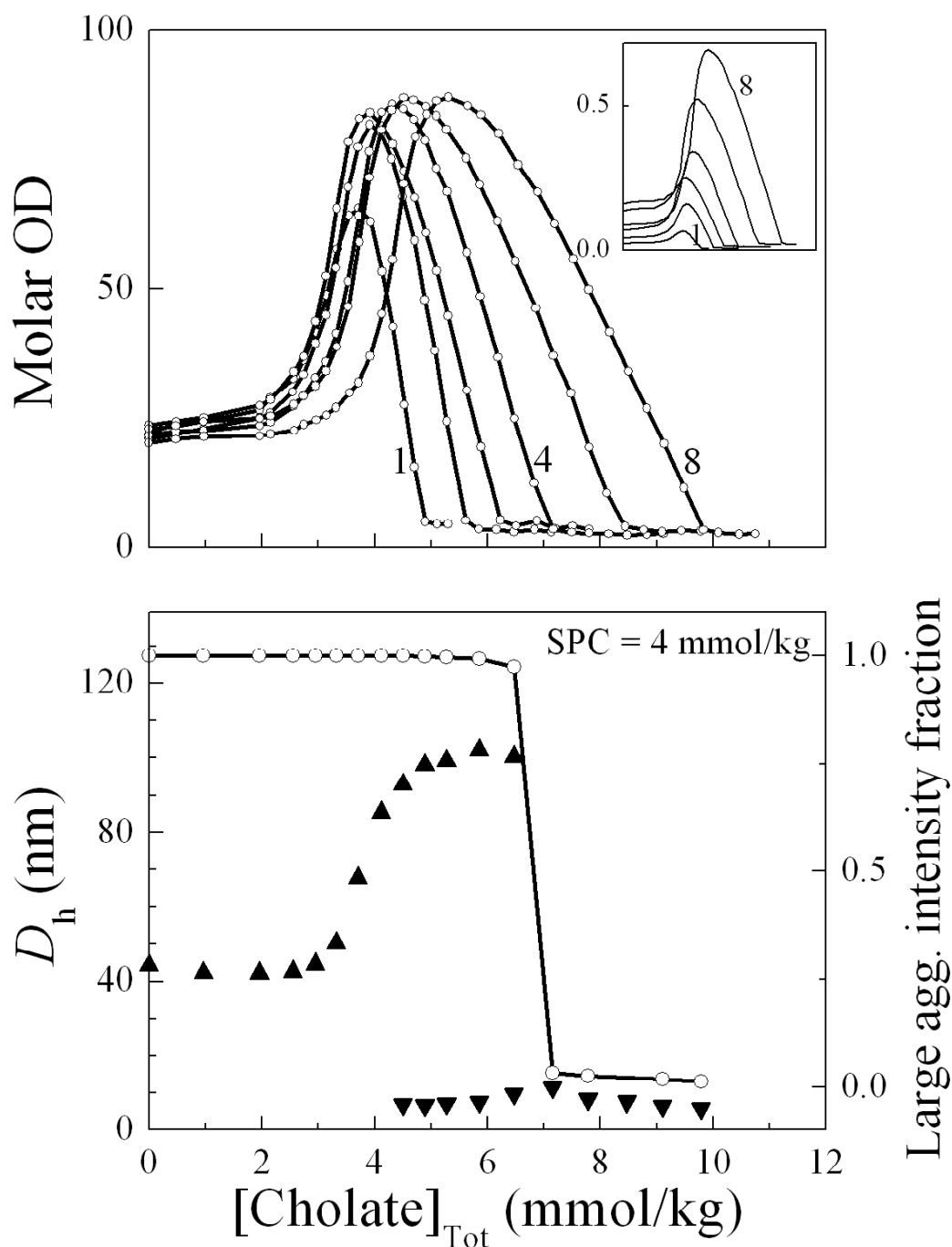


Figure 3.3 Upper panel: The molar optical density (quasi-steady state, $\lambda = 400$ nm) of the mixed aggregates suspension resulting from the SUV after addition of sodium cholate to the given total concentration. The numbers next to curves give the corresponding final phospholipid concentrations, which were 1, 2, 3, 4, 6, and 8 mmol SPC kg⁻¹. Inset: The corresponding absolute optical density. Lower panel: The mean hydrodynamic diameter of the mixed aggregates formed from the SUV (final concentration = 4.00 mmol SPC kg⁻¹) after addition of sodium cholate to the given total concentration (quasi-steady state, triangles, left axis). A peak detectable in all samples with total cholate concentration above 6.50 mmol kg⁻¹ somewhere in the range 90-350 nm is not shown for better clarity. Circles give the intensity-normalized fraction of the peak corresponding to mixed lipid vesicles and/or other large mixed aggregates (right axis). In both panels, each data point represents a separate preparation. The standard deviation is always smaller than the symbol.

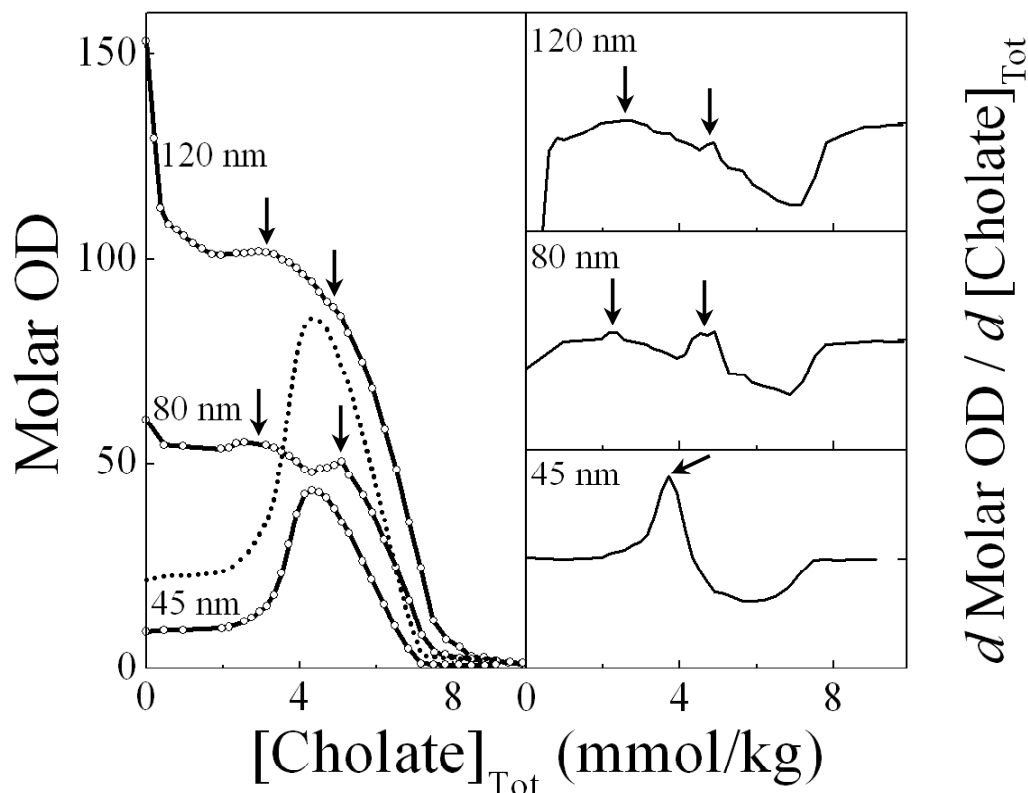


Figure 3.4 Left panel: The molar optical density (quasi-steady state, $\lambda = 500$ nm) of the mixed aggregates suspension resulting from the LUV, the IUV or the SUV after addition of sodium cholate to the given total concentration (final SPC concentration = $4.00 \text{ mmol kg}^{-1}$). The curve pertaining to the SUV was calculated from the data measured at $\lambda = 400$ nm (dashed line) assuming $\text{OD} \propto \lambda^{-w}$ and $3.023 \leq w \leq 4.000$. Right panel: The derivative of the molar optical densities shown in the left panel vs. the total cholate concentration. The arrows point to unusual changes in optical density curves.

measured optical density suggests a change in the opposite direction. Raising cholate concentration further then enlarges the mean diameter of mixed aggregates sharply, from 42 nm (essentially the starting value) to 102 nm, in qualitative agreement with the optical density data. Such changes more or less coincide with appearance of small mixed micelles.

The intensity-normalized fraction of the peak pertaining to the large aggregates falls steeply with increasing cholate concentration. The peak remains detectable at various positions between 90 nm and 350 nm, however (data not shown in Fig. 3.3 for better clarity). The average size of the small mixed phosphatidylcholine/cholate micelles is 5-11 nm. The dynamic and the static light scattering both imply similar solubilisation-endpoints.

Intermediate size vesicle (IUV) suspensions supplemented with a small amount of cholate become more transparent. We measured smaller optical density decrease with such intermediate-size (80 nm) unilamellar vesicles than with the LUV. Raising cholate concentration further triggers a complex set of optical density changes. This is reflected in at

least two well resolved, successive optical density vs. cholate concentration peaks. We detected two peaks – or more precisely: a peak with a shoulder – for the LUV as well. To determine these two peak positions for the LUV we had to take the derivative of optical density vs. total cholate concentration curve (Figs. 3.2, 3.4). Escalating cholate concentration further decreases optical density of the suspension that originally contained IUV essentially in parallel with the optical density changes observed with the LUV and SUV suspensions. The process continues until the optical density reaches a low quasi-plateau, where most lipid vesicles are transformed into small mixed micelles. The gradual solubilisation creates a “tail” at the high end of optical density vs. cholate concentration curves. The tail is more prominent for the LUV than for the IUV and is not detectable for the SUV (Figs. 3.2–3.4).

One should thus identify complete solubilisation with the cholate concentration at which the suspension optical density reaches its final low value than by extrapolating the steeply descending part of the curve toward such a value. The minimum cholate concentration needed to completely solubilise phosphatidylcholine into small mixed micelles depends on the original vesicle size. It is generally higher for larger vesicles (Figs. 3.2–3.4).

3.3.2 The time-resolved light scattering

Fig. 3.5 illustrates the temporal evolution of molar optical density of the LUV or of the SUV suspensions triggered by adding sodium cholate to the specified final concentration. The vesicle-to-micelle transformation is accordingly sensitive to the initial average vesicle size, whether measured in quasi-equilibrium (Figs. 3.2–3.4) or time-resolved (Fig. 3.5).

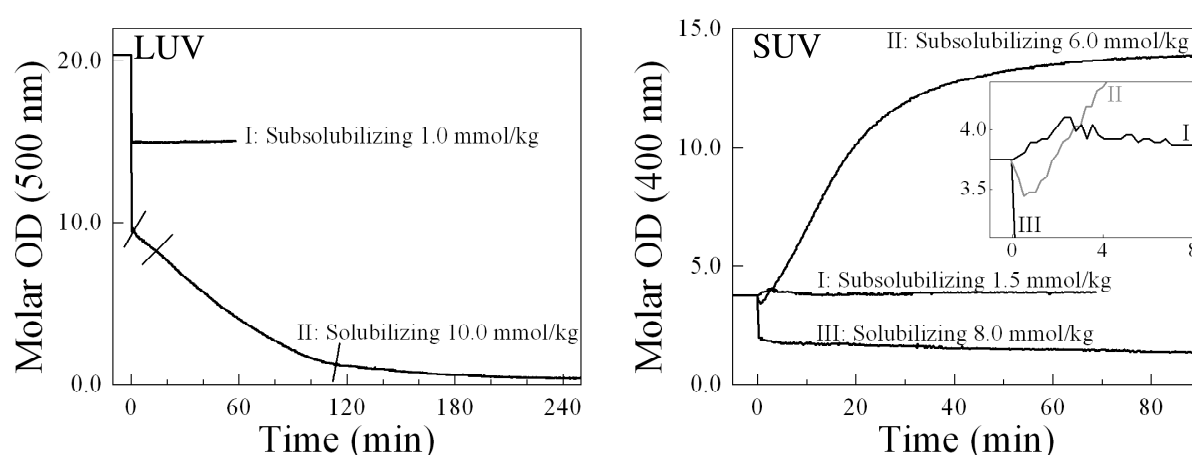


Figure 3.5 The temporal evolution of molar optical density of the LUV (left panel) or the SUV (right panel) suspensions after addition of sodium cholate to the given total concentration (final SPC concentration = 4 mmol kg⁻¹). The baselines are corrected for the dilution effect. The curve II in the upper panel is subdivided into four segments by crossing lines indicating apparent changes in optical density decrease rate. Inset: Magnification of the changes taking place during the first few minutes.

Addition of a sub-solubilising cholate amount to the LUV suspension precipitously decreases the preparation optical density. The optical density reaches a final, constant value nearly instantaneously, indicative of fast partitioning of cholate molecules between the bulk and the LUV bilayers. Addition of a solubilising sodium cholate quantity to the LUV also promptly lowers the suspension optical density to approximately half the original value. The optical density subsequently decreases gradually toward the final very low value, which is reached after approx. 3–4 hours (Fig. 3.5, left panel). The LUV solubilisation into small mixed-phosphatidylcholine-cholate micelles is thus a complex and relatively slow process.

The temporal optical density evolution in the cholate-supplemented SUV (Fig. 3.5, right panel) differs from the corresponding time-course determined for the LUV suspensions. A sub-solubilising cholate addition triggers a small increase of the SUV optical density that seamlessly transitions into a smaller secondary decrease. Higher, but still sub-solubilising, cholate concentration (corresponding to the optical density maximum in Fig. 3.3) transiently lowers the suspension optical density. The suspension optical density thereafter gradually increases until it reaches its final value, which is nearly three times higher than the original value. Introduction of a solubilising sodium cholate amount, in contrast, precipitously decreases the suspension optical density. A subsequent asymptotic approach to the final value is observed. The secondary suspension optical density decrease possibly reflects diminution of mixed amphipat micelles rather than vesicle solubilisation (cf. LUV, Fig. 3.5, left panel). We did not see the intermediate transition, characterized by the steep optical density increase, after having added the solubilising cholate amount to our preparations in a single step. The time-dependent and the continuously recorded optical density curves thus differ in this respect from the cholate concentration-dependent quasi-steady state changes illustrated in Fig. 3.3.

3.3.3 Quantitative analysis of the cholate-facilitated bilayer fluctuations

We analysed the data from Figs. 3.2 and 3.3 within the framework of the Helfrich bilayer elasticity model ^[135], which accounts for the functional dependency of the effective bilayer rigidity on the average vesicle size. This afforded the effective bilayer rigidity as a function of total cholate concentration, based on the observed LUV diameter diminution (see Appendix 3.A and Table 3.2). We then inferred the apparent size and optical density of the SUV preparations from the LUV results without making any further assumption. The qualitative agreement between the calculated and the measured results for the SUV, shown in Fig. 3.6, gives some credence to the underlying assumptions. To improve the agreement one could allow for the relatively large polydispersity of the SUV as compared with the LUV.

Table 3.2 The calculated bending rigidity, κ , of the mixed amphipat bilayers as a function of total cholate concentration. The results are derived from the LUV size changes measured with the static and the dynamic light scattering and analysed with the basic Helfrich's model (Appendix 3.A) ^[135].

[Cholate] _{Tot}	Static light scattering		Dynamic light scattering	
	Molar OD	κ [10^{-20} J ($k_B T$)]	D_h [nm]	κ [10^{-20} J ($k_B T$)]
0.000	153.004	-- ^a	121.8	-- ^a
0.383	112.509	1.031 (2.5)	107.1	0.807 (2.0)
0.973	105.622	0.846 (2.1)	106.0	0.732 (1.8)
1.464	102.489	0.783 (1.9)	104.5	0.664 (1.6)
1.947	101.072	0.766 (1.9)	98.5	0.518 (1.3)

^a We know of no published bending rigidity value for the pure SPC bilayers. The reasonably similar egg PC has $\kappa \approx 9.7$ - $13.4 k_B T$ ^[136, 137]. Reliable values for the fluid phase PCs typically range between $10 k_B T$ and $20 k_B T$, depending on chain-length and -unsaturation ^[138]. Dilinoleyl-phosphatidylcholine with four double bonds per molecule has $\kappa \approx 11 k_B T$ ^[138]. We therefore presume $\kappa \approx 15 k_B T$ (6.172×10^{-20} J) for the studied simple SPC bilayers.

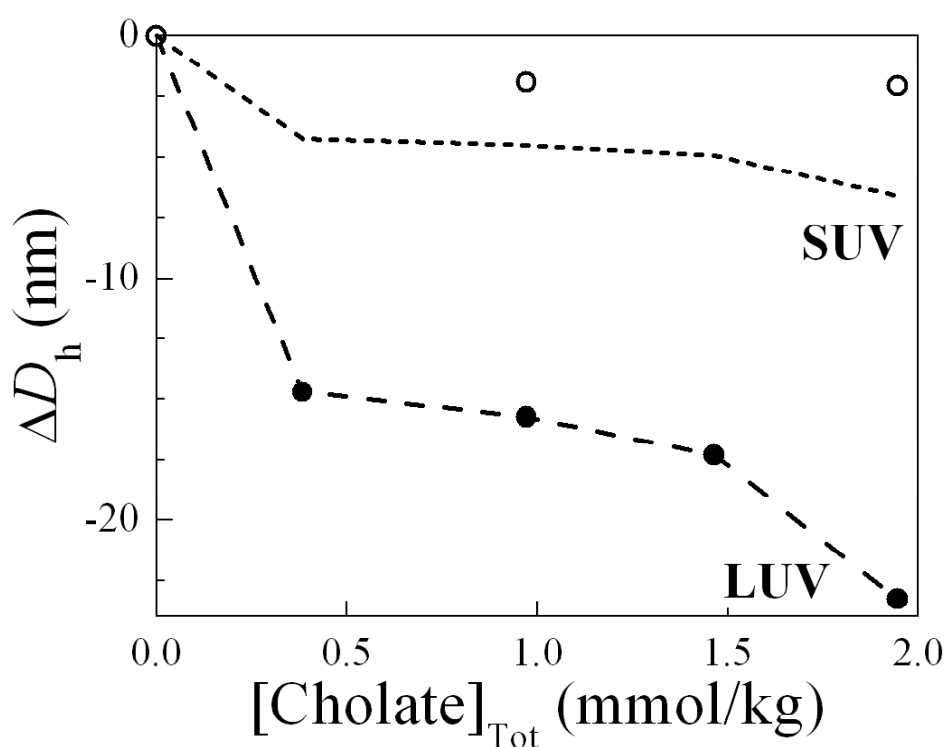


Figure 3.6 The cholate (total concentration = 0–2 mmol kg⁻¹) induced (mixed) vesicle hydrodynamic diameter changes (4.00 mmol SPC kg⁻¹). Symbols give the experimental data and lines the values calculated as is described in Appendix 3.A with the bending rigidity values given in Table 3.2. The calculation presumed the same cholate apparent partition coefficient in the LUV and the SUV bilayers at similar cholate concentration.

3.4 Discussion

3.4.1 Experimental considerations

Under the physiologic conditions cholate is essentially an anionic biosurfactant with an aqueous dissociation constant $pK_a = 4.63$ (25 °C, 150 mM ionic strength ^[139]). The apparent dissociation constant of cholate is higher, however, in the homo-aggregates that prevail above this biosurfactant CMC and in the presence of other lipids or surfactants which tend to form hetero-aggregates with this biosurfactant. The chief reasons are the lower polarity and the repulsive electrostatic potential at such aggregate surface (see Chapter 2). Our own potentiometric measurements (Chapter 2) suggest that $pK_a = 4.80$ (37 °C, 150 mM ionic strength) for an aqueous cholate solution below CMC and that cholate bound to originally electroneutral SPC bilayers has a higher $pK_a^{\text{mem}} = 6.91$ (37 °C, 150 mM ionic strength). These results agree with earlier reported ¹³C NMR measurements ^[140, 141].

Previous studies of membrane-associated cholate were conversely done nearly exclusively in a quasi-physiological range $6.5 < \text{pH} < 7.5$, i.e. around pK_a^{mem} . This focused on the physiologic cholic acid/cholate-lipid interactions but aggravated proper analysis of cholate partitioning/binding. Indeed, no previous study of which we know has treated the pH effects in such range properly (by correctly considering both the dissolved as well as the lipid-associated cholate ionisation). The variability of cholate ionisation in such pH range was in the previous publications accounted for only incompletely, if at all. The experimental pH effects on cholate ionization are greatest when $\text{pH} \approx pK_a^{\text{mem}}$, i.e. around the physiological pH range (for illustration: degree of ionisation varies between 24 – 76% at $\text{pH} = pK_a \pm 0.5$). This explains some discrepancies between the various published results. For a similar reason, the Coulomb correction in such pH range requires utmost care: incomplete cholate ionisation, a consequence of the small $\text{pH} - pK_a^{\text{mem}}$ difference, would make mathematical analysis of the resulting data much more complex.

One should also carefully consider the local pH shift, ΔpH , which results from proton attraction to the negatively charged surface. To estimate the shift, one can first employ the Gouy-Chapman approximation ^[101, 142] to calculate the electrostatic surface potential, ψ , as a function of bilayer bound cholate molecule fraction, interfacial dielectric constant, and bulk salt concentration (see Chapter 2). From the calculated interfacial electrostatic potential one can derive the pH shift originating from the Coulomb interactions: $\Delta\text{pH} = \log[\exp(-e_0\psi/k_B T)] = -e_0\psi/2.3k_B T$, where e_0 is the elementary electric charge (1.602×10^{-19} C), k_B the Boltzmann

constant ($1.38 \times 10^{-23} \text{ JK}^{-1}$), and T the absolute temperature. If the mole fraction of the negative molecules in a planar bilayer is $x_e = 0.175$, for example, the difference amounts to $\Delta\text{pH} \approx -1$; for $x_e = 0.521$ the difference is $\Delta\text{pH} \approx -2$ (both at $25 \text{ }^\circ\text{C}$, for bulk ionic strength = 150 mM , and neglecting non-Coulombic contributions).

We wished to experiment only with cholate in a well defined ionisation state. Cholate is fully charged only when the interfacial pH sufficiently exceeds the interfacial $\text{p}K_a^{\text{mem}} + 2$. One must therefore choose the bulk $\text{pH} \geq \text{p}K_a^{\text{mem}} - \Delta\text{pH} + 2$ (or 3) rather than the bulk $\text{pH} \geq \text{p}K_a + 2$ (or 3) to ensure full ionization of the biosurfactant and thus a reasonably simple mathematical analysis of experimental data. We conducted our experiments at $\text{pH} = 10.25$, which ensure $>99\%$ ionization of the dissolved as well as the aggregate-bound cholate for all the tested lipid and surfactant concentrations.

Wanting to ensure cholate equilibration in the tested suspensions, we sought to achieve constancy of the measured signal by waiting long enough. We kept in mind that the minimum required time depends on the initial vesicle size as well as on total cholate and lipid concentrations (Fig. 3.5). Cholate exchange and equilibration between an aqueous solution and a lipid bilayer can be slow at $\text{pH} = 10.25$. Addition of cholate may moreover initially (and often transiently) decrease the dispersion optical density, which subsequently re-increases, or vice versa (Fig. 3.5). Premature read-out is thus prone to produce wrong conclusions. We consequently either equilibrated each test sample until its optical density became constant, which took up to 6 hours, or else measured the full time-dependency.

We also cared about SPC hydrolysis at the high chosen experimental pH. We first calculated the rate of phosphatidylcholine degradation based on published information^[143, 144] and duly considering the local pH-shift effects. We concluded that the overall degree of lipid hydrolysis should be less than 2.5 % during the 6 hour equilibration period at $\text{pH} = 10.25$, $T = 25 \text{ }^\circ\text{C}$, $I = 150 \text{ mM}$, except when the mole fraction of bound cholate in the aggregates is less than 0.1. This would apply for our suspensions (SPC concentrations $\leq 6.00 \text{ mmol kg}^{-1}$) only if the total cholate concentration is less than 1.4 mmol kg^{-1} (see the published partition coefficient values in^[82, 145]). Such mixtures require equilibration times of a few minutes (Fig. 3.5), however. This is too short to cause considerable degradation. We furthermore checked experimentally that phospholipid hydrolysis did not play a role in our experiments. We did not detect lysophosphatidylcholine or a phosphatidylcholine concentration change in representative samples, kept at $\text{pH} = 10.25$ and $T = 25 \text{ }^\circ\text{C}$ for 6 hours. We therefore deem our results to be reliable and not falsified by phospholipid degradation.

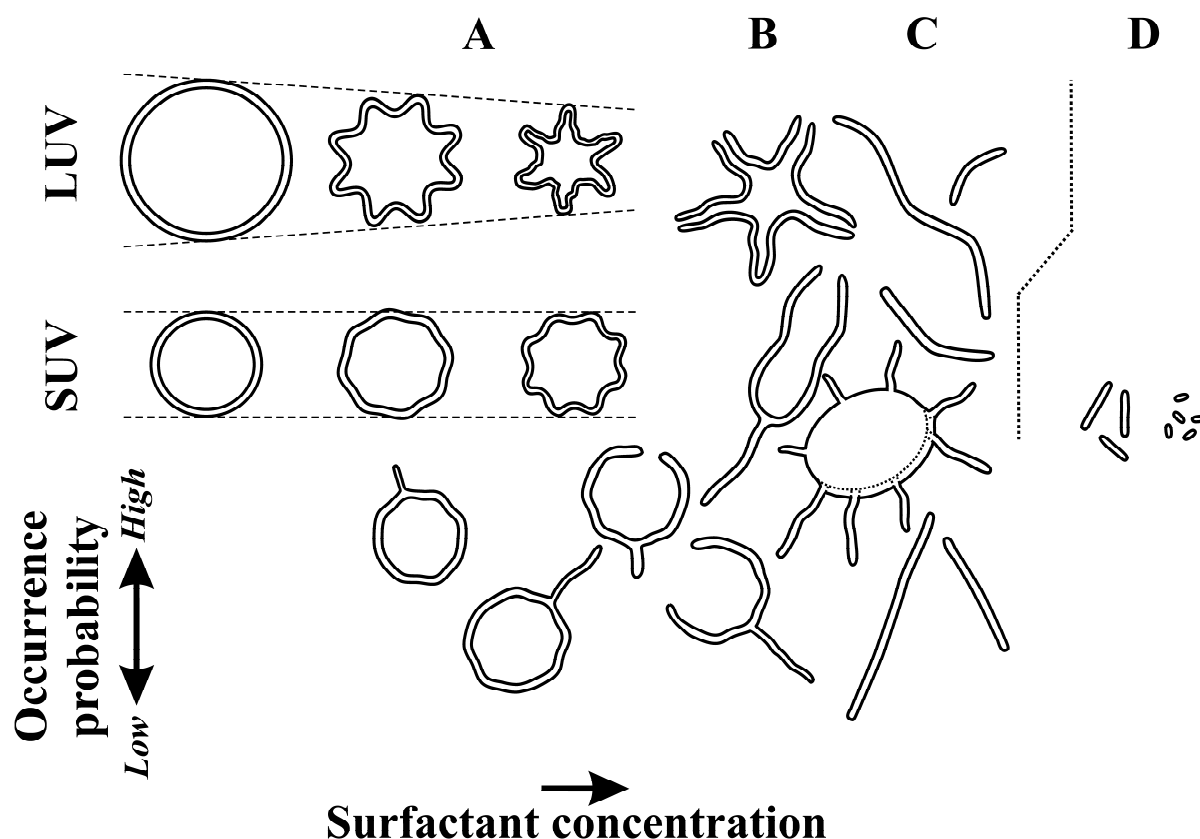


Figure 3.7 Schematic representation of the most typical structures that can appear, and typically coexist, during progressive vesicle-to-micelle transformation, and their ad hoc separation into four quasi-distinct regions: the bilayer vesicle/mixed vesicle region (A); the open, quasi-lamellar structure region (B); the long, thread-like micelle region (C); and the relatively small micelle region (D).

3.4.2 Supramolecular view of the vesicle-to-micelle transformation

The most common description of vesicle-to-micelle transformations is the “three-stage model”^[59]. According to such model, at stage I surfactant monomers partition into lipid bilayers. Higher surfactant concentration pushes the mixed amphipat suspension into stage II at which the lipid-saturated micelles coexist with the surfactant saturated vesicles. At stage III only micelles exist.

Despite its simplicity, the three stage model can describe reasonably well the basic behaviour of many lipid-surfactant mixtures. This explains the model popularity despite its restriction to just two, in detail unspecified, aggregate types: bilayer vesicles and micelles. The three stage model cannot cope with the structural diversity described by many researchers^[120, 146-148] including us. Indeed, such data suggest that surfactants solubilise bilayer vesicles in a continuous process comprising at least two sequential and partially overlapping, structurally complex, and aggregate size-dependent phenomena – one increasing and the other decreasing average mixed aggregate size (see Appendix 3.C).

Fig. 3.7, which we construed on the basis of our own and previously published findings, illustrates the most typical structures that may (co)exist during vesicle transformation into the ultimately small mixed micelles. The figure highlights the only unambiguous and common boundary in such a transition: the complete replacement of the relatively large, water-filled bilayer vesicles (whether spherical and non-perforated or not) by the much smaller and more compact micelles (whether thread-like, ellipsoid, discoid, or spherical). Any further firm subdivision is artificial, even if it facilitates underlying process description. We reduce the general, quasi “bicontinuous and parallel transformation”, which we advocate herein, to four transformation steps or regions: A, B, C, D (Fig. 3.7). We caution the reader that this serves solely better comparability with the three-stage model and that such simplified “differentiation” has no one-to-one correlation with reality. For further commentary see Appendix 3.C.

3.4.2.1 The lamellar bilayer vesicles/mixed amphipat vesicles (region A)

Low total cholate concentrations result in low degree of cholate-bilayer association. Only mixed amphipat bilayer vesicles then exists. If cholate-bilayer association is the only process involved, the average vesicle size should simply increase with cholate concentration [149]. Evans, et al. [149] showed that the surface area of a pressurised giant unilamellar vesicle increases monotonously with added/bilayer bound bile acid fraction. In reality, we measured a “richer” and vesicle size-dependent optical density vs. total (low) cholate concentration curve: the slope of our experimental curve is first steep and negative for the LUV, less negative for the IUV, and slightly positive for the SUV (Figs. 3.2-3.4).

Our dynamic and static light scattering data qualitatively agree for the SPC/cholate mixed aggregates originating from the LUV. This confirms that the apparent mean diameter of such aggregates decreases with increasing total cholate concentration (Fig. 3.2). Conversely, dynamic light scattering indicates a slight vesicle size decrease (~ 2.0 nm) for the SUV whereas static light scattering reveals a slight increase of the SUV size (Fig. 3.3). The diversity of bilayer forms, brought about by phospholipid-cholate interaction and association, evidently increases with average aggregate size even if starting vesicles are always spherical.

Surfactant insertion into a lipid bilayer lowers the resulting mixed bilayer rigidity [150, 151]. This lowers mechanical bilayer stability [149] and facilitates bilayer fluctuations [152, 153]. Hydration studies with mixed bilayers [152] and high-intensity dark-field micrographs [153] vindicate the claim. The frequency spectrum of bilayer fluctuations inevitably depends on the

average vesicle surface/size, and is more restricted for the SUV than for the LUV. The size-dependent counter-play between the bilayer expansion caused by cholate adsorption and the apparent bilayer vesicle shrinkage caused by the cholate-induced bilayer fluctuations can thus explain our quantitative conclusions summarised in Fig. 3.6. Absence of such fluctuations in mixed amphipat vesicles under tension in turn explains the monotonous size-increase with surfactant concentration reported by Evans et al. ^[149].

Surfactants insertion into lipid vesicles lowers bilayer bending rigidity ^[108, 149, 150, 154, 155]. With an improved vesicle adaptability assay, Wachter et al. ^[156] assessed the bending rigidity of SPC bilayers saturated with the non-ionic surfactant polyoxyethylene (20) oleyl ether (C_{18:1}EO₂₀) to be $\kappa \approx 2.1 k_B T$. Brown and colleagues ^[154] estimated from deuterium NMR relaxation times the bending rigidity of 2/1 dimyristoylphosphatidylcholine/C₁₂EO₈ mixed bilayers, which is also not too far from phospholipid solubilisation, to be $\kappa \approx 7 k_B T$. Evans, et al. ^[149] reported a quasi-exponential decrease of bilayer lysis-tension with increasing concentration of the trihydroxy bile acid cholylglycine in egg phosphatidylcholine giant vesicles. Their data imply bilayer bending rigidity at 5-10% of the saturation limit also to be in the 5 - 8 $k_B T$ range. Our own estimate of $\kappa \approx 2 k_B T$ (Table 3.2) for suspensions containing sub-solubilising cholate concentrations is thus probably too low.

The low calculated κ value probably points towards an inhomogeneous surfactant distribution within the fluctuating mixed amphipat bilayers ^[108, 155]. Such distribution introduces another surfactant-sensitive size dependency into the generalised Helfrich's model, in addition to the size-dependent fluctuations cut-off. A finite surface area namely restricts the range of all possible vesicle membrane fluctuations. In turn, this diminishes the maximum surfactant induced κ -decrease and the resulting apparent vesicle size reduction. Laterally and transversely non-uniform surfactant distribution can account for the 25% discrepancy between the cholate-induced size-changes of the LUV and SUV, which we measured with the dynamic light scattering (Fig. 3.6). To explain the much larger difference between the static light scattering changes measured with the LUV or SUV one would have to allow for the putative cholate-induced bilayer refractive index change (e.g. due to bilayer hydration) and/or for bilayer thickness variation.

Restricted transbilayer “flip-flop” of charged cholate molecules through SUV bilayers could play a role as well. Cabral et al. ^[157] assessed the rate of cholate flip-flop through egg phosphatidylcholine SUV bilayers ($2r \approx 23$ nm) with ¹³C NMR; charged cholate molecules at pH = 10 practically failed to traverse such bilayers (flip-flop half-time > 24 h at 35 °C).

Donovan and Jackson ^[158] investigated surfactant flip-flop through LUV bilayers by monitoring the time-dependency of surfactant binding. They determined the transverse time of the ionized bile salts across lipid bilayers to be hours or even minutes ^[158]. The discrepancy could reflect vesicle size differences; the relatively high SUV bilayer curvature creates a less favourable surrounding (higher chemical potential) on its inside for charged surfactant molecules as compared with the outer bilayer half. Cholate resistance towards “running uphill” through the SUV bilayer could explain the slower flip-flop through the highly curved SUV bilayers as compared with the “flatter” LUV bilayers. The same applies to some of the differences illustrated in Figures 3.2-3.4, at least.

3.4.2.2 Vesicle poration, partial fragmentation, and/or fusion/appearance of thread-like micelles (region B)

Differently large vesicles respond differently to cholate incorporation in the intermediate cholate concentration range (for illustration: total cholate concentration of 2.0–4.5 mmol kg⁻¹ for the samples with 4.00 mmol SPC kg⁻¹; Figs. 3.2–3.4). Optical density of the originally LUV and the originally IUV suspensions responds to surfactant concentration within such range only little. For a better resolution we differentiated each curve (Fig. 3.4, right panels). This revealed existence of two optical density maxima for the LUV (for the LUV, better described as a peak and a shoulder) as well as for the IUV. Optical density of the suspensions that originally contained the SUV, in contrast, comprised only one optical density peak (within resolution of our measurements).

The first maximum in our optical density vs. cholate concentration curves is visible at approximately the same total surfactant concentration for the originally LUV and IUV suspensions (Fig. 3.4). This probably refers to domination of the surfactant-dependent bilayer expansion over the surfactant-induced bilayer fluctuations. Our data can neither support nor exclude the previously proposed shedding of SUV during solubilisation of the originally LUV/IUV, which had been implied for phosphatidylcholine-octylglucoside mixtures ^[148, 159].

The shoulder on the molar optical density vs. total cholate concentration curve measured with the LUV, the second peak on such curve for the IUV, and the single peak on the curve for the SUV all correspond. They coincide with the first detection of the small mixed micelles by the dynamic light scattering. Such “secondary characteristics” thus reveal onset of vesicles solubilisation; they depend on initial vesicle size, showing a higher maximum for the smaller than the larger vesicles.

The dynamic light scattering data basically confirm the static light scattering results. The peak corresponding to the large aggregates shifts upward with increasing cholate concentration (Figs. 3.2-3.3). The dynamic light scattering detects small mixed micelles at lower cholate concentrations for the SUV than for the IUV or the LUV. The dynamic light scattering delivers imprecise information about the large aggregates size within the bilayer presolubilisation region (i.e. at the higher end of the intermediate cholate concentration range; Fig. 3.2); this suggests co-existence of various aggregate forms (Fig. 3.7). An additional peak between 90 nm and 900 nm in some measurements (data not shown) supports the conclusion.

Walter et al. ^[120] investigated the intermediate structures in vesicle-micelle transition of the phosphatidylcholine SUV–cholate system with cryo-transmission electron microscopy. For the cholate concentrations which increase the suspension optical density most steeply (the ascending part of the optical density “peak”) they observed open vesicles, collapsed vesicles, bilayer patches, and cylindrical (i.e. thread-like) micelles. They also detected some cylindrical mixed micelles at the broken vesicles/large bilayer sheets rims. They reported maximum prevalence of such micelles for the cholate concentrations corresponding to the optical density peak illustrated in our Figures 3.2–3.4. Vinson et al. ^[148] saw similar structures with the LUV phosphatidylcholine-octylglucoside mixtures.

Long et al. ^[116] investigated the reverse process, i.e. the intermediate aggregate formation by diluting lecithin-bile salt micellar suspensions. Their small-angle neutron diffraction data revealed coexistence of bilayer vesicles and cylindrical micelles even in some samples for which dynamic light scattering measurements showed just one kind of aggregates. They explained such an observation at intermediate cholate concentrations by postulating that micelles are too long to be distinguishable from bilayer vesicles with visible light. Existence of such micelles or (micellar) protrusions emerging from bilayers can also explain the variable peak position which we uncovered for the large aggregates with the dynamic light scattering.

In our view, the changes occurring in this region, as reflected by the static and dynamic light scattering measurements (Figs. 3.2-3.4), result from gradual bilayer enrichment and finally saturation with the surfactant and the accompanying diversity of transformations in the mixed aggregates morphology. The two major types of such morphological changes are: vesicles poration/rupture into quasi-lamellar open vesicles/bilayer fragments, on the one hand, and retro-fusion of the resulting fragments or vesicles into larger aggregates, on the other hand. The most frequent minor and/or transient change is protrusion formation, which is optically indistinguishable from vesicle fragments fusion. It stands to reason that the

protrusion formed before creation of transbilayer pores (which permit fast cholate migration across bilayers) involve just the outer bilayer half; subsequently (after the porated or fragmented bilayers stop acting as barriers to cholate transport) both bilayer halves are involved. Complexity of the derivatives shown in Fig. 3.4 supports our overall picture of vesicle-to-micelle transformation (Fig. 3.7). The process of surfactant-induced vesicle solubilisation is evidently not interchangeable with vesicle formation triggered by decreasing surfactant concentration. Whereas the latter is exclusively controlled by the mixed aggregate composition ^[160-163] and its change-rate ^[164, 165], the former depends on the starting aggregate size, on total amphipat concentration, and also on equilibration time (Figs. 3.2-3.5).

Arguably, each aggregate shape transformation triggers a time- and morphology-dependent local cholate concentration adjustment, whether this is directly observable or not. Such an adjustment can give an explanation for the initial light scattering variation and/or its transience in the case of the SUV (see Fig. 3.5), as well as the preferential occurrence of the long cylindrical mixed micelles at bilayer fragments' rims (see the previous paragraphs and ^[120]). Optical light scattering was only capable of directly and unambiguously confirming the local cholate concentration increase in the caps of the thread-like, mixed phosphatidylcholine-cholate micelles (Fig. 3.8). The size- and time-dependency of the scattered light characteristics measured with the partially solubilised phospholipid (Figs. 3.2-3.5) implies a similar cholate local concentration adjustment in the pre-solubilisation region.

The propensity for large aggregate or protrusion formation depends on several parameters. The starting aggregate size can obscure their identification, however: the mixed aggregates originating from the LUV scatter light similarly as the original LUV while the aggregate stemming from the SUV scatter light more than the original SUV. The optical density peak is consequently higher for vesicles with smaller initial size (Fig. 3.4). The shape and the height of the molar optical density peak depend also on lipid concentration (Fig. 3.3), which can affect the transformations kinetics as well. Aggregate proximity/higher amphipat concentration raises the probability for aggregate-cholate and aggregate-aggregate collisions and fusion. This facilitates protrusion growth and aggregate remerging/fusion. This offers an explanation for the flatter optical density vs. cholate concentration curve measured for higher lipid concentrations. The starting aggregate size effect on the average inter-aggregate distance also explains why such effect is greater for the LUV than for the SUV (Figs. 3.2, 3.3).

We warn against accepting any reported “vesicle saturation” with a surfactant boundary, derived effective bound molar fraction, x_e^{sat} , or associated effective bound molar

ratio, R_e^{sat} , as a reliable and/or definitive value, at least when such parameters are derived from optical light scattering data. Long cylindrical, thread-like micelles may coexist with mixed vesicles at surfactant concentrations below the optical density “peak”. Some open vesicles may coexist with cylindrical micelles at the beginning of the ascending part of the optical density peak. The starting size also influences the optical density peak position (see Figs. 3.4, 3.9 and Appendix 3.C).

3.4.2.3 Thread-like micelles fragmentation/small micelle formation (region C)

Increasing cholate concentration well above the concentration that ensures full bilayer fragmentation shortens the thread-like micelles. The cylindrical micelles ultimately transform into smaller ellipsoidal or (quasi) spherical micelles. In parallel, the suspension optical density decreases, diagnostic of (nearly) complete lipid solubilisation. The weight fraction of the peak corresponding to the small micelles in the dynamic light scattering data concurrently increases and the weight fraction of the peak corresponding to the large/long aggregates decreases (Figs. 3.2–3.3, lower panels, right axes). The suspension characteristics which we determined in region C are qualitatively interchangeable with those previously measured with visible light scattering and neutron diffraction in the opposite direction (dilution of small mixed micelles)^[160].

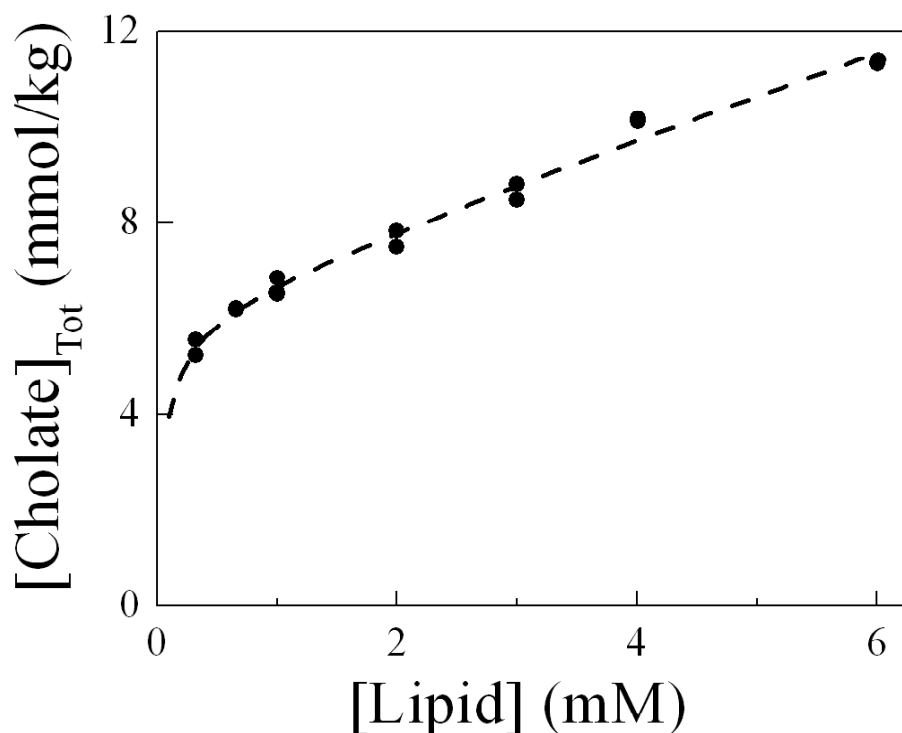


Figure 3.8 Total cholate concentration required to solubilise the LUV bilayer vesicles into small mixed amphipat micelles as a function of total phospholipid (SPC) concentration. Symbols represent the experimental static light scattering data. The dashed curve illustrates the best fit, derived from the model proposed by Roth et al.^[166] with the modifications described in Appendix 3.B.

The tailing of optical density vs. cholate concentration curve depends on the initial vesicle size. It is more prominent for the mixtures originating from the LUV (data published by de la Maza and Parra^[115], who worked with larger vesicles than our LUV show also tailing) than for the preparations originating from the IUV (Figs. 3.2, 3.4). Our data pertaining to the SUV show no clear tailing (Figs. 3.3-3.4), however.

Temporal evolution of the optical density measured after addition of a solubilising cholate amount elucidates the observation. LUV solubilisation, as reflected in the temporal optical density evolution, follows a similar pattern as the cholate-induced concentration-dependent changes (Figs. 3.2, 3.5); one can thus view the LUV solubilisation as a gradual but rather rapid aggregate transformation. In contrast, the SUV seem to be less capable of accommodating large amounts of cholate, probably owing to their smaller average surface area that only tolerates a limited fluctuation spectrum; the flip-flop hampering surface curvature influence may play a role as well. Small vesicles therefore break more directly into cylindrical micelles, and require a lower total cholate concentration for solubilisation, than the LUV (Figs. 3.2-3.4).

Turbidimetric/optical density measurements can quantitatively and reliably reveal the effective surfactant mole fraction above which only small ellipsoidal or spherical micelles exist, x_e^{sol} . We evaluated such fraction from the data given in Figs. 3.2-3.4 with the mathematical approach of Roth et al.^[166]. We thus accounted for the micelles finite size and the inhomogeneous end-caps (inhomogeneous with regard to surfactant and lipid distributions at both ends as compared to the central part of each cylindrical micelle). We moreover included the Columbic interactions into the model (Appendix 3.B) and present the results in Table 3.3 and Figure 3.8. The predicted non-linearity at low lipid concentrations agrees with the experimental data measured with the LUV ($< 1.00 \text{ mmol SPC kg}^{-1}$). We were unable to collect similar data with the dilute SUV preparations owing to their low scattering intensity. From the whole experimental data set we were nonetheless able to conclude that the effective surfactant molar ratio in the aggregates at complete lipid solubilisation is lower for the SUV than for the LUV: $R_e^{\text{sol-SUV}} < R_e^{\text{sol-LUV}}$. The size of the small mixed micelles existing at such boundary is larger for the SUV ($2r = 11.4 \text{ nm}$) than for the LUV ($2r = 4.5 \text{ nm}$). This supports our earlier conclusion that the SUV, having a relatively small surface area and restricted flip-flop ability, can tolerate less cholate than the LUV. The SUV therefore require less cholate to break into larger and having lower R_e mixed micelles (see Figs, 3.2–3.4, Tab. 3.3).

Table 3.3 The mixed aggregate composition, the corresponding aqueous cholate concentration, and the cholate partition coefficient into the mixed aggregates at the total cholate concentration ensuring complete soybean phosphatidylcholine solubilisation into small mixed micelles. The values are derived from the static light scattering data using the analytical approach described by Roth et al. [166], with allowance for the Coulomb interactions (see Appendix 3.B).

	R_e^{sol}	[Cholate] _w ^a [mM]	[Cholate] _{w,int} ^a [mM]	A_w ^a [mM ^{3/2}]	R^2	P_0 ^a
LUV	0.877 ± 0.058	6.65 ± 0.35	0.23 ± 0.01	0.88 ± 0.26 ^d	0.988	1.1×10^5
SUV ^b	0.709 ± 0.042	4.31 ± 0.35	0.16 ± 0.01	0.10 ± 0.35	0.996	1.4×10^5
SUV ^c	0.624 ± 0.020	5.08 ± 0.07	0.23 ± 0.00	0.88	0.994	9.5×10^4

^a [Cholate]_w is the bulk aqueous cholate concentration. [Cholate]_{w,int} is the aqueous cholate concentration at the aggregate surface, corrected for the Coulomb effect. A_w is a fitting parameter that takes into account the micellar scission energy. P_0 is the partition coefficient of cholate into the phosphatidylcholine-cholate mixed aggregates.

^b Owing to the low scattering intensity of the aggregates formed from the SUV, we were unable to conduct measurements with highly diluted SUV. This precluded us from studying the deviation from linearity at low lipid concentrations and thus from accurately calculating the A_w value for the SUV; the mentioned value is likely underestimated.

^c Calculations done with the A_w derived from the LUV data, for at least a rough approximation.

^d The result corresponds to a scission energy of $2\epsilon = 9.5 - 10.0 k_B T$, if $0.2 < R_e^{sat} < 0.35$. Roth et al. [166] obtained a higher value for octylglucoside ($19.5 k_B T$) and heptylglucoside ($18.0 k_B T$), suggesting comparably high spontaneous curvature of cholate containing aggregates.

3.4.2.4 The small mixed micelles (region D)

A high cholate concentration in a lipid suspension ensures that all the aggregated amphipat molecules will form only small mixed amphipat micelles (Fig. 3.2–3.3). Adding a solubilising cholate amount to either the LUV or the SUV triggers a slow terminal optical density decrease, diagnostic of the progressive micelle size diminution (Fig.3.5).

3.5 Conclusions

We characterised various soybean phosphatidylcholine-sodium cholate mixtures with light scattering techniques to elucidate the vesicle-to-micelle transformation. More specifically, we used the static, the time-resolved, and the dynamic light scattering to investigate the equilibrium optical density and aggregate size in soybean phosphatidylcholine suspensions supplemented with cholate. We worked with unilamellar vesicles blended with fully ionised sodium cholate at pH = 10.25. We varied lipid concentration, starting with the lowest properly explorable value of 1 mmol kg⁻¹, and also changed cholate concentration, as have been done by many researchers before. Additionally and importantly, we explored the starting vesicle size ($2r_v = 45 \text{ nm} - 120 \text{ nm}$) effect to explore the influence of lipid bilayer curvature on lipid solubilisation and mixed micelle formation.

The size-standardised measurements uncovered several new features. Our results reveal that the cholate-induced initial vesicle size decrease is greater for the originally large than for the originally small vesicles. Quantitative data analysis confirmed that the difference is mainly due to broadening of shape-fluctuation spectrum with mixed bilayer vesicle surface area. In contrast, the suspension optical density increase before complete vesicle solubilisation is bigger for the originally small than for the originally large vesicles. The small, 45 nm vesicles require around 30% less cholate for complete solubilisation than the larger, 120 nm vesicles. The former, nonetheless, form approximately twice as large mixed micelles.

Simple phenomenological parameterisation of optical density *vs.* total cholate concentration curves suggests that vesicle-to-micelle transformation size-wise predominantly involves two largely parallel phenomena. The first is associated with an apparent, gradual aggregates size decrease; it involves progressive bilayer destabilisation, bilayer fragments- and detached thread micelles-formation, and finally micellar diminution. The second is associated with an apparent aggregate size increase; it mainly involves bilayer fusion or vesicles reformation and/or formation of bilayer-attached threadlike protrusions.

From the morphological viewpoint, originally spherical vesicles arguably become aspherical upon surfactant incorporation. The reason is cholate-dependent bilayer softening and enhancement of bilayer fluctuations. The mixed amphipat vesicles compensate for some of the excess area that results from the surfactant binding to the outer bilayer half by forming thread-like protrusions. Arguably, the surfactant concentration at the end of any relatively thin structures is higher than in the less curved cylinder or bilayer part. It furthermore stands to reason that aggregate surface fluctuations provoke inhomogeneous surfactant distribution in the mixed amphipat bilayers. The resulting local surfactant accumulation catalyses trans-bilayer pore formation, more frequently and/or likely when lipid-solubilising surfactant concentration is approached. Strong fluctuations/protrusions and/or pores increase the probability for, first, vesicle re/fusion and, second, bilayer fragmentation.

The popular three-stage bilayer solubilisation model is convenient but potentially misleading. For better accuracy and broader applicability we advocate replacing it with the more realistic continuous (i.e. bicontinuous and parallel) transformation model. The starting vesicle size effect precludes determination of the bilayer-saturating surfactant concentration from light scattering or size measurements alone. More fundamentally, any such concentration value is an ill-defined quantity, due to inhomogeneous surfactant distribution along (and across) the mixed aggregate surface.

The presumption of constant and laterally uniform aggregate composition is not tenable in any solubilisation model, owing to interdependency of local aggregate composition and curvature. This causes small vesicles to solubilise more readily than large bilayer aggregates, and then surprisingly to form (at least for some time) relatively larger mixed micelles. Inhomogeneous surfactant distribution moreover helps explain – together with the bilayer barrier to surfactant transport – why a vesicle-to-micelle transition is not simply a mirror picture of micelle-to-vesicle transformation. The latter is dominated and controlled by the final mixed aggregate composition. It thus produces similar final results so long as the rate of relative composition change remains the same. In contrast, the surfactant-induced vesicle solubilisation typically creates a plethora of intermediate structures. Some are long-lived and differ in size despite their similar composition. Kinetic trapping is an additional, and relatively more likely, problem encountered during vesicle solubilisation studies.

Appendix 3.A: Dependence of the effective bilayer rigidity on the average vesicle size

To account for the dependence of the apparent vesicle size changes upon addition of low cholate concentration (region A) on initial vesicle size (Figs. 3.2–3.4) we used the mathematical approach derived by Helfrich ^[135]. This describes the dependency of effective bilayer rigidity on average vesicle size and allows calculation of the softening-induced vesicle size diminution.

Let us write the effective mole fraction of the bilayer associated cholate as:

$$x_e = \frac{C_b}{C_b + L} \quad (3.1)$$

and the mole fraction of free cholate in the bulk aqueous solution as:

$$x_w = \frac{C_w}{C_w + W} \approx \frac{C_w}{W} \quad (3.2)$$

where C_b is the bound and C_w the bulk cholate concentration. L is the molar lipid and $W \approx 55.5$ M the molar water concentration. The commonly used definition of the apparent cholate partition coefficient between water and lipid bilayer is:

$$P = \frac{x_e}{x_w} \quad (3.3)$$

It should be replaced, in the simplest approximation, with an expression that allows for the

Coulomb interaction:

$$P_0 = \frac{x_e}{x_w \cdot \exp[-\varphi]} \quad , \quad (3.4)$$

where φ is the bilayer surface dimensionless electrostatic potential. Eq. 3.4 conveniently accounts for the Coulomb interactions between the charged cholate molecules in solution and the charges at bilayer surface through the electrostatic Boltzmann factor in the denominator. φ is related to the surface electrostatic potential, ψ , through the relation $\varphi = ze_0\psi/k_B T$. In turn, the electrostatic surface potential depends on cholate concentration at the bilayer surface (for further details see ^[101, 142, 167]). For the sake of simplicity, we did not separate the effect of the Coulomb interactions on cholate partition coefficient and true bending rigidity of bilayers. We rather used their apparent values, as follows. Based on published and on our own unpublished data we estimated the intrinsic ‘partition coefficient’ of cholate in SPC lipid bilayers to be around 1.5×10^4 . From this value we calculated the apparent cholate partition coefficient as a function of lipid and total cholate concentration, allowing for the Coulomb electrostatic effects ^[101, 142, 167].

By combining Eqs. 3.1–3.3 and considering the relationship $C_{\text{Tot}} = C_b + C_w$ we got:

$$P \approx \frac{C_b W}{(C_b + L) C_w} \approx \frac{C_b W}{(C_b + L) (C_{\text{Tot}} - C_b)} \quad . \quad (3.5)$$

We calculated C_b as a function of total cholate concentration by numerically solving Eq. 3.5 and then derived x_e from Eq. 3.1.

To assess the cholate concentration effect on the average vesicle size we first expressed the total (outer + inner) surface area of a spherical bilayer vesicle as:

$$A_v = 4\pi r_v^2 + 4\pi(r_v - d_{\text{mem}})^2 \quad , \quad (3.6)$$

r_v being the vesicle radius and d_{mem} the bilayer thickness (which we took to be 4 nm, as is appropriate for a typical fluid-phase phospholipid). From the starting vesicle area, $A_{v,0}$ (i.e. A_v at $x_e = 0$) we obtained the average number of lipid molecules in each vesicle

$$N_L = \frac{A_{v,0}}{A_L} \quad (3.7)$$

in terms of the average area per lipid molecule in a bilayer, A_L , which we took to be 0.65 nm^2 . The number of cholate molecules in each mixed bilayer vesicle is then:

$$N_C(x_e) = \frac{x_e}{1 - x_e} N_L \quad . \quad (3.8)$$

A_C is the average area of a cholate molecule in the mixed bilayer ($A_C \approx 0.40 \text{ nm}^2$). The total (outer + inner) surface area of a mixed bilayer vesicle is correspondingly:

$$A_v(x_e) = \left[1 + \frac{x_e}{(1 - x_e)} \frac{A_C}{A_L} \right] A_{v,0} \quad . \quad (3.9)$$

Calculation of a mixed, spherical vesicle diameter, or radius, as a function of bilayer associated cholate concentration can be done by numerically solving Eq. 3.9 after inserting $A_{v,0}$ and $A_v(x_e)$ from Eq. 3.6.

We finally refined the apparent mixed bilayer vesicle size calculation by using the mathematical approach introduced by Helfrich ^[135]. We accordingly took the difference between the intrinsic and the apparent outer surface of a bilayer vesicle to be:

$$A_{v, \text{outer}} - A_{v, \text{outer, app}} = r_v^2 \frac{k_B T}{2\kappa} \ln M \quad . \quad (3.10)$$

k_B is the Boltzmann constant ($1.38 \times 10^{-23} \text{ JK}^{-1}$), T the absolute temperature, and κ the intrinsic, “true” mixed bilayer bending rigidity (which is a function of the cholate concentration in the bilayer).

In the spirit of the Helfrich model we identified the total number of modes on a vesicle with $M = N_C/2 + N_L$, thus clarifying that this quantity depends on cholate concentration in the bilayer as well. By rewriting Eq. 3.10 in terms of the vesicle radius we obtained:

$$r_v^2 - r_{v, \text{eff}}^2 = r_v^2 \frac{k_B T}{8\pi\kappa} \ln M \quad , \quad (3.11)$$

$$r_{v, \text{eff}} = r_v \left[1 - \frac{k_B T}{8\pi\kappa} \ln M \right]^{0.5} \quad . \quad (3.12)$$

We combined Eqs. 3.5, 3.9, and 3.12 to analyse the dynamic light scattering data. For this purpose, we programmed a Mathcad calculation sheet (Mathcad version 11.0b, Mathsoft Engineering & Education, Inc., Cambridge, MA, USA). We show the results in Table 3.2 and Figure 3.6.

To analyse the static light scattering data with the same mathematical approach one must consider that the intensity of the light scattered by an aggregate particle is a power-function of the average (presumably spherical) aggregate radius ^[168]. We calculated the

corresponding exponent within the framework of the Rayleigh-Gans-Debye approximation (see Chapter 4) to be 3.00–3.33 for vesicles with average radius in the range 60–50 nm.

Appendix 3.B: The small mixed micelles composition at the total cholate concentration that ensures complete lipid solubilisation

We used the mathematical model developed by Roth et al. ^[166] to determine the molecular composition of the mixed aggregates comprised of the solubilised phospholipid and cholate molecules. The model accounts for the finite size of the thread-like micelles and also considers the inhomogeneous cholate distribution between the central micelle part and the end-caps. The total surfactant concentration

$$C_{\text{Tot}} = C_w + \left[\frac{L_M}{L} R_e^{\text{sol}} + \left(1 - \frac{L_M}{L}\right) R_e^{\text{sat}} \right] L - \frac{A_w}{\alpha^{0.5} L^{0.5}} \quad (3.13)$$

is a function of the bulk surfactant concentration, C_w , the total lipid concentration, L , and the solubilised (i.e. micellar) lipid concentration, L_M . R_e^{sat} defines the maximum achievable surfactant molar ratio in a vesicle bilayer (i.e. the saturation limit) and R_e^{sol} the surfactant molar ratio ensuring complete lipid solubilisation into mixed micelles within the framework of a three-stage solubilisation model. The effective surfactant molar ratio in an aggregate is generally given by: $R_e = C_b/L$, where C_b is the lipid associated (i.e. bound) surfactant concentration.

A_w is an adjustable parameter that takes into account the scission energy ^[166]. Scission of a thread-like micelle is a physical process resulting in creation of two end-caps. To create an end-cap from the cylindrical part of a micelle an energy ϵ is required; the energy 2ϵ is thus called the scission energy ^[169]. According to Kozlov et al. ^[170] and Roth et al. ^[166], the scission energy should be qualitatively smaller for a surfactant with a higher spontaneous curvature, which typically corresponds to shorter hydrocarbon chains. For a surfactant requiring lower scission energy the phase boundaries should deviate from the straight line over a broader concentration range, beginning already at high lipid concentrations and extending toward the low concentrations end ^[166].

An alternative form of Eq. 3.13, written in terms of the relative lipid concentration in micelles, $\alpha = L_M/L$, is:

$$C_{\text{Tot}} = C_w + \left[\alpha R_e^{\text{sol}} + (1 - \alpha) R_e^{\text{sat}} \right] L - \frac{A_w}{\alpha^{0.5} L^{0.5}} \quad (3.14)$$

Eq. 3.14 is useful for fitting data measured with aggregates of known and constant composition. Our turbidimetric measurements can quantitatively and reliably reveal only the effective surfactant molar ratio in the small micellar aggregates, R_e^{sol} , for which $\alpha = 1$; thus:

$$C_{\text{Tot}} = C_w + R_e^{\text{sol}} L - \frac{A_w}{L^{1/2}} \quad (3.15)$$

The negatively charged cholate molecules in mixed amphipat aggregates affect the surfactant distribution between micelles/vesicle bilayers and bulk solution. To assess more properly the association (expressed here for the sake of convenience as partition coefficient) of cholate in the tested aggregates we included the Coulomb interactions into our data analysis (but neglected for the sake of simplicity all the non-Coulomb effects). To this effect, we expressed the surface charge density

$$\sigma(R_e) = ze_0 \frac{R_e}{A_L + R_e A_C} \quad (3.16)$$

as a function of the aggregate bound, charged surfactant valence, $z = -1$, the molar ratio of the charged surfactant in the aggregate, R_e , the elementary electric charge, $e_0 = 1.602 \times 10^{-19}$ C, the area per surfactant molecule in the mixed aggregates, A_C , and the area per lipid molecule in the mixed aggregate, A_L .

Another important system descriptor is the Debye screening length, λ_D , which describes the electrostatic interactions reach. For a symmetric monovalent (i.e. 1:1) electrolyte solution with the bulk salt concentration C_{el} one can express the Debye length as:

$$\lambda_D = \sqrt{\frac{\varepsilon_0 \varepsilon_r k_B T}{2000 e_0^2 N_A C_{\text{el}}}} \quad (3.17)$$

ε_0 is the permittivity of free space (8.8542×10^{-12} As/Vm), ε_r the relative permittivity (i.e. the dielectric constant) of the bulk solution, k_B the Boltzmann constant, T the absolute temperature, and N_A the Avogadro's number (6.02205×10^{23} mol⁻¹).

For a spherical surface (the simplest possible proxy for the small mixed micelles) in a 1:1 electrolyte the relationship between the electrostatic potential and the surface charge density is ^[171]:

$$\sigma = \frac{\varepsilon_0 \varepsilon_b k_B T}{\lambda_D e_0} \cdot 2 \sinh\left(\frac{\varphi}{2}\right) \cdot \left[1 + \frac{2\lambda_D}{r_v \cosh^2\left(\frac{\varphi}{4}\right)} + \frac{8\lambda_D^2 \ln\left(\cosh\left(\frac{\varphi}{4}\right)\right)}{r_v^2 \sinh^2\left(\frac{\varphi}{2}\right)} \right]^{0.5} \quad (3.18)$$

ϵ_b is the local dielectric constant near the surface associated charges and φ the normalized dimensionless electrostatic potential at the micellar surface. We used Eq. 3.18 to calculate φ and then the surface electrostatic potential, $\psi = \varphi k_B T / ze_0$, from the surface charge density, σ (for the much larger, and thus quasi-planar, bilayer vesicle surface one would have to use the corresponding Gouy-Chapman expression for a planar surface instead of Eq. 3.18; see Chapter 2). The effective mole fraction of cholate in the mixed aggregates, x_e , the cholate mole fraction in the bulk solution, x_w , and the cholate partition coefficient in the mixed micelles is then derivable from Eqs. 3.1, 3.2, and 3.4, respectively.

Appendix 3.C

Our experimental data suggest that the structural conversions observed with the mixed phosphatidylcholine-cholate aggregates could involve two bicontinuous, parallel aggregate size changes. To corroborate the plausibility of such notion, and to mimic the measured optical density vs. total cholate concentration curves, we combined two sigmoidal functions, each with the following basic mathematical form:

$$f(x, x_0, S) = \frac{1}{1 + \exp[S(x - x_0)]} \quad (3.19)$$

We assumed the first sigmoidal function to be centered around x_0 and to have the width described by S . We postulated the second sigmoidal curve to have a width different by dS and to be shifted relative to the first curve by dx_0 , i.e. we assumed the second curve centre to be at $x_0 + dx_0$ and the second curve width to be $S + dS$. We moreover postulated the second sigmoidal function to differ from the first one in height by a factor n , by writing:

$$f_{1+2}(x, x_0, S, dx_0, dS, n) = f(x, x_0, S) - n \cdot f(x, x_0 + dx_0, S + dS) \quad (3.20)$$

We then assigned different *ad hoc* values to each adjustable parameter of such *purely phenomenological* model. Certain tested parameter combinations simulated qualitatively each curve form those found in our static light scattering data, as is illustrated in Fig. 3.9.

We do not doubt that we could achieve an even closer match by optimising the adjustable parameter values. This proves to us that a simple combination of two parallel processes – one increasing and one decreasing the average aggregate size – can explain the main features of the cholate-induced vesicles transformation into small mixed amphipat micelles. To elucidate the finer features, such as tailing, further and/or more complicated processes need to be invoked.

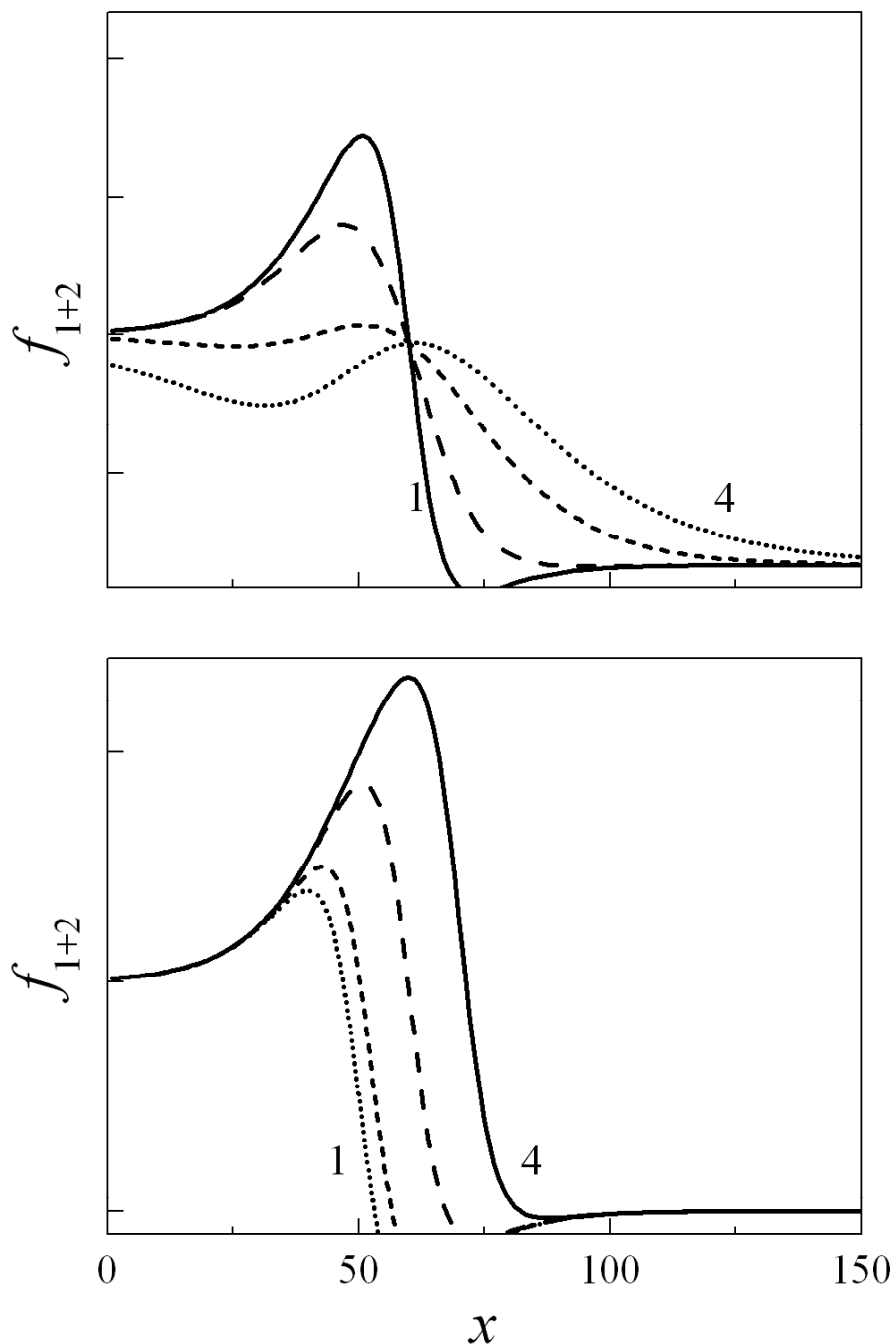


Figure 3.9 The sum of two sigmoidal curves, described by Eqs. 3.19–3.20, can mimic all the basic forms of the experimental optical density vs. cholesterol concentration curves which we measured. More specifically, we always used $n = 1.5$ together with $x_0 = 50$, $S = 0.1$, $dx_0 = 10$, and $dS = -0.05$, -0.025 , 0.05 , and 0.2 (for the curves 1 to 4, respectively) to generate the set of curves shown in the upper panel or $x_0 = 50$, $S = 0.1$, $dx_0 = 0$, 2.5 , 10 , and 20 (for the curves 1 to 4, respectively), and $dS = 0.2$, to create the set of curves in the lower panel.

4 Turbidity spectroscopy for characterization of submicroscopic drug carriers, such as nanoparticles and small lipid vesicles*

Contents

4.1	Introduction	67
4.2	Theory	69
4.2.1	Description of a light scattering particle suspension	69
4.2.2	Theory of light scattering	70
4.2.3	Size distribution	73
4.3	Materials and Methods	74
4.3.1	Materials	74
4.3.2	Preparation of lipid vesicles	74
4.3.3	Monitoring effect of cholate on lipid vesicles	75
4.3.4	Turbidity/optical density measurements	76
4.3.5	Dynamic light scattering (photon correlation spectroscopy)	76
4.4	Results and Discussion	77
4.4.1	Characteristics affecting turbidity of a nanosized particle suspension	77
4.4.2	Characterization of real lipid vesicle suspensions	86
4.4.3	Monitoring small size changes (effect of cholate on size of lipid vesicles)	89
4.4.4	Experimental recommendations and limitations	89
4.5	Conclusions	91
	Appendix 4.A	92
	Appendix 4.B	93
	Appendix 4.C	94

* This chapter was published as: M.M.A. Elsayed, G. Cevc. Turbidity spectroscopy for characterization of submicroscopic drug carriers, such as nanoparticles and lipid vesicles: Size Determination. Pharm. Res. In Press.

4.1 Introduction

Submicroscopic particles/aggregates, such as nanocrystals^[20, 172], nanoparticles^[15, 16], polymeric micelles^[12], nanoemulsions^[18-20], or lipid bilayer vesicles (liposomes), are gaining popularity in the pharmaceutical field. For example, lipid bilayer vesicles are now often used in drug delivery, gene therapy, diagnostics^[10, 11], and as membrane models^[173]. Size and size distribution critically influence all applications of submicroscopic particles and are particularly important in the pharmaceutical field. A plethora of techniques has been used to study size of particulate drug carriers, but only a few such techniques found their way out of specialized laboratories.

The most obvious and conceptually simplest method for studying shape, size, and size distribution of submicroscopic particles is electron microscopy. The method is costly, laborious, and skill-demanding, however. It involves analysis of particles outside their actual dispersion medium and is often subject to sample perturbation and preparation artifacts. It moreover requires taking and inspecting many electron micrographs to gain a representative result. Electron microscopy is therefore mainly employed in research, especially for studying particles with an unusual or changing shape, or else a broad size distribution. Other kinds of high resolution microscopy, such as the scanning tunneling microscopy^[174] or the atomic force microscopy^[175, 176], which can resolve structures at nanometer or sub-nanometer scale, are even more expensive and complex to deal with.

Some scattering techniques can also highlight carrier size and shape characteristics. The explorable length-scale depends primarily on the employed light/radiation wavelength. The small-angle scattering of X-rays and neutrons typically resolves structures measuring 1 nm to 100 nm in size^[30-35]. Such limited explorable size, the high cost of the involved equipment, and/or the scarcity of suitable radiation sources restricts applicability of such scattering techniques in the pharmaceutical field. Submicroscopic, nanosized (the word “nanosized” herein implies diameters between 10 and a few hundred nanometers) drug carriers are thus typically characterized with the longer optical/visible wavelengths.

The dynamic light scattering (DLS), also known as quasi-elastic light scattering or photon correlation spectroscopy (PCS), is currently the most popular method for measuring size of submicroscopic particles, including nanosized drug carriers^[27-29]. The technique requires no special skill to use. However, it does involve not inexpensive instruments that are therefore not broadly accessible. Furthermore, it typically takes at least 30 seconds and often

longer to collect data for a single good-quality measurement; dynamic light scattering therefore cannot monitor rapid size changes. Finding a less costly, more accessible, and potentially faster method for size characterization of colloidal drug carriers is thus desirable.

The static light scattering (SLS) can also provide information about size and, to an extent, shape of light scattering particles. Extraction of such information normally involves analyzing the angular dependency of light scattering. The Guinier-plot (approximation for small-angle data^[177]) or the Zimm-plot^[178, 179] affords the scatterer radius of gyration^[180-183]. Fitting the angular dependency of the scattered light intensity, $I(\theta)$, with a suitable form-factor and size distribution function reveals the underlying size distribution. Such fitting can provide information about the scattering particle structure, e.g. spherical shell/lipid vesicle bilayer thickness^[183]. Combining the Zimm-plot and the Rayleigh-Gans-Debye approach provides more accurate values for these particle characteristics^[184]. A combination of light scattering with flow field-flow fractionation yields absolute size distributions^[185]. All these analytical procedures involve analysis of angular dependency of light scattering and thus depend on special and expensive pieces of equipment, specifically a goniometer or an array-detector.

Heller and colleagues quite early^[186-189] proposed using differential turbidity spectra — or in other words wavelength dependency of light scattering — for size characterization of submicroscopic particles. The concept relies on dependency of the scattering vector, $q(\theta, \lambda) = (4\pi n/\lambda) \cdot \sin(\theta/2)$, on both the scattering angle, θ , and the incident light wavelength, λ , n being the dispersion medium refractive index.

Analysis of turbidity spectrum, $\tau(\lambda)$, which for a non-absorbing sample corresponds to extinction spectrum, is attractive for several reasons: *i*) it requires only a simple, broadly accessible UV-Vis spectrophotometer to collect experimental data; *ii*) it allows monitoring of size-changes on time scale of the order of 5-10 seconds with a conventional spectrophotometer and much faster with an instrument equipped with a multi-channel detector; *iii*) the method is simple yet sensitive. All these advantages notwithstanding, turbidity spectrum analysis attracted little attention to date, especially in the field of drug carrier research. Only a few practical characterization attempts were published to date^[168, 190-192] and at least for lipid vesicles were quantitatively unsuccessful; this is possibly due to some underlying theoretical and/or experimental problems. We considered these problems and in this publication show how turbidity spectrum analysis can be successfully applied in the pharmaceutical field for purpose of particulate drug carrier characterization.

In this chapter we first scrutinize the theoretical background of turbidity spectrum analysis within the framework of the Rayleigh-Gans-Debye approximation. We study effects of colloidal suspension characteristics on $\tau(\lambda)$ and provide all equations necessary for extracting the most relevant characteristics from such spectra. We illustrate the advocated analytical method using lipid bilayer vesicle suspensions. In so doing, we also address effects of bilayer thickness and lamellarity on turbidity spectra. We juxtapose the outcome of turbidity spectrum and corresponding dynamic light scattering analyses for the various lipid vesicle suspensions to prove excellent match between results of both analytical approaches.

4.2 Theory

4.2.1 Description of a light scattering particle suspension

A homogeneous spherical particle is completely described as a light scatterer in terms of its refractive index, n_p , and radius, r . The latter defines the scatterer surface area, $A = 4\pi r^2$, and volume, $V = (4\pi/3)r^3$. The number concentration of such homogeneous particles in suspension, i.e. the number of spherical particles per unit volume of the suspension, is then

$$N_p = \frac{C}{V\rho} \quad , \quad (4.1)$$

C being the particle material concentration (*weight/volume*) and ρ the particle density.

Describing a hollow sphere/spherical shell as a light scatterer requires knowledge of the core and the shell refractive indices, n_{core} and n_{shell} , the shell outer radius, r_{shell} , and the shell thickness, d_{shell} . If one uses the corresponding shell volume, $V = (4\pi/3)(r_{\text{shell}}^3 - r_{\text{core}}^3)$, with $r_{\text{core}} = r_{\text{shell}} - d_{\text{shell}}$, in Eq. 4.1, one can also calculate the number concentration of hollow spheres/spherical shells in a suspension from the expression.

Vesicles are exemplary hollow spherical particles. Mathematical description of bilayer vesicles as spherical shells uses the vesicle/particle outer radius, r_v , the number of bilayers/shells per vesicle/particle, $l \geq 1$, the bilayer/shell thickness, d_b , the inter-bilayer/-shell water layer thickness, d_w , and the lipid/shell refractive index, n_L , as vesicle characteristics. If we identify the innermost bilayer/shell with $x = 1$ and the outermost bilayer/shell with $x = l$, the outer radius of the x -th bilayer/shell is given by:

$$r_{x,\text{out}} = r_v - [(l - x)(d_b + d_w)] \quad . \quad (4.2)$$

The inner radius of the same bilayer/shell is accordingly:

$$r_{x,\text{in}} = r_{x,\text{out}} - d_b \quad (4.3)$$

The total (outer + inner) surface area of all bilayers/shells in a vesicle/particle is thus

$$A_{L,v} = 4\pi \sum_{x=1}^{x=l} [r_{x,\text{out}}^2 + r_{x,\text{in}}^2] \quad (4.4)$$

For a single-bilayer (unilamellar) vesicle or a single-shell particle Eq. 4.4 simplifies to:

$$A_{L,v} = 4\pi [r_v^2 + (r_v - d_b)^2] \quad (4.5)$$

The number concentration of bilayer vesicles/spherical shell particles in a suspension becomes:

$$N_v = \frac{N_A A_L L}{A_{L,v}} \quad (4.6)$$

where N_A is the Avogadro's number ($6.02205 \times 10^{23} \text{ mol}^{-1}$), A_L the average area of (lipid) molecules forming bilayers/shells, and L the molar concentration of such, essentially water insoluble, molecules. Phosphatidylcholine molecules in a fluid/liquid crystalline phase typically occupy an area $0.55 \text{ nm}^2 \leq A_L \leq 0.70 \text{ nm}^2$ [193-195]. In the gel phase the area is appreciably smaller and is normally in the range $0.42 \text{ nm}^2 \leq A_L \leq 0.55 \text{ nm}^2$. One can follow Luzzati by identifying the molecular area upper limit with $A_L = 2V_L/d_b$, i.e. by postulating constancy of the easily measurable volume of a single lipid molecule, V_L . Some area and volume data for different phospholipids, phases, and temperatures were published [196].

4.2.2 Theory of light scattering

We herein analyze turbidity spectra within the framework of the Rayleigh-Gans-Debye approximation (RGDA). One fundamental assumption of the approximation is absence of a significant light "phase shift", or expressed mathematically: $2ka(m-1) \ll 1$. $k = 2\pi n/\lambda$ is the propagation constant in the dispersion medium, n the dispersion medium refractive index, and λ the incident light wavelength in vacuum. a is a characteristic dimension of the light scattering particle; for a sphere it denotes the radius r . $m = n_p/n$ is the particle-to-dispersion medium relative refractive index, with n_p denoting the scattering particle refractive index. In practice, this means that the RGDA is only valid for scattering particles much smaller than $\lambda/[n(m-1)]$. The size range amenable to the RGDA correspondingly widens when the dispersion medium refractive index approaches the scattering particle refractive index, i.e. $m-1 \rightarrow 0$ (see Appendix 4.A). When the RGDA basic condition is not met, one must revert to the more general and exact, but also more complex, Mie-theory of light scattering [197, 198].

Within the framework of the Rayleigh-Gans-Debye approximation, the scattered light

intensity can be written as ^[168, 197-199]:

$$I(\theta, \lambda) = I_0 N \left(\frac{3\pi V}{d} \right)^2 \left(\frac{n(\lambda)}{\lambda} \right)^4 \left(\frac{m^2(\lambda) - 1}{m^2(\lambda) + 2} \right)^2 \left(\frac{1 + \cos^2 \theta}{2} \right) P(\theta, \lambda) \quad (4.7)$$

I_0 is the incident light intensity and N the number concentration of the light scattering particles (i.e. N_p or N_v). V is the volume of an individual particle, d the observation distance (the distance between the scattering particle and the detector), and θ the scattering angle. The scattering or form factor, $P(\theta, \lambda)$, allows for the scattering particle finite size and non-sphericity; it accounts for interference of light scattered from different parts of the scattering particle. This factor consequently depends on the scattering particle shape. We provide the form factors for the most frequently studied particle geometries (homogeneous sphere, concentric/coated sphere, and hollow sphere/spherical shell) in the following subsections. The form factors pertaining to other particle geometries (e.g. cylinder, rod, disk, cube, ellipsoid, or prolate vesicle) were published ^[181, 184, 197, 200]. Scattering particles appreciably smaller than the incident light wavelength have $P(\theta, \lambda) \rightarrow 1$ (i.e. Rayleigh scattering). Wavelength and angular dependency of light scattered by such particles thus contains no structural information.

Integrating over the surface of a sphere yields the total light scattered or turbidity ^[168]:

$$\begin{aligned} \tau(\lambda) &= 2.303 \text{OD} \\ &= 9N\pi^3 V^2 \left(\frac{n(\lambda)}{\lambda} \right)^4 \left(\frac{m^2(\lambda) - 1}{m^2(\lambda) + 2} \right)^2 \int_0^\pi (1 + \cos^2 \theta) P(\theta, \lambda) \sin \theta \, d\theta \quad (4.8) \end{aligned}$$

OD is the optical density, as measured with a spectrophotometer for a non-absorbing sample in a cuvette with 1 cm path-length*.

Turbidity is a power function of the incident light wavelength: $\tau(\lambda) \propto \lambda^{w(\lambda)}$ ^[186, 187]. The wavelength exponent function is thus

* Optical density is the quantity commonly provided by a spectrophotometer according to the definition: $\text{OD} = -\log(I_T/I_0)/b$, where I_T is the transmitted light intensity, I_0 the incident light intensity, and b the optical path-length. OD corresponds to extinction or total attenuation, i.e. due to absorption + scattering. The term “absorbance”, A , denotes attenuation due to absorption; i.e. for an absorbing, non-scattering sample $\text{OD} = A$. The term “turbidity”, τ , denotes attenuation due to scattering. The most common definition of turbidity, which we use herein, is based on the natural rather than the decadic logarithm: $\tau = -\ln(I_T/I_0)/b$, however. Accordingly, for a non-absorbing sample $\tau = 2.303 \text{OD}$. Before applying Eq. 4.8, one should thus check whether the used spectrophotometer provides τ or OD, as defined here.

$$w(\lambda) = \frac{d \log \tau(\lambda)}{d \log \lambda} \quad (4.9)$$

Considering the wavelength dependency of the refractive indices (see Appendix 4.B and Appendix 4.C) as well as the pertinent form factor one can differentiate Eq. 4.8 to get

$$w(\lambda) = -4 + \frac{d}{d \log \lambda} \log \left[n^4(\lambda) \left(\frac{m^2(\lambda) - 1}{m^2(\lambda) + 2} \right)^2 \int_0^\pi (1 + \cos^2 \theta) P(\theta, \lambda) \sin \theta d\theta \right]. \quad (4.10)$$

4.2.2.1 Homogeneous sphere

For an optically homogeneous sphere the form factor is ^[197, 201, 202]

$$P(\theta, \lambda) = \left[\frac{3(\sin qr - qr \cos qr)}{q^3 r^3} \right]^2 \quad (4.11)$$

The scattering vector is again $q(\theta, \lambda) = (4\pi n/\lambda) \sin(\theta/2)$. Such form factor applies to spheres or reasonably homogeneous spherical hetero-aggregates, such as particles in a nanoemulsion.

4.2.2.2 Sphere coated with a spherical shell

For a spherical particle comprising two concentric and optically homogeneous regions, i.e. a spherical core of one medium encased in a concentric spherical shell of a different medium, the form factor is ^[197, 203]

$$P(\theta, \lambda) = \left[\frac{3 \left[(\sin qr_{\text{shell}} - qr_{\text{shell}} \cos qr_{\text{shell}}) + \frac{m_{\text{core}}(\lambda) - m_{\text{shell}}(\lambda)}{m_{\text{shell}}(\lambda) - 1} (\sin qr_{\text{core}} - qr_{\text{core}} \cos qr_{\text{core}}) \right]}{q^3 r_{\text{shell}}^3} \right]^2. \quad (4.12)$$

r_{core} denotes the core radius, r_{shell} the shell outer radius, m_{core} the core-to-dispersion medium relative refractive index, and m_{shell} the shell-to-dispersion medium relative refractive index. When Eq. 4.12 is used, the total volume: $V = (4\pi/3) r_{\text{shell}}^3$ and the shell-to-dispersion medium relative refractive index, i.e. $m(\lambda) = m_{\text{shell}}(\lambda)$, must be used in Eqs. 4.7, 4.8, and 4.10.

4.2.2.3 Hollow sphere / spherical shell

The form factor pertaining to a shell-coated sphere simplifies to the expression for a hollow sphere/spherical shell when $m_{\text{core}} = 1$:

$$P(\theta, \lambda) = \left[\frac{3(\sin qr_{\text{shell}} - qr_{\text{shell}} \cos qr_{\text{shell}} - \sin qr_{\text{core}} + qr_{\text{core}} \cos qr_{\text{core}})}{q^3 r_{\text{shell}}^3} \right]^2. \quad (4.13)$$

Again, the total sphere volume: $V = (4\pi/3) r_{\text{shell}}^3$ and the shell-to-dispersion medium relative

refractive index, i.e. $m(\lambda) = m_{\text{shell}}(\lambda)$, must be used in Eqs. 4.7, 4.8, or 4.10 §.

The form factor described by Eq. 4.13 applies to spherical unilamellar lipid bilayer vesicles. For such vesicles the parameter r_{shell} in Eq. 4.13 corresponds to the vesicle radius, $r_{\text{shell}} = r_v$. The aqueous core radius is $r_{\text{core}} = r_v - d_b$, d_b being bilayer thickness. $m(\lambda) = m_{\text{shell}}(\lambda)$ is the bilayer-to-dispersion medium relative refractive index.

For a multilamellar vesicle the form factor becomes ^[168]:

$$P(\theta, \lambda) = \left[\frac{3 \sum_{x=1}^{x=l} [\sin qr_{x,\text{out}} - qr_{x,\text{out}} \cos qr_{x,\text{out}} - \sin qr_{x,\text{in}} + qr_{x,\text{in}} \cos qr_{x,\text{in}}]}{q^3 r_v^3} \right]^2, \quad (4.14)$$

$r_{x,\text{out}}$, $r_{x,\text{in}}$, x , and l being defined in the “Description of light scattering particle suspension” section. In combination with Eq. 4.14, the total vesicle volume and the shell-to-dispersion medium relative refractive index must be used in Eqs. 4.7, 4.8, or 4.10.

4.2.3 Size distribution

To describe light scattering by a real population of particles one must consider particle size distribution as well. Several distribution functions were proposed to meet the goal. Herein we are using the log-normal distribution function:

$$f^{\text{Num}}(r) = \frac{1}{r\delta\sqrt{2\pi}} \exp\left[-\frac{[\ln r - \mu]^2}{2\delta^2}\right], \quad (4.15)$$

which postulates that the size logarithm, $\ln r$, rather than the size itself, r , is normally distributed. μ is the mean value of $\ln r$ and δ the corresponding standard deviation of $\ln r$. Correspondingly, $\mu = \ln \bar{r}_g$ and $\delta = \ln \sigma_g$, where \bar{r}_g is the geometric mean and σ_g the geometric standard deviation of r . Eq. 4.15 satisfactorily describes size distribution in a suspension of natural particles ^[197] and is also acceptable for lipid vesicles.

Popular alternatives to the log-normal distribution function are the Weibull ^[185, 205, 206] and the gamma ^[182] distribution functions. While the log-normal (Eq. 4.15) and the gamma distribution functions are two-parametric and thus simpler to use, the Weibull distribution

§ It is noteworthy that such a form factor is commonly ^[181-184, 191, 200, 204] written with $q^3(r_{\text{shell}}^3 - r_{\text{core}}^3)$ instead of $q^3 r_{\text{shell}}^3$ in the denominator. In contrast to our treatment for the particles as hollow spheres, the same particles are in such approach treated as spherical shells; shell volume: $V = (4\pi/3)(r_{\text{shell}}^3 - r_{\text{core}}^3)$ must then be used in Eq. 4.7 or 4.8.

function is three-parametric and can thus provide more robust and correct estimates for the lower size limit. Compared to the log-normal distribution, the Weibull distribution thus better describes especially small (e.g. sonicated ^[205, 206] or extruded ^[185]) liposome size distribution.

Allowance for scatterer size distribution transforms Eqs. 4.7 and 4.8 into:

$$I(\theta, \lambda) = \frac{I_0 N}{2} \left(\frac{3\pi}{d} \right)^2 \left(\frac{n(\lambda)}{\lambda} \right)^4 \left(\frac{m^2(\lambda) - 1}{m^2(\lambda) + 2} \right)^2 \int f^{\text{Num}} V^2 (1 + \cos^2 \theta) P(\theta, \lambda) dr \quad , \quad (4.16)$$

$$\tau(\lambda) = 9N\pi^3 \left(\frac{n(\lambda)}{\lambda} \right)^4 \left(\frac{m^2(\lambda) - 1}{m^2(\lambda) + 2} \right)^2 \int f^{\text{Num}} V^2 \int_0^\pi (1 + \cos^2 \theta) P(\theta, \lambda) \sin \theta d\theta dr \quad . \quad (4.17)$$

One should be mindful of the r -dependency of f^{Num} , V , and P too. The corresponding number concentration for homogeneous spheres and spherical shells (cf. Eq. 4.1) is

$$N_P = \frac{C}{\rho \int f^{\text{Num}} V dr} \quad . \quad (4.18)$$

For spherical vesicles (cf. Eq. 4.6) this more specifically means:

$$N_v = \frac{N_A A_L L}{\int f^{\text{Num}} A_{L,v} dr} \quad . \quad (4.19)$$

Hitherto, we have considered only the number-weighted size distribution. Researchers commonly express size distributions derived from light scattering experiments as intensity-weighted size distributions, however. To get the latter kind of distribution, one should divide the contribution of each scatterer with radius r to the sample turbidity by the overall suspension turbidity. If one then fits the intensity-weighted size distribution to the log-normal distribution function, one gets the intensity-weighted mean scatterer size.

4.3 Materials and methods

4.3.1 Materials

We used the same materials as those described in Chapter 3.

4.3.2 Preparation of lipid vesicles

We prepared unilamellar vesicles of different size by extrusion. In brief, we dissolved the necessary phospholipid amount in chloroform, in a 500 mL round-bottom flask. We then removed the solvent at 50 °C in a rotary evaporator to get a thin lipid film, which we hydrated at the same temperature with distilled water. This prompted spontaneous formation of multilamellar vesicles. The resulting suspension had total phospholipid concentration of 120

mg/g (~ 150 mmol/kg).

To produce the unilamellar vesicles “V80” we extruded the original multilamellar vesicle suspension 20 times through a set of polycarbonate membranes with 80 nm pores under 1.5 MPa nitrogen gas pressure. To gain the smaller unilamellar vesicles “V50” we extruded the “V80” suspension 16–20 times through a set of polycarbonate membranes with 50 nm pores under nitrogen gas pressure of 2.1 MPa. To obtain the unilamellar vesicles “V30” we finally extruded the “V50” suspension 16–20 times through a set of polycarbonate membranes with 30 nm pores under nitrogen gas pressure of 2.5 MPa. To prepare suspensions with different lipid concentrations, we diluted the starting suspensions with distilled water, pre-filtered through syringe filters with 200 nm pore diameter.

We verified that the described extensive extrusion did not eliminate a considerable amount of lipid material, i.e. did not appreciably reduce the final lipid concentration. For this purpose, we measured phosphatidylcholine concentration in representative preparations with HPLC. We used an in-house modification of the method described by Nasner and Kraus^[128] with refractive index detection^[129].

4.3.3 Monitoring effect of cholate on lipid vesicles

We applied the turbidimetric method to monitor lipid vesicle size changes induced by addition of sodium cholate as a function of the surfactant concentration. We first prepared a series of vesicle suspensions with 8 mmol lipid/kg in an aqueous carbonate buffer (50 mM, pH = 10.25) adjusted with NaCl to a final ionic strength of 150 mM. We always prepared fresh samples immediately before starting an experimental series to minimize lipid degradation/hydrolysis at the high chosen pH. We moreover used the HPLC assay described earlier to confirm that no detectable phosphatidylcholine hydrolysis took place during experiments: the lysophosphatidylcholine level in several representative samples kept at pH = 10.25 and $T = 25$ °C for 6 hours was below the HPLC method detection limit. Total phosphatidylcholine concentration also did not change. We prepared a series of sodium cholate solutions/suspensions with different concentrations in a similar buffer and adjusted each preparation to a final ionic strength of 150 mM with NaCl.

We then mixed an aliquot of the test vesicle suspension with an equal volume of the appropriate sodium cholate solution/suspension and stirred the blend thoroughly. All mixtures had final lipid concentration of 4 mmol/kg and final cholate concentration between 0.0 and 1.2 mmol/kg. We equilibrated all mixtures at room temperature (~ 25 °C) for 3 hours, which

sufficed for reaching quasi-equilibrium (a constant optical density reading) in the studied cholate concentration range ^[207]. Finally, we recorded the suspensions optical density spectra.

4.3.4 Turbidity/optical density measurements

We measured optical density (extinction) spectra mainly with a Shimadzu UV-1601 double-beam UV-Vis spectrophotometer equipped with a 6 position, automated sample changer and the Shimadzu UVProbe version 2.0 software (Shimadzu Corporation, Kyoto, Japan); we will refer to this instrument as “Spectrophotometer A”. To test the general validity and ruggedness of the method, we also recorded optical density spectra of selected samples with a PerkinElmer Lambda EZ 201 UV-VIS spectrophotometer equipped with the PESSW version 1.2 (Revision E) software; we will refer to this instrument as “Spectrophotometer B”. We confirmed negligible light absorbance by SPC in the employed concentration range at $\lambda > 400$ nm. We then recorded optical density spectra at $\lambda = 400\text{--}600$ nm. Both spectrophotometers (A and B) produced comparably useful spectra, measured with the test samples in a conventional, 1-cm light-path quartz cuvette. We also measured some optical density spectra with another spectrophotometer that works with much smaller volumes (5 μL). This spectrophotometer (NanoDrop®1000, Thermo Scientific), which has an air-exposed measuring site, produced too noisy spectra for reliable size determination, however.

We programmed a Mathcad sheet (Mathcad version 14, Parametric Technology Corporation, Needham, Massachusetts, USA) including the complete set of equations given in “Theory” section. Before analyzing the measured turbidity spectra with the sheet, we confirmed that the spectra are in the linear concentration dependency range (i.e. $d\tau/dL = \text{constant}$), which is a prerequisite for applying Eq. 4.8 or Eq. 4.17 (see the “Theory” section).

4.3.5 Dynamic light scattering (photon correlation spectroscopy)

We used an ALV-NIBS/HPSS particle sizer (ALV-Laser Vertriebsgesellschaft mbH, Langen, Germany) for the dynamic light scattering measurements. The device is equipped with a HeNe laser ($\lambda = 632.8$ nm) and operates with a scattering angle of 173° . We measured each sample at 25°C three to six times and analyzed the results with the ALV-5000/E/EPP software (Ver. 3.0, regularized fit routine, scattering spherical shells) based on the CONTIN 2DP method ^[130, 131]. We took the refractive index and the dynamic viscosity of water at 25°C to be $n = 1.33162$ ($\lambda = 632.8$ nm; Eqs. 4.20-4.21) and $\eta = 0.89038$ cP. We calculated the dynamic viscosity of the aqueous carbonate buffer with the formula developed by Pereira et al. ^[132] to be 0.91711 cP. The effect of sodium cholate on suspension viscosity in the studied

concentration range was negligible (< 0.002 cP)^[133].

4.4 Results and discussion

4.4.1 Characteristics affecting turbidity of a nanosized particle suspension

In this section we explore theoretically effects of various particle and dispersion medium characteristics on turbidity and wavelength exponent spectra of a particle suspension, all within the framework of the RGDA. We first focus on general characteristics of any particle suspension, including particle mean size and size distribution, particle and dispersion medium refractive indices, and particle concentration within the homogeneous sphere as well as the hollow sphere models. We then deal with special characteristics of hollow spheres/spherical shells/lipid vesicles, such as shell/bilayer thickness and number of shells/bilayers in a particle (i.e. lamellarity).

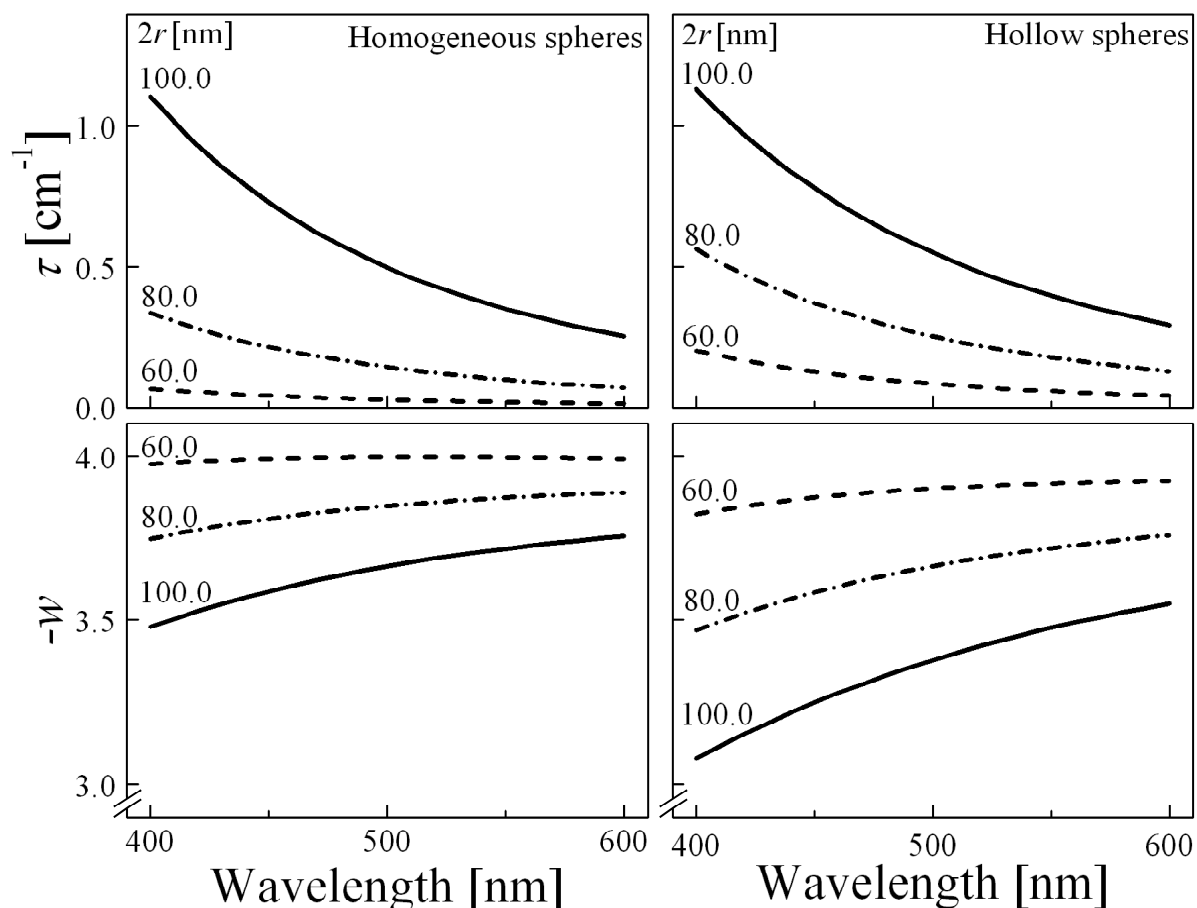


Figure 4.1 Effect of light scattering particle diameter ($2r = 60.0$ – 100.0 nm, monodisperse) on the particle suspension turbidity (upper panels) and wavelength exponent (lower panels) spectra. The curves were calculated for suspensions of either homogeneous spheres (left two panels, number concentration $N_p = 1.1 \times 10^{12}$ mL⁻¹) or hollow spheres/spherical shells/lipid vesicles (right two panels, number concentration $N_v = 3.5 \times 10^{13}$ mL⁻¹, shell thickness $d_{\text{shell}} = 3.6$ nm). The homogeneous spheres and the spherical shells/lipid bilayers were assumed to have the refractive index of dipalmitoylphosphatidylcholine (Eq. 4.22) and the dispersion medium to have the refractive index of water (Eqs. 4.20–4.21).

4.4.1.1 General characteristics of a nanosized particle suspension

Size: Raising particle size in a suspension of monodisperse (i.e. having the same size) particles with a fixed number concentration increases the suspension turbidity and decreases the wavelength exponent absolute value, i.e. $-w$, at all wavelengths. The effect is qualitatively similar for homogeneous and hollow spheres/vesicles (Fig. 4.1). Both turbidity and wavelength exponent spectra are sensitive to particle size changes; they are therefore both useful for particle size characterization. Shorter wavelengths offer a higher relative sensitivity.

Size distribution: No real suspension is truly monodisperse. To allow for particle size distribution we introduced the log-normal distribution function into the mathematical expressions used for various analyses. Our results thus give the geometric, rather than arithmetic, mean diameters and standard deviations. Simulations described in this section and the consequent findings are accordingly quantitatively valid only within limits of such distribution function applicability.

Broadening the size distribution (i.e. increasing the standard deviation, σ) in a suspension of particles with fixed mean diameter and number concentration increases the suspension turbidity and decreases the wavelength exponent absolute value at all wavelengths. Fig. 4.2 illustrates the effects for suspensions of homogeneous spheres, but we also got similar results for hollow spheres (data not shown). Broadening size distribution (Fig. 4.2) and increasing mean particle diameter (Fig. 4.1) influence turbidity spectra, in qualitative terms, similarly. The two main reasons are: *i*) light scattering by a particle is a power function of the light scattering particle radius; higher turbidity caused by extending such particles size distribution towards the distribution function high end thus overcompensates the turbidity decrease caused by extending the size distribution towards the distribution function low end; *ii*) the log-normal distribution is skewed.

Quantitative analysis of turbidity or wavelength exponent spectra can afford the mean size as well as the size distribution width (expressed as a standard deviation) of suspended particles despite the qualitative similarity of effects of these two parameters. For illustration, we simulated a set of turbidity spectra ($\lambda = 400\text{-}600$ nm, Fig, 4.3, upper panel) for suspensions containing particles with different geometric mean diameter and standard deviation but identical turbidity at $\lambda = 600$ nm. We also generated a similar set of wavelength exponent spectra with identical wavelength exponent at $\lambda = 600$ nm (Fig, 4.3, lower panel). The spectra confirm that changing the mean diameter and standard deviation produces quantitatively

dissimilar effects and yields characteristic $d\tau/d\lambda$ and $dw/d\lambda$ derivatives. These differences permit accurate calculation of the mean diameter and the corresponding standard deviation from the spectra. The analyzed spectrum broadening improves analytical accuracy.

Turbidity spectrum analysis neglecting scatterer size distribution (i.e. assuming monodispersity, $\sigma = 0$) provides a diameter value that is larger than the number-weighted geometric

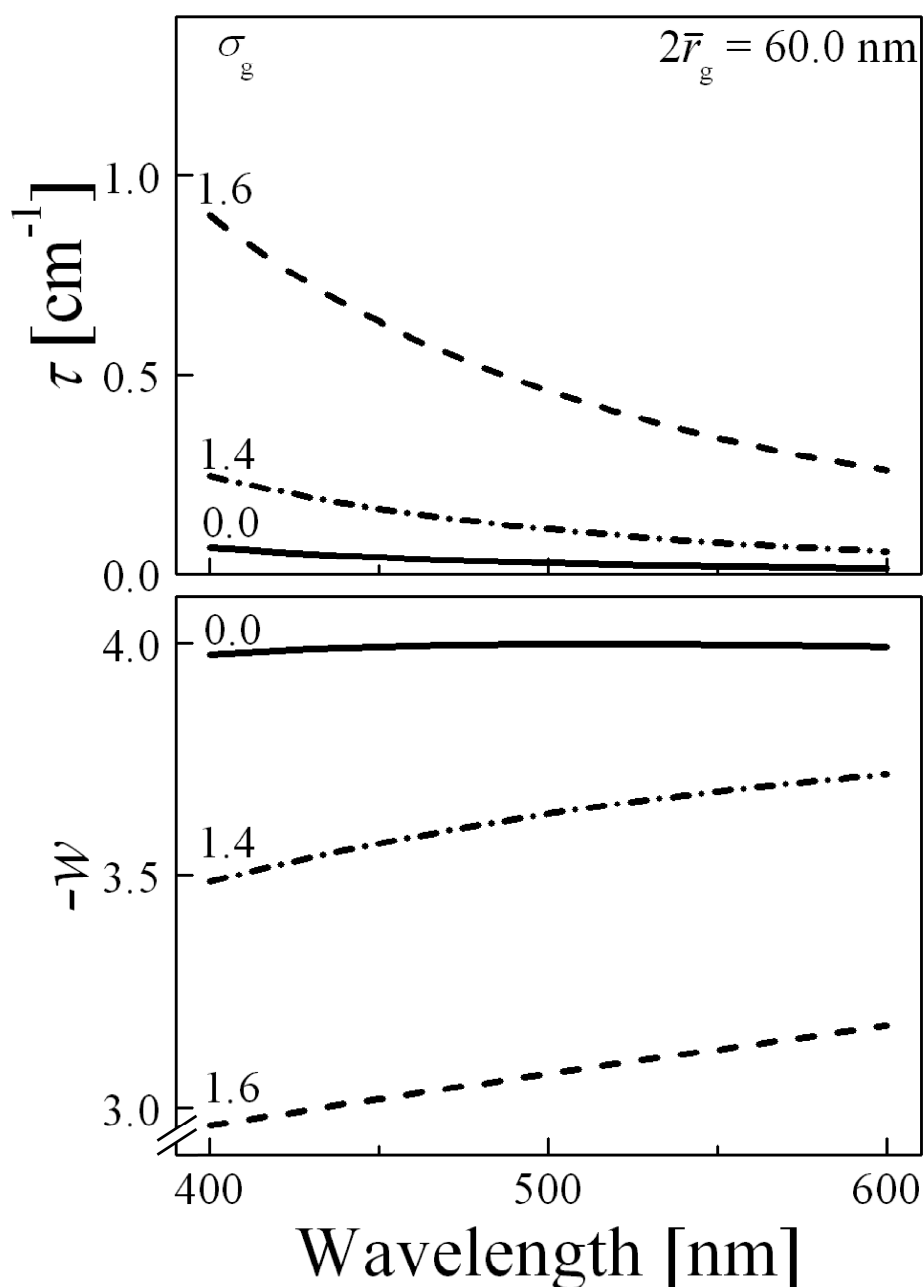


Figure 4.2 Effect of particle size distribution width (geometric mean diameter $2\bar{r}_g = 60.0 \text{ nm}$, standard deviation $\sigma_g = 0.0\text{--}1.6 \text{ nm}$ (equivalent to $\delta = 0.00\text{--}0.45$)) on suspension turbidity (upper panel) and wavelength exponent (lower panel) spectra. The curves were calculated for suspensions of homogeneous spheres with a number concentration $N_p = 1.1 \times 10^{12} \text{ mL}^{-1}$. The spheres were assumed to have the same refractive index as dipalmitoylphosphatidylcholine (Eq. 4.22) and the dispersion medium to have the refractive index of water (Eqs. 4.20–4.21).

mean diameter and smaller than the intensity-weighted geometric mean diameter. Wavelength exponent spectrum analysis neglecting scatterers size distribution yields a good approximation of the intensity-weighted geometric mean diameter, provided that the underlying size distribution is not too wide (Table 4.1).

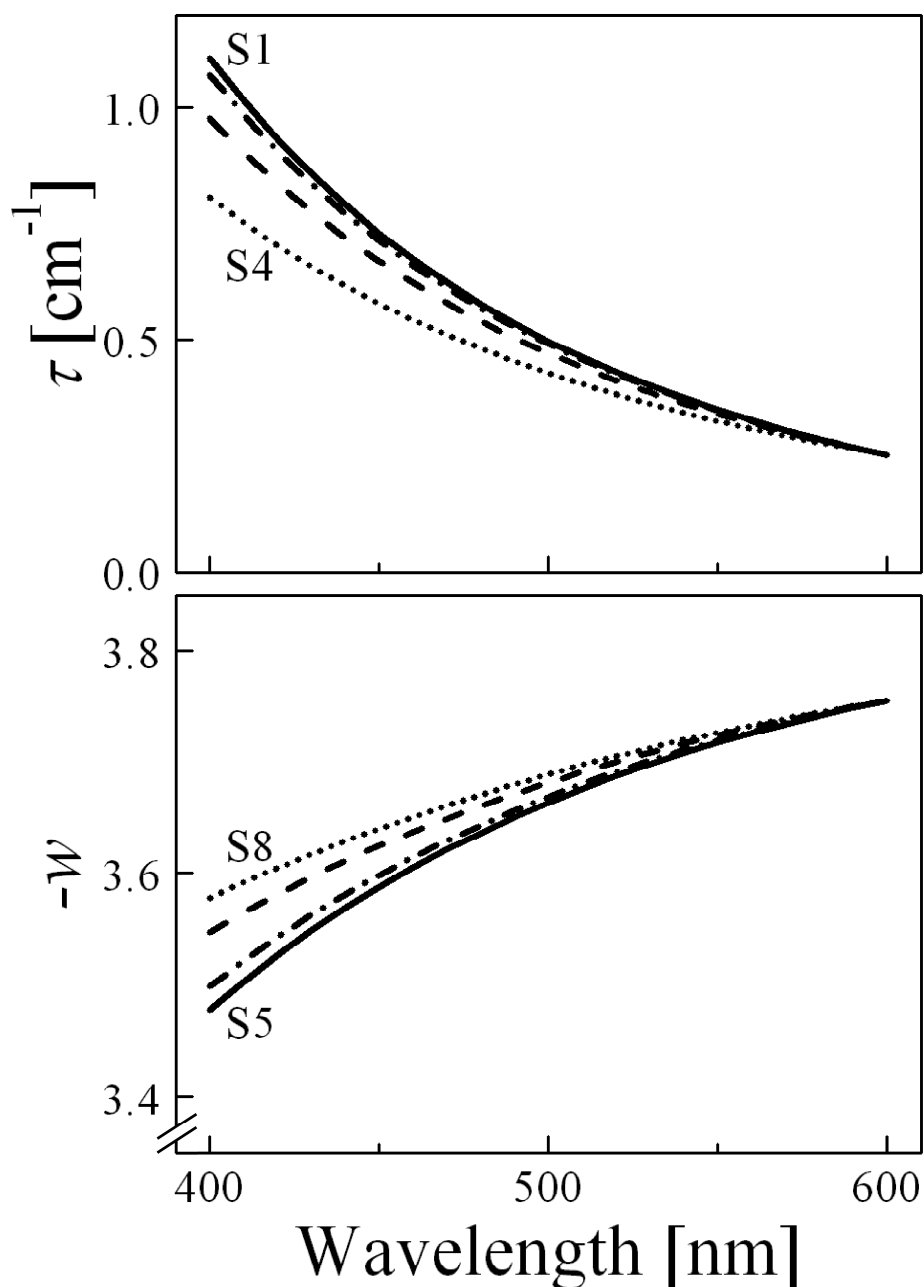


Figure 4.3 Turbidity (upper panel) and wavelength exponent (lower panel) spectra calculated for suspensions of homogeneous spheres with constant number concentration $N_p = 1.1 \times 10^{12} \text{ mL}^{-1}$ and variable geometric mean diameter and standard deviation. Detailed characteristics of the suspensions are given in Table 4.1. The suspensions have either identical turbidity (upper panel) or wavelength exponent (lower panel) at $\lambda = 600 \text{ nm}$. The figure illustrates how quantitative analysis of turbidity or wavelength exponent spectra can resolve the mean diameter as well as the standard deviation.

Table 4.1 Characteristics of the simulated suspensions used to generate the spectra shown in Fig. 4.3.

Line	Number-weighted ^a		Intensity-weighted ^{a,b}		Calculated (MD) ^c
	Mean diameter, $2\bar{r}_g$ [nm]	St. deviation, σ_g [nm]	Mean diameter, $2\bar{r}_g$ [nm]	St. deviation, σ_g [nm]	
Identical $\tau(\lambda = 600 \text{ nm})^e$					
S1	100.0	0.0 (0.00)	100.0	0.0 (0.00)	100.0
S2	94.1	1.2 (0.02)	106.2	1.2 (0.02)	99.6
S3	78.7	1.3 (0.09)	125.4	1.3 (0.08)	98.4
S4	41.7	1.8 (0.36)	210.8	1.6 (0.24)	95.9
Identical $w(\lambda = 600 \text{ nm})^f$					
S5	100.0	0.0 (0.00)	100.0	0.0 (0.00)	100.0
S6	86.5	1.2 (0.02)	97.8	1.2 (0.02)	99.2
S7	56.7	1.3 (0.09)	93.0	1.3 (0.08)	97.3
S8	14.9	1.8 (0.36)	97.8	1.6 (0.22)	96.2

^a All calculations rely on the log normal distribution function. The given values therefore denote the geometric, rather than arithmetic, mean diameters and standard deviations.

^b Calculated relying on turbidity at $\lambda = 500 \text{ nm}$.

^c Diameters calculated by analyzing the simulated turbidity (Fig. 4.3, upper panel) or wavelength exponent (Fig. 4.3, lower panel) spectra presuming monodispersity, i.e. not allowing for particle size distribution.

^d Values in parentheses denote the conventional polydispersity index, defined as $PI = \sigma^2 = (\ln \sigma_g)^2$.

^e Various suspensions of homogeneous spherical particles with the same turbidity at $\lambda = 600 \text{ nm}$; the spheres were assumed to have the same refractive index as dipalmitoylphosphatidylcholine (Eq. 4.22) and the dispersion medium to have the refractive index of water (Eqs. 4.20–4.21); number concentration $N_p = 1.1 \times 10^{12} \text{ mL}^{-1}$.

^f Various suspensions of homogeneous spherical particles with the same wavelength exponent at $\lambda = 600 \text{ nm}$; the spheres were assumed to have the same refractive index as dipalmitoylphosphatidylcholine (Eq. 4.22) and the dispersion medium to have the refractive index of water (Eqs. 4.20–4.21); number concentration $N_p = 1.1 \times 10^{12} \text{ mL}^{-1}$.

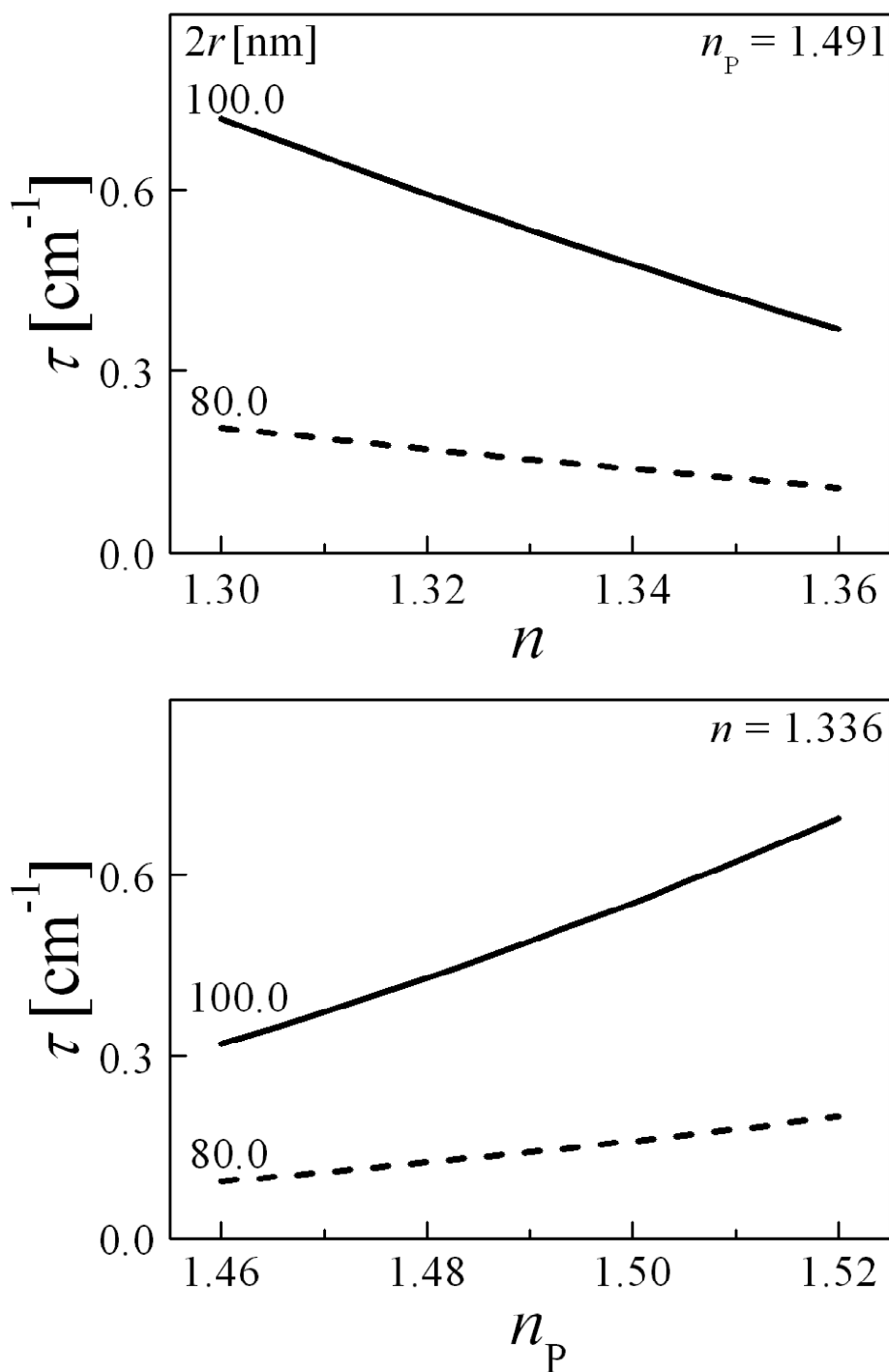


Figure 4.4 Influence of particle and dispersion medium refractive indices on suspension turbidity. The curves were calculated at $\lambda = 500$ nm for suspensions of monodisperse ($2r = 80$ nm or 100 nm) homogeneous spheres with a number concentration $N_p = 1.1 \times 10^{12}$ mL $^{-1}$. Results for hollow spheres/spherical shells/lipid vesicles are qualitatively similar.

Refractive index. Suspension turbidity depends on the scattering particle and the dispersion medium refractive indices (Fig. 4.4). Raising the particle-to-dispersion medium relative refractive index, m , generally increases suspension turbidity. Wavelength exponent does not depend on refractive indices values at any particular wavelength but rather on their

wavelength dependency (Eq. 4.15). The effect is usually negative. Tiny particles therefore have $\lim_{r \rightarrow 0} w < -4$. For an aqueous suspension of homogeneous spheres, assumed to have the same refractive index as dipalmitoylphosphatidylcholine (Eq. 4.22), in water (n calculated from Eqs. 4.20–4.21) one gets: $\lim_{r \rightarrow 0} w = -4.29$ at $\lambda = 400$ nm and $\lim_{r \rightarrow 0} w = -4.20$ at $\lambda = 500$ nm.

Concentration. Turbidity increases linearly with number concentration of particles in a suspension (Eq. 4.8). Linear concentration dependency of turbidity is thus a prerequisite for applying Eq. 4.8 for turbidity spectrum analysis. Non-linearity is diagnostic of interference, e.g. quenching or multiple-scattering. Wavelength exponent is, in contrast, concentration independent (Eqs. 4.9–4.10). Inaccurate information about particle concentration, density, and/or molecular weight (for lipid vesicles, see Eqs. 4.1–4.6) consequently affects the outcome of turbidity spectrum analysis but not of wavelength exponent spectrum analysis.

4.4.1.2 Special characteristics of hollow spheres/spherical shells/lipid vesicles

Shell/bilayer thickness. Hollow spheres scatter light more when their shell thickens. Turbidity of a suspension of monodisperse unilamellar vesicles with a fixed outer radius thus increases with bilayer thickness (Fig. 4.5, upper panel). The corresponding wavelength exponent is less affected by bilayer thickness. Within the 3–4 nm thickness range, which pertains to most common biological and synthetic lipids, the effect is close to nil (Fig. 4.5, lower panel). Inaccurate presumption about shell/bilayer thickness within such range thus produces significant error (up to 100%) if one derives hollow sphere/vesicle size from turbidity spectra. In contrast, similarly inaccurate presumption gives an error of less than 0.5 nm for hollow sphere/vesicle size calculated from corresponding wavelength exponent spectra (both error estimates were calculated for vesicles with diameter ≤ 120 nm studied in the wavelength range $\lambda = 400$ – 600 nm). Lacking trustworthy information about shell/bilayer thickness, one should therefore rely rather on wavelength exponent than on turbidity spectrum analysis for hollow sphere/vesicle size characterization.

Number of shells/lipid bilayers (lamellarity). Effect of increasing number of shells/bilayers on turbidity resembles that of increasing single shell/bilayer thickness. Vesicles with a higher number of bilayers (i.e. lamellarity, l) consequently produce more turbid suspensions at fixed lipid vesicle mass concentration (keeping the mass concentration constant and increasing vesicle lamellarity reduces the number concentration of vesicles; turbidity increase is thus greater if the number- rather than mass concentration is fixed), outer

radius, and bilayer thickness (Fig. 4.6, upper panel). Wavelength exponent spectra change with lamellarity as well, but less so than turbidity spectrum (Fig. 4.6, lower panel).

Distribution of (mixed) “lamellarity”. A suspension of ideally uniform lipid vesicles comprises merely vesicles with identical lamellarity. Such a suspension is practically unachievable, however. We therefore assessed the influence of uncertain, or diverse, lamellarity

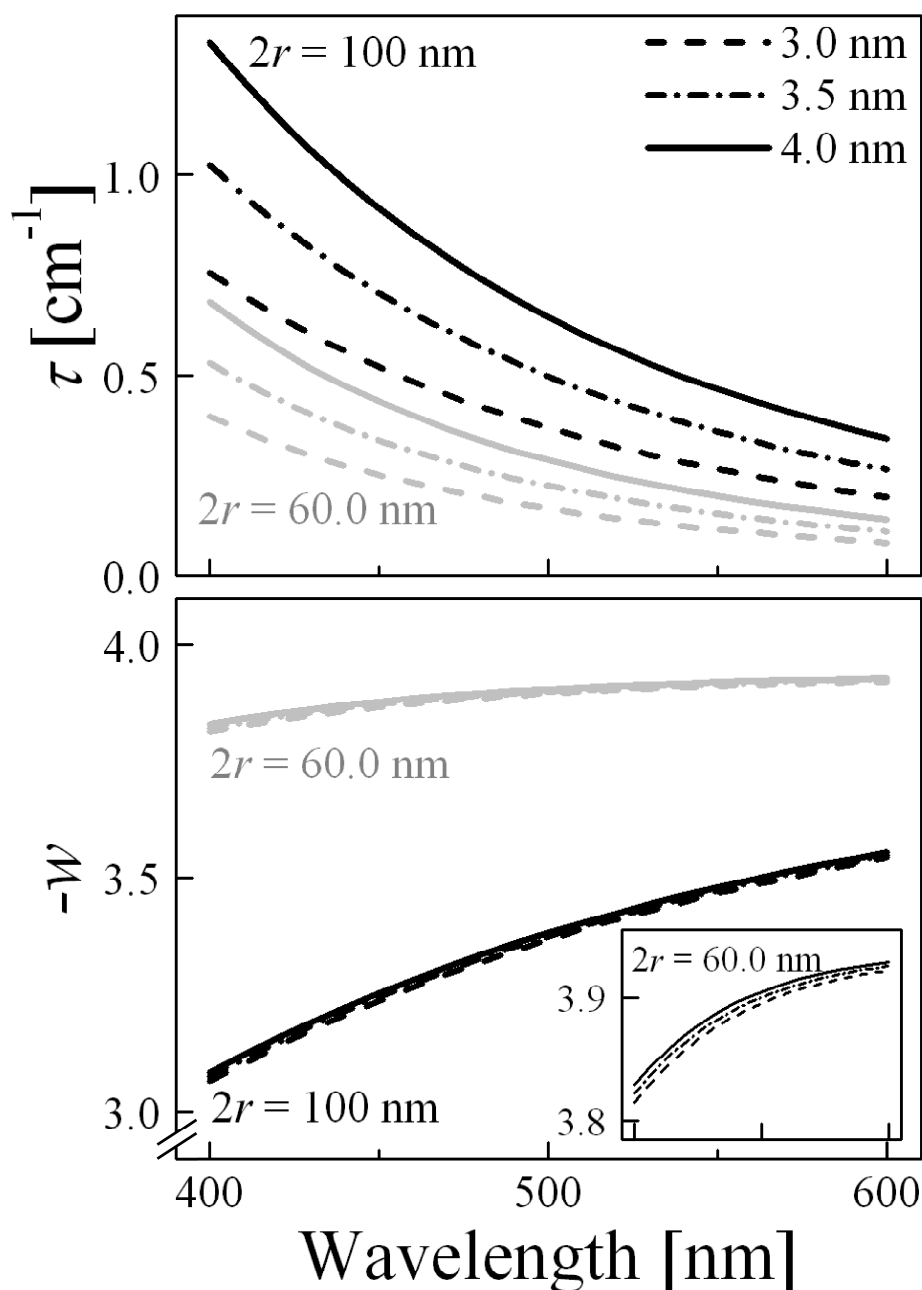


Figure 4.5 Effect of spherical shell/lipid bilayer thickness ($d_b = 3\text{--}4$ nm) on turbidity (upper panel) and wavelength exponent (lower panel) of a monodisperse unilamellar lipid vesicle suspension. The curves were calculated assuming constant lipid (dipalmitoylphosphatidylcholine) concentration of 5 mM ($\approx 0.37\%$ w/w) and shell/vesicle outer diameter $2r_v = 100$ nm (black curves) or 60 nm (grey curves). The lipid (dipalmitoylphosphatidylcholine) refractive index was calculated from Eq. 4.22 and the dispersion medium (water) refractive index from Eqs. 4.20–4.21. Inset to the lower panel: blow-up of the curves pertaining to the 60 nm vesicles.

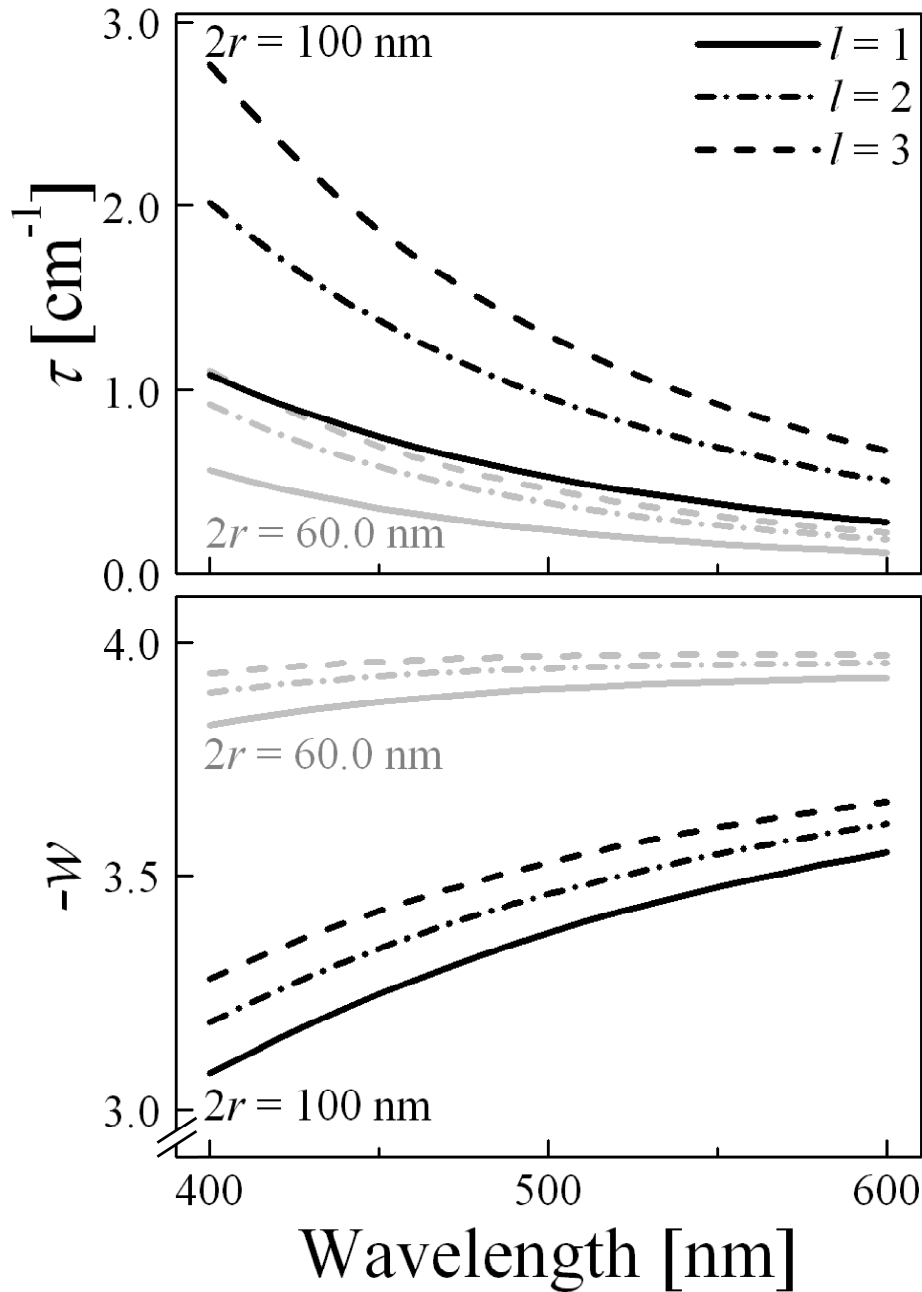


Figure 4.6 Effect of lamellarity ($l = 1, 2,$ or 3) on turbidity (upper panel) and wavelength exponent (lower panel) of a suspension of monodisperse lipid vesicles. The curves were calculated assuming a constant lipid (dipalmitoylphosphatidylcholine) concentration of 5 mM (≈ 0.37 % w/w), bilayer thickness $d_b = 3.6$ nm, inter-bilayer/inter-shell water layer thickness $d_w = 3.0$ nm, outer diameter $2r_v = 100$ nm (black curves) or $2r_v = 60$ nm (grey curves), lipid (dipalmitoylphosphatidylcholine) refractive index calculated from Eq. 4.22, and dispersion medium (water) refractive index calculated from Eqs. 4.20–4.21.

on the size calculated via wavelength exponent spectrum analysis. We did this by simulating a set of turbidity spectra ($\lambda = 400$ – 600 nm) for suspensions containing unilamellar-bilamellar or unilamellar-trilamellar vesicle mixtures. We then used the simulated spectra to back-calculate the apparent vesicle diameter via wavelength exponent analysis presuming that all vesicles are unilamellar.

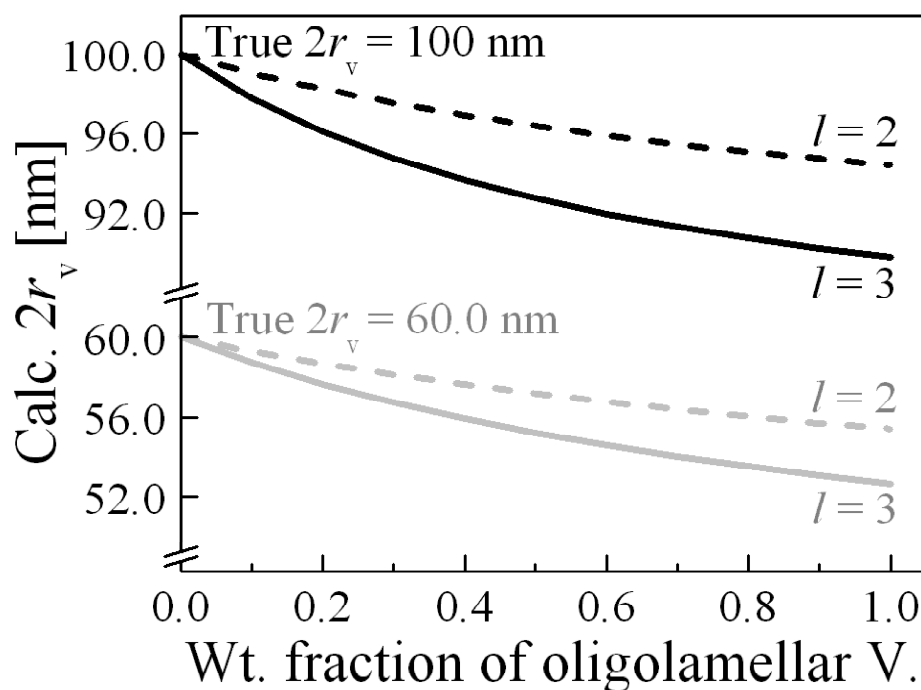


Figure 4.7 Vesicle diameter calculated from wavelength exponent spectra ($\lambda = 400\text{--}600$ nm) presuming unilamellarity as a function of the weight fraction of oligolamellar vesicles. Model parameter values are the same as for Fig. 4.6.

Fig. 4.7 illustrates the resulting analytical error as a function of the weight-fraction of oligolamellar vesicles. The analytical approach underestimates the average vesicle size when oligolamellar vesicle existence is neglected. The error is small: for a suspension containing 20 weight-% bilamellar or trilamellar vesicles the resulting mistake is below 4.0% for vesicles with a real diameter $2r_v = 60$ nm or 100 nm. One can therefore reliably derive size of lipid vesicles in suspension from wavelength exponent spectrum presuming unilamellarity even if the studied suspension contains a moderate fraction of oligolamellar vesicles. In turn, one can inspect oligolamellarity by, first, calculating the average vesicle size from the wavelength exponent spectrum and, second, using this result to derive lamellarity from the corresponding turbidity spectrum (turbidity spectra are, in contrast to wavelength exponent spectra, very sensitive to lamellarity).

4.4.2 Characterization of real lipid vesicle suspensions

We investigated the practical feasibility of the analytical approach described here. Hollow spheres are more difficult to characterize with the visible light scattering than homogeneous spheres due to their greater complexity and lower optical contrast. We therefore decided to test the proposed method with fluid-chain lipid vesicles (liposomes) rather than

with homogeneous spheres. For the purpose, we prepared differently sized soybean phosphatidylcholine vesicles by extrusion, which typically yields unilamellar vesicles with a narrow size distribution [56, 134, 208]. For each of the resulting suspensions we recorded the turbidity spectrum and derived the vesicle size via the corresponding wavelength exponent spectrum analysis. We also characterized each suspension with dynamic light scattering.

More specifically, we first derived a wavelength exponent spectrum from each turbidity spectrum by taking the derivative $d \log \tau / d \log \lambda$ (Eq. 4.14). We then analyzed the derived wavelength exponent spectrum, $w(\lambda)$, within the framework of the Rayleigh-Gans-Debye approximation, as is described in the “Theory” section. We principally employed the hollow sphere/spherical shell model, which best describes lipid bilayer vesicles [168, 182, 183, 197]. Given that some researchers [191, 209] had previously treated vesicles as homogeneous spheres with an averaged refractive index, we tested such an approach as well.

We initially presumed that the preparations are monodisperse, i.e. we did not allow for any size distribution in the analysis. The excellent fitting results confirmed our quasi-monodispersity assumption. The results derived relying on the hollow sphere/spherical shell model agreed with the dynamic light scattering results (Table 4.2). Conversely, treating the studied vesicles as homogeneous spheres with an averaged refractive index gave approximately 25% too large diameter (Table 4.2), proving inadequacy of such an assumption.

Wavelength exponent spectra are little sensitive to vesicle lamellarity and bilayer thickness. They are moreover independent of vesicle concentration. Analysis of a wavelength exponent spectrum thus provides a reliable size estimate even when only inaccurate, but reasonable, values are available for these parameters. Conversely, turbidity spectra are very responsive to all the three listed parameters. One can thus employ sizes calculated from wavelength exponent spectra to derive information about vesicle lamellarity, bilayer thickness, and/or the average area per (lipid) molecule forming bilayers/shells through turbidity spectrum analysis. Our wavelength exponent spectrum analysis assumed vesicle unilamellarity, bilayer thickness $d_b = 3.6 \text{ nm}$ [184], and an average area per lipid molecule of $A_L = 0.65 \text{ nm}^2$ (which we used to calculate the vesicle number concentration according to Eqs. 4.9 and 4.16). The turbidity spectra analyses based on these values gave larger diameters than the corresponding wavelength exponent spectra analyses; this suggests that at least one of the parameter values used was too low. The discrepancy was largest for the V80 suspension and smallest for the V30 suspension (possibly due to a higher fraction of oligolamellar vesicles in the former suspension).

Petrache, et al. ^[193] reported for egg-yolk phosphatidylcholine $V_L = 1.2606 \text{ nm}^3$ and estimated molecular area to be $A_L = 0.694 \text{ nm}^2$. These values insertion into the Luzzati formula gave $d_b = 3.63 \text{ nm}$; the same authors also calculated $d_b = 4.52 \text{ nm}$ with a different approach. We took the quoted V_L value as a surrogate for the otherwise still unknown volume of a soybean phosphatidylcholine molecule and set $3.63 \text{ nm} \leq d_b \leq 4.52 \text{ nm}$. Assuming, sensibly, that the V30 preparation contained merely monodisperse unilamellar vesicles, we brought results of turbidity spectrum and wavelength exponent spectrum analyses into quantitative agreement by setting $d_b = 4.1 \text{ nm}$ and $A_L = 0.62 \text{ nm}^2$. Considering existenc of oligolamellar vesicles, if real, would decrease the calculated bilayer thickness value (Fig. 4.6). We thereafter ventured to assess, using the derived d_b value, vesicle lamellarity in the preparations V50 and V80. We surmised the suspensions V50 and V80 to contain unilamellar and bilamellar, monodisperse vesicles and repeated the analysis. This implied 11% bilamellarity in the suspension V50S01 and 24% bilamellarity in the suspension V80S01. Whilst one should take these estimates with a grain of salt, they are broadly compatible with the published information about extruded vesicles lamellarity ^[56, 191], leaving no need for alternative explanations (e.g. by invoking vesicle non-sphericity).

Table 4.2 Size characterization of the tested extruded lipid vesicles

Preparation	Geometric mean diameter, $2\bar{r}_g$ [nm] ^a		
	Dynamic light scattering	Turbidity spectroscopy ^b	
		Hollow sphere	Homogeneous sphere
V80S01	106.2 ± 1.6	101.3 ± 0.0 ^{c,e}	128.7 ± 0.1 ^{c,e}
V80S02	111.9 ± 3.0	108.4 ± 0.4 ^{d,f}	138.7 ± 0.6 ^{d,f}
V50S01	86.8 ± 0.8	83.1 ± 0.3 ^{c,e}	103.7 ± 0.4 ^{c,e}
V50S02	89.0 ± 0.6	86.3 ± 0.4 ^{c,g}	108.1 ± 0.5 ^{c,g}
V50S03	92.3 ± 0.8	92.0 ± 0.4 ^{d,h}	115.9 ± 0.6 ^{d,h}
V30S01	72.2 ± 0.8	71.1 ± 0.1 ^{c,j}	87.6 ± 0.2 ^{c,j}

^a Results are presented as mean ± SD of at least 3 replicate measurements.

^b Diameters were derived from wavelength exponent spectra, presuming vesicle monodispersity; the calculations relied on bilayer thickness $d_b = 3.6 \text{ nm}$ and on the refractive indices defined by Eqs. 4.20–4.21 (for water) and 4.22 (for the bilayer forming phospholipid).

^c Spectrophotometer A, the analyzed spectrum range: 400–600 nm.

^d Spectrophotometer B, the analyzed spectrum range: 400–600 nm.

^e Lipid concentration = 4 mM.

^f Lipid concentration = 3–6 mM.

^g Lipid concentration = 7–10 mM.

^h Lipid concentration = 4–10 mM.

^j Lipid concentration = 6 mM.

To assess size distribution effects we mixed the suspensions V80 and V50 at different ratios. We characterized the blends via wavelength exponent analyses, allowing for size distribution, and with dynamic light scattering. Table 4.3 gives the results that confirm similar sensitivity of both methods to size distribution changes. The results also support our earlier notion that analyzing wavelength exponent spectra presuming monodispersity well approximates the intensity-weighted mean diameter.

4.4.3 Monitoring small size changes (effect of cholate on size of lipid vesicles)

We finally checked suitability of turbidity spectroscopy for monitoring small particle, vesicle, or drug carrier size changes. To this end, we added sodium cholate to the suspensions V80 and V50 to a final surfactant concentration of 0.0–1.2 mmol/kg. We then characterized the resulting mixtures with turbidity spectroscopy, via wavelength exponent analysis, and with dynamic light scattering. The results are shown in Fig. 4.8 and corroborate similar sensitivity of both methods to even quite small vesicle size changes.

4.4.4 Experimental recommendations and limitations

Adjust sample concentration so that the measured optical density over the analyzed spectrum range preferably lies between 0.2 and 1.2. Filter all dilution media to eliminate contaminants, such as dust particles, that scatter light more than smaller investigated particles.

Choose the analyzed wavelength range carefully, including the RGDA validity check (see “Theory” section and Appendix 4.1) at the low end of the utilized range (for lipid vesicles with an average diameter up to 130 nm suspended in aqueous medium setting the low wavelength limit at 400 nm is a good choice). The upper wavelength limit selection is normally governed by the signal-to-noise ratio, which is worsened by decrease of suspension turbidity at high wavelengths. Taking turbidity spectrum derivative (i.e. deriving the wavelength exponent spectrum) amplifies experimental noise. One should eliminate the noisy readings at the high spectrum end or smooth the experimental spectrum before its derivation.

Exclude spectral regions in which the tested preparation (the particles material and/or the dispersion medium) significantly absorbs light. Alternatively, eliminate the contribution from light absorption by analyzing the difference of the spectra measured with a turbid and absorbing suspension (e.g. in water) and with a corresponding clear but still light absorbing solution (e.g. in a water/suitable solvent mixture), i.e. subtract the absorption part of a spectrum from total extinction spectrum (see ^[210] for the reverse procedure) to gain a pure turbidity spectrum.

Table 4.3 Sensitivity of different analytical methods to changes in vesicle size distribution.

Sample composition [w/w]	Dynamic light scattering ^a		Turbidity spectroscopy ^{a, b}	
	Mean diameter, $2\bar{r}_g$ [nm]	Standard deviation, σ_g^c [nm]	Mean diameter, $2\bar{r}_g$ [nm]	Standard deviation, σ_g^c [nm]
4 : 0	111.4 ± 1.3	1.4 ± 0.1 (0.11 ± 0.04)	123.2 ± 0.3	1.6 ± 0.0 (0.20 ± 0.01)
3 : 1	107.0 ± 0.9	1.5 ± 0.1 (0.15 ± 0.03)	120.7 ± 1.8	1.7 ± 0.1 (0.29 ± 0.04)
2 : 2	103.0 ± 1.5	1.5 ± 0.1 (0.16 ± 0.08)	109.6 ± 0.0	1.7 ± 0.0 (0.29 ± 0.00)
1 : 3	97.0 ± 3.1	1.6 ± 0.4 (0.25 ± 0.24)	101.7 ± 0.1	1.8 ± 0.0 (0.36 ± 0.00)
0 : 4	88.0 ± 1.1	1.4 ± 0.1 (0.12 ± 0.05)	79.6	1.4 (0.11)

^a All calculations relied on the log normal distribution function. The given values therefore denote intensity-weighted geometric, rather than arithmetic, mean diameters and standard deviations. The results are presented as mean ± SD of replicate measurements.

^b Diameters were derived from wavelength exponent spectra; the calculations relied on the hollow sphere/spherical shell model, bilayer thickness $d_b = 3.6$ nm, and refractive indices defined by Eqs. 4.20–4.21 (for water) and 4.22 (for the lipid). Measurements were conducted using spectrophotometer A; Spectrum range: 400–600 nm.

^c Values between parentheses denote the conventional polydispersity index, which is defined as $PI = \delta^2 = (\ln \sigma_g)^2$.

^d Diameters calculated presuming monodispersity, i.e. not allowing for size distribution.

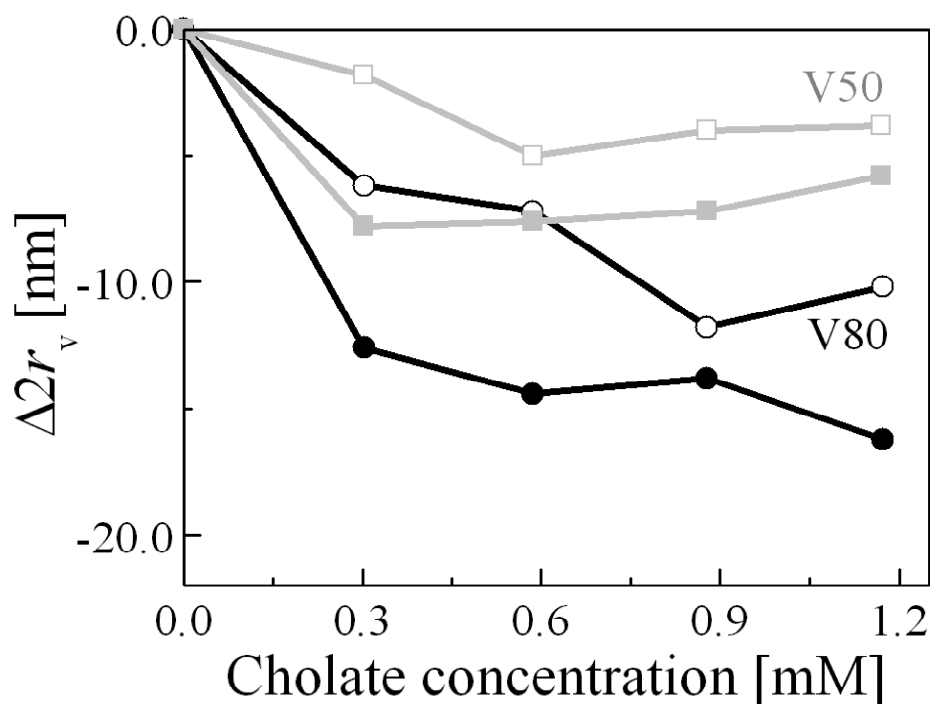


Figure 4.8 Effect of sodium cholate concentration on size of extruded lipid vesicles (preparations V80 (black circles) and V50 (grey squares)), as measured with turbidity spectroscopy relying on wavelength exponent analysis (filled symbols) or with dynamic light scattering (open symbols). Analysis of wavelength exponent spectra presumed monodispersity and relied on the hollow sphere/spherical shell model, bilayer thickness $d_b = 3.6$ nm, and refractive indices defined by Eqs. 4.20-4.21 (for water) and 4.22 (for the lipid).

Wavelength exponent spectrum analysis is typically better choice for size-determination than turbidity spectrum analysis. The main reasons are: *i*) concentration independence; *ii*) good approximation to the intensity-weighted mean diameter even in the approximation presuming simplest monodispersity; *iii*) low sensitivity to shell/bilayer thickness uncertainty; *iv*) low sensitivity to number of shells/oligolamellarity. In turn, these advantages turns into disadvantages when one wishes to explore characteristics to which wavelength exponent spectrum is only moderately or not at all sensitive. Such characteristics consequently must be investigated with turbidity spectrum analysis.

4.5 Conclusions

Turbidity spectrum of submicroscopic, nanosized drug carriers in suspension contains enough information for accurate size characterization. Analysis of the wavelength exponent spectrum suffices the purpose. Other characteristics pertaining to spherical shells/vesicles, such as shell thickness and number of shells/lamellarity, can be moreover derived from turbidity spectra. In this paper we pave the way for such applications by theoretically investigating sensitivity of turbidity spectra to various particle, vesicle and suspending

medium characteristics within the framework of the RGDA. We prove the analytical approach applicability by successfully employing the proposed method to extruded lipid vesicles size and size distribution determination. The quality and kind of information derived from the measured turbidity spectra of such vesicles at least matches the outcome of the corresponding dynamic light scattering measurements. The ability of either of the two techniques to monitor small size and/or size distribution changes is also similar, but the former method offers the advantage of speed and insensitivity to dispersion medium viscosity. We vindicated turbidimetric method ruggedness by recording the turbidity spectra with two different spectrophotometers, which produced practically identical analytical outcome.

Our results corroborate usefulness of any good spectrophotometer for reliable nanosized drug carrier characterization. This offers a valuable new option to all researchers and scientists in pharmaceutical industry and academia — and not just to those working in specialized laboratories with dedicated equipment. Sameness of turbidity spectra may confirm directly such carrier size-stability over time. Additional information about carrier size distribution or, with some restrictions, morphology (shell thickness and lamellarity for vesicles) is deducible by quantitative turbidity spectrum analysis. The unprecedented speed of the advocated method for drug carrier size characterization makes our approach suitable for assessing moderately fast kinetics. The opportunity to use a spectrophotometer equipped with a flow-through cell for continuous monitoring of drug carrier size makes the described method attractive for in-process control.

In short, the new drug carrier characterization method described in this work qualifies for routine applications in pharmaceutical research and quality control, where cost, experimental simplicity, and/or speed are of essence.

Appendix 4.A: Range of validity of the Rayleigh-Gans-Debye approximation

Kerker and colleagues ^[211] tested the range of validity of the Rayleigh-Gans-Debye approximation for homogeneous spheres by comparing the outcome of the exact Mie calculations and of the approximate calculation. As we are concerned with turbidity, we present in Fig. 4.9 the results for the scattering coefficient, Q_{sca} , defined as the total radiation scattered by a particle relative to the incident radiation intensity intercepted by the particle, i.e. $Q_{\text{sca}} = \tau/N_p\pi r^2$.

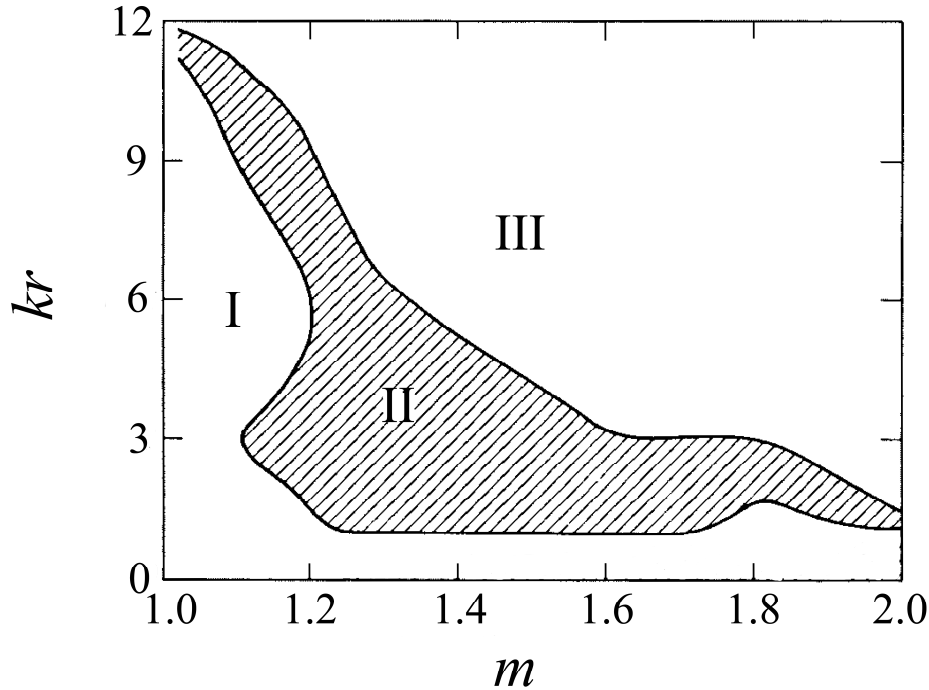


Figure 4.9 The error contour chart for the scattering coefficient, Q_{sca} (modified from ^[197, 211]). In region I, the accuracy of the Rayleigh-Gans-Debye approximation (RGDA) is better than 10%. In region II the RGDA accuracy is between 10% and 100% whereas in region III the error resulting from using the RGDA exceeds 100%, except in small islands. $k = 2\pi n/\lambda$ is the propagation constant in the dispersion medium with refractive index n in which scatterers with average diameter $2r$ and refractive index n_s are dispersed. Relative refractive index is described as $m = n_s/n$.

It is noteworthy that the area just above the abscissa with $m > 1.25$ is part of region II in the originally published chart ^[211]. The failure to obtain 10% agreement in this area is not due to limitation of the RGDA but rather due to the numerical approximation made by the authors about the refractive index, $\lim_{m \rightarrow 1} (m^2 - 1)/(m^2 + 2) = 2(m - 1)/3$. The error due to this approximation is 10% at $m = 1.25$. We avoided making such an approximation in our calculations described in the “Theory” section, and consequently included the area just above the abscissa with $m > 1.25$ into region I.

For a suspension of homogeneous spheres with $m = 1.10$ the 10% contour line is located at $kr = 9.2$. For a suspension of homogeneous spheres in water with $m = 1.10$, the RGDA analysis of turbidity spectra is consequently correct to within 10% when $r \leq \lambda$.

Appendix 4.B: The refractive index of water

The refractive index of water at 25 °C under atmospheric pressure is described as a function of wavelength in the visible wavelength range with the formula

$$n_w(\lambda) = \left(\frac{2u_w(\lambda) + 1}{1 - u_w(\lambda)} \right)^{0.5}, \quad (4.20)$$

where

$$u_w(\lambda) = b_0 + b_1 \lambda^{*2} + \frac{b_2}{\lambda^{*2}} + \frac{b_3}{\lambda^{*2} - \lambda_{UV}^{*2}} + \frac{b_4}{\lambda^{*2} - \lambda_{IR}^{*2}}. \quad (4.21)$$

$b_0 = 0.232602194$, $b_1 = + 0.294685133 \times 10^{-3}$, $b_2 = + 0.163176785 \times 10^{-2}$, $b_3 = + 0.241520886 \times 10^{-2}$, $b_4 = + 0.897025499$, $\lambda_{UV}^* = 0.2292020$, $\lambda_{IR}^* = 5.432937$, and $\lambda^* = \lambda/589$ nm. Eqs. 4.20–4.21 provide absolute accuracy of $\pm 1 \times 10^{-5}$.

We derived Eqs. 4.20–4.21 by simplifying the more general expression published by Schiebener and colleagues [212], which covers wide ranges of wavelengths, temperatures, densities, and pressures. We reached the goal by taking water density at 25 °C and atmospheric pressure to be $\rho = 997.0480$ kg m⁻³ [213].

Appendix 4.C: The refractive index of lipids

Khlebtsov and colleagues [190] proposed the following parametric description of dipalmitoylphosphatidylcholine (DPPC) refractive index as a function of light wavelength at 20 °C, based on data measured by Chong and Colbow with visible light above 400 nm [168]:

$$n_L(\lambda) = 1.4713 + 1.31 \text{ nm } \lambda^{-1} + 4309 \text{ nm}^2 \lambda^{-2}. \quad (4.22)$$

The result of Eq. 4.22 at $\lambda = 632.8$ nm, $n_L = 1.484$, compares favorably with the experimental values reported for DPPC at $T = 25^\circ\text{C}$ by Erbe and Sigl [214], $n_L = 1.478$. The result of Eq. 4.22 at $\lambda = 589$ nm, $n_L = 1.486$, likewise resembles the value extrapolated for DPPC to $T = 25^\circ\text{C}$ from the data published by Yi & McDonald [215], $n_L = 1.475$.

At the specified temperature DPPC forms one particular type of the ordered-gel, L_B-phase. Eq. 4.22 thus does not strictly apply to any other temperature or lipid. The former restriction is especially important; temperature not only gradually decreases n_L but can also trigger more influential lipid phase transitions. Chain fluidization, for example, lowers lipid refractive index; the reported difference for DPPC is approximately -0.008 units [215, 216].

Polar lipid headgroups contribute relatively little to the refractive index difference between lipid bilayers and water. The influence of lipid chain-length and unsaturation is bigger. Both these parameters increase lipid refractive index and thus can “compete” with the temperature- and fluidization-induced n_L changes.

In all experiments reported herein we were using soybean phosphatidylcholine (SPC). This lipid has roughly two more methylene groups per chain than DPPC and contains mainly di-unsaturated chains. SPC melts below the water-freezing point and the lipid is consequently in the fluid lamellar phase, L_α , at $T = 25^\circ\text{C}$. To the best of our knowledge, results of the kind reported for DPPC by Chong and Colbow ^[168] are unavailable for soybean phosphatidylcholine till date. We only found some information on the refractive index of soybean oil wavelength dependency ^[217]. Fortunately, soybean oil has arguably similar chain composition as soybean phosphatidylcholine. We thus used the parametrization published by van Staveren and colleagues for such oil to check Eq. 4.22 applicability to SPC, and thus to our illustrative experimental system. Between 500 nm and 800 nm the calculated difference between the two parametric equations amounts to -0.01203 ± 0.00084 . The two underlying expressions have therefore quite similar slope $dn_L/d\lambda$ in the compared wavelength region. Van Staveren expression may not be applied below 500 nm (where it predicts $dn_L/d\lambda$ to change sign) but is essentially equivalent to Eq. 4.22 at longer wavelengths. We therefore applied Eq. 4.22 herein to cover the entire analyzed wavelength range: $400 \text{ nm} \leq \lambda \leq 600 \text{ nm}$. Shifting results of Eq. 4.22 downward (by subtracting the above mentioned difference of 0.01203 from the constant in Eq. 4.22, i.e. replacing the term 1.4713 in Eq. 4.22 with 1.4593, whilst keeping all the other parameters unchanged) would merely affect turbidity spectrum analysis and leave the results of wavelength exponent spectrum analysis practically unchanged. As this work has a focus on the latter option, we refrained from making such a correction herein.

Any cautious user of the analytical method advocated in this work should always check applicability of Eq. 4.22 to his particular experimental system. More likely than not, the expression will need to be adjusted and/or generalized. This will require knowledge of at least some reliable n_L vs. λ data-pairs. If such information is missing, the appropriate refractive index dependency should be measured (e.g. with an Abbè refractometer). Alternatively, the n_L vs. λ dependency could be determined by, first, reversing the experimental sequence used in this work with the aim of generating a calibration data set for further applications. For the purpose, at least three suspensions of differently large vesicles should be prepared from the same batch of lipid and then assessed with wavelength exponent analysis and with dynamic light scattering. The results should be compared and the parameters needed for the former kind of analysis iteratively adjusted until the two size characterization methods give the same result.

5 Summary

Use of colloidal carriers in drug delivery continues to grow for decades. This created a need in the pharmaceutical field for better understanding of the physical and physicochemical properties of such, often complex, colloidal systems. This thesis aims at improving the understanding and at developing simple techniques helpful in colloidal drug carrier development and characterization.

In Chapter 2 we propose and explain a new analytical approach for analyzing potentiometric data measured with lipid vesicle suspensions. The proposed model for the first time properly considers the Coulombic electrostatic interaction in addition to the hydrophobic interactions underlying drug-carrier association. The approach was tested by studying association of four illustrative ionizable drugs, namely the anionic diclofenac and ketoprofen and the cationic bupivacaine and terbinafine, into neutral, phosphatidylcholine, and/or negatively charged, mixed phosphatidylcholine-phosphatidylglycerol, bilayer membranes.

Compared with the conventional approach, the new analytical approach better explains potentiometric data measured with complex systems. It also delivers more accurate and reliable lipid membrane-water partition coefficient of ionizable drugs. Unlike the previously used model, the new analytical method is advantageously insensitive to the experimental conditions that influence the Coulombic electrostatic interactions, such as lipid drug ratio and ionic strength. The new analytical method also permits studying drugs with high P^I (ionized form partition coefficient), such as terbinafine, which cannot be analysed satisfactory with the conventional approach.

Chapter 3 revisits vesicle-to-micelle transformation in phosphatidylcholine–cholate mixtures, paying special attention to the lipid bilayer curvature effects. For the purpose we studied the initial vesicle size effects on phosphatidylcholine vesicle transformation into cholate dominated mixed micelles, relying on static and dynamic light scattering measurements. Unlike most previous studies in the field, we ensured sodium cholate complete ionization by working at $\text{pH} = 10.25$. We quantitatively analyzed the results with several

theoretical models.

The emerging picture of vesicle-to-micelle transformation is richer but also more complex than previously known. In our view, vesicle-to-micelle transformation size-wise predominantly involves two largely parallel phenomena. The first is associated with an apparent, gradual mixed amphipat aggregate size decrease; it involves progressive bilayer destabilisation, bilayer fragmentation and thread micelle formation, followed by micelle size diminution. The second phenomenon is an apparent aggregate size increase, which involves mainly bilayer fusion, vesicle reformation and/or formation of bilayer-attached threadlike protrusions.

Quantitative data analysis revealed several interesting features. At low concentration cholate induces bilayer fluctuations. These fluctuations are more pronounced for the originally larger vesicles mainly owing to the broader fluctuation spectrum and the relatively smaller flip-flop-hampering surface curvature effects. For the same reasons, the originally larger vesicles can accommodate higher amounts of cholate and require more cholate for complete vesicle solubilisation.

The experimental findings reported in Chapter 3 raise some caveats: *i*) the very popular “bilayer-saturating concentration” is an ill-defined “descriptor” with assay-, preparation history-, and size-dependent value, at least when it is measured optically; *ii*) results obtained with only partially ionized surfactant are questionable due to molecular charge sensitivity to interfacial effects, and vice versa; *iii*) the “bilayer solubilising concentration”, which is the only descriptor that can be reliably derived from an optical measurement, depends on the starting aggregate size and can be burdened with slow transition kinetics; *iv*) the presumption of constant and laterally uniform aggregate composition is not tenable.

In Chapter 4 we investigate the feasibility of applying UV/Vis spectrometry for characterizing submicroscopic drug carriers, such as lipid vesicles. We first investigate theoretically, within the framework of the Rayleigh-Gans-Debye approximation (RGDA), the parameters that affect turbidity spectrum, $\tau(\lambda)$, of a submicroscopic light scatterer suspension. We then apply the RGDA to analyze turbidity spectra ($\lambda = 400\text{--}600$ nm) of various suspensions containing extruded lipid vesicles with an average diameter in the range ~ 70 nm $\leq 2r \leq 110$ nm. We also monitor cholate-induced vesicle size changes, always using dynamic light scattering measurements as control.

Our results suggest that the measured turbidity spectra contain sufficient information for accurate, fast, and viscosity independent characterization of submicroscopic particles. The power-law describing turbidity of such particle suspension, $\tau(\lambda) \propto \lambda^{w(\lambda)}$, or more precisely the exponent spectrum, $w(\lambda)$, analysis suits well the purpose. Such analysis yielded similar average diameters for the tested lipid vesicles ($2r = 108.4 \pm 0.4$ nm; 92.0 ± 0.4 nm; 71.1 ± 0.1 nm) as the dynamic light scattering ($2r = 111.9 \pm 3.0$ nm; 92.3 ± 0.8 nm; 72.3 ± 0.8 nm). The two methods were comparably suitable for monitoring cholate-induced, small (few-nanometer) vesicle size changes and to reveal size distribution changes.

The advanced analytical approaches developed and investigated in this thesis lend themselves to applications in the pharmaceutical research, mainly in colloidal carrier product characterization and quality control. They highlight some important properties of such complex formulations and help explain their basis. Further progress achievable with application of the proposed new analytical procedures opens the door for further advancements as well. The improved analytical approach described in Chapter 2 as a means for analyzing potentiometric data pertaining to lipid vesicle suspensions may be advanced further, for example, by replacing the partitioning concept with the more relevant binding concept and/or by studying effects of transbilayer dielectric constant profile on drug-carrier interactions. Chapter 3 reveals the need for advancing the theoretical models used for bilayer fluctuations description by simultaneously allowing for lateral and transverse non-uniform surfactant distribution. Successful application of the RGDA for derivation of lipid vesicle size from turbidity spectra in Chapter 4 encourages generalization of the method by using the more general and exact Mie-theory of light scattering, which will allow characterization of particles with sizes exceeding the the RGDA limits. It also calls for the method generalization to light absorbing, and not merely scattering, colloidal systems.

6 Zusammenfassung

Der Einsatz von kolloidalen Trägern bei der Arzneimittelverabreichung wächst seit Jahrzehnten. Auf dem Gebiet der Pharmazie schaffte das einen Bedarf nach besserem Verständnis von physikalischen und physiko-chemischen Eigenschaften solcher, oft komplexen, kolloidalen Systeme. Das Ziel dieser Arbeit ist dieses Verständnis zu fördern und neue, einfache Techniken zu etablieren, die für die Entwicklung und Charakterisierung von kolloidalen Arzneimittelträgern nützlich sind.

Folglich schlagen wir im Kapitel 2 einen neuen Ansatz zur Analyse potenziometrischer Daten vor. Wir erklären und illustrieren diese beispielhaft an Suspensionen von arzneimittelbeladenen Lipidvesikeln. Unser Model berücksichtigt erstmalig korrekt die elektrostatische, Coulomb'sche Wechselwirkung, die gemeinsam mit der hydrophoben Wechselwirkung für Verbindung zwischen Arzneimittelmolekülen und den Trägern sorgt. Der Ansatz wurde durch Untersuchungen von vier illustrativen, ionisierbaren Arzneimitteln getestet: Die beiden anionischen Stoffe Diklofenac und Ketoprofen und die beiden kationischen Stoffe Bupivacain and Terbinafin, jeweils in Wechselwirkung mit den neutralen Phosphatidylcholinmembranen und/oder mit den negativ geladenen Phosphatidylcholin-Phosphatidylglycerol Mischmembranen.

Die neue analytische Methode erklärt potenziometrische Daten, die in komplexen Systemen erhoben wurden, besser als der herkömmliche Deutungsansatz. Die neue Methode liefert außerdem genauere und sicherere Werte für den Membran-Wasser Verteilungskoeffizienten der ionisierbaren Arzneimittel. Ein weiterer Vorteil des neuen, in dieser Arbeit beschriebenen, analytischen Verfahrens gegenüber dem herkömmlichen Verfahren ist, dass die neue Methode unabhängig von den Versuchsbedingungen ist, welche die elektrostatische, Coulomb'sche Wechselwirkung beeinflussen, wie zum Beispiel Lipid-Arzneimittel-Verhältnis und Ionenstärke. Das neue analytische Verfahren erlaubt ferner Untersuchungen von Arzneimittelmolekülen mit einem hohen P^I -Wert (d.h. einem hohen Verteilungskoeffizienten für die geladene Molekülform), wie zum Beispiel Terbinafin, das mit der her-

kömmlichen Methode nicht befriedigend analysiert werden kann.

Kapitel 3 befasst sich mit der Transformation von Vesikeln in Mizellen, die aus Phosphatidylcholin–Cholat-Gemischen bestehen, unter besonderer Berücksichtigung von Krümmungseffekten in der Lipiddoppelschicht. Dafür untersuchten wir den Einfluss der ursprünglichen Aggregatgröße auf die Veränderung der Vesikel in die cholat-dominierten Mischmizellen. Die experimentelle Grundlage dafür waren die Messungen der statischen und dynamischen Lichtstreuung an entsprechenden Suspensionen. Anders als frühere Forscher auf diesem Gebiet sorgten wir dabei für eine Komplettionisierung der Cholatmoleküle durch die Alkalinität von Suspensionen mit $\text{pH} = 10,25$. Außerdem analysierten wir die Ergebnisse quantitativ mittels mehrerer theoretischer Modelle.

Das resultierende Bild der Vesikel-Mizellen-Transformation ist reicher und komplexer als zuvor bekannt. Nach unserer Ansicht besteht solche Transformation größenweise aus zwei weitgehend parallelen Hauptvorgängen. Der erste Vorgang verringert graduell die scheinbare Größe von Mischaggregaten und schließt mit ein: Die zunehmende Destabilisierung der Doppelschicht, Doppelschichtfragmentierung, sowie Bildung von Fadenmizellen, deren Größe sich letztlich verringert. Der zweite Vorgang spiegelt sich in einer scheinbaren Aggregatgrössenzunahme wider. Diese geht hauptsächlich auf die Membranfusion, Vesikelneubildung und/oder das Wachsen von fadenartigen Protrusionen aus der Doppelschicht zurück.

Quantitative Datenanalysen lieferten weitere Einsichten. Cholatzugabe in kleinen Mengen erzeugt Doppelschichtfluktuationen. Diese sind an den ursprünglich relativ großen Vesikeln relativ stark ausgeprägt, vor allem, weil solche Vesikel ein breiteres Fluktuationsspektrum zulassen und deren Oberflächenkrümmung das Flip-Flop (der Cholatmoleküle) relativ wenig hemmen. Aus gleichem Grund können die ursprünglich relativ großen Vesikel mehr Cholat in der Doppelschicht verkräften und lösen sich folglich erst bei einer relativ hohen Cholatkonzentrationen auf.

Die experimentelle Befunde, die im Kapitel 3 beschrieben sind, mahnen aber auch zur Vorsicht in mehreren Hinsichten: *i*) Die sehr populäre “Konzentration der Doppelschicht-sättigung” ist kein zuverlässiges “Charakteristikum”, da sie einen meßmethoden-, herstellungsgeschichts- und größenabhängigen Wert einnimmt, zumindest, wenn dieser Wert mittels optischer Messungen bestimmt wird; *ii*) Die Messergebnisse, die nur teilweise ionisiertes Cholat involvieren, sind wegen der wechselseitigen Effekte der Grenzschicht auf die molekulare Ladung, und umgekehrt, zweifelhaft; *iii*) Die “Konzentration der Doppelschicht-

solubilisierung", die als einziges Suspensionscharakteristikum aus optischen Messungen zuverlässig abgeleitet werden kann, hängt von der anfänglichen Größe der getesteten Lipidaggregate ab und kann von der langsamen Veränderungskinetik überlagert sein; *iv*) Die Annahme, dass Mischaggregate eine konstante and lateral gleichmäßige Zusammensetzung haben, ist nicht haltbar.

Im Kapitel 4 untersuchen wir die Möglichkeit der Verwendung von UV/Vis Spektroskopie zur Charakterisierung von submikroskopischen Arzneimittelträgern, wie zum Beispiel Lipidvesikeln. Zuerst nehmen wir im Rahmen der Rayleigh-Gans-Debye Annäherung (RGDA) die Parameter unter die Lupe, die das Trübheitsspektrum, $\tau(\lambda)$, von submikroskopischen, lichtstreuenden, suspendierten Teilchen beliebiger Art beeinflussen. Dann wenden wir die RGDA zur Analyse unterschiedlicher Suspensionstrübheitsspektren ($\lambda = 400\text{--}600\text{ nm}$) am Beispiel der extrudierten Lipidvesikel mit mittlerem Durchmesser im Bereich $\sim 70\text{ nm} \leq 2r \leq 110\text{ nm}$ an. Wir widmen uns auch den Änderungen der mittleren Größe solcher Vesikel, welche durch Cholatzugabe ausgelöst werden, jeweils die dynamische Lichtstreuung zur Kontrolle einsetzend.

Unsere Ergebnisse implizieren, dass die experimentellen Trübheitsspektren ausreichend viel Information enthalten, um daraus schnelle, genaue und viskositätsunabhängige Charakteristika von submikroskopischen Teilchen ableiten zu können. Eine gute Grundlage dafür ist das Potenz-Gesetz, das die Trübung solcher Teilchensuspensionen beschreibt, $\tau(\lambda) \propto \lambda^{w(\lambda)}$ (oder genauer: das dazugehörige Potenzspektrum, $w(\lambda)$). Die entsprechenden Analysen lieferten ähnliche mittlere Durchmesser für die getesteten Lipidvesikel ($2r = 108.4 \pm 0.4\text{ nm}$; $92.0 \pm 0.4\text{ nm}$; $71.1 \pm 0.1\text{ nm}$) wie die dynamische Lichtstreuung ($2r = 111.9 \pm 3.0\text{ nm}$; $92.3 \pm 0.8\text{ nm}$; $72.3 \pm 0.8\text{ nm}$). Beide Methoden waren auch vergleichbar geeignet, die geringen (nur einige Nanometer betragenden), cholatinduzierten Änderungen der mittleren Vesikelgröße zu offenbaren und zu quantifizieren.

Die fortschrittlichen analytischen Methoden, die im Rahmen dieser Arbeit entwickelt und untersucht wurden, eignen sich gut für die Anwendung in der pharmazeutischen Forschung, insbesondere zur Charakterisierung von kolloidalen Trägern und in der Qualitätskontrolle; Die neuen Methoden können mehrere wichtige Eigenschaften solcher komplexen Formulierungen beleuchten und deren Grundlage erklären. Der Einsatz von dieser neu vorgeschlagenen analytischen Methoden öffnet außerdem die Tore für weitere Fortentwicklungen. Die im Kapitel 2 beschriebene Verbesserung der potenziometrischen Datenanalytik könnte zum Beispiel verfeinert werden, indem das Verteilungskonzept durch das realistischere

Konzept der Bindung ersetzt wird und/oder durch das Studium der Effekte des dielektrischen Profils innerhalb der Doppelschicht und ihrer Nähe auf die Arzneimittel-Träger Wechselwirkungen. Kapitel 3 offenbart den Bedarf für die Weiterentwicklung von theoretischen Modellen, welche für die Beschreibung von Membranfluktuationen verwendet werden, unter gleichzeitiger Berücksichtigung der lateral und transversal ungleichmäßigen molekularen Verteilung innerhalb der Membran-Doppelschicht. Die erfolgreiche Anwendung von RGDA zur Bestimmung von Vesikelgröße aus Trübheitsspektrum in Kapitel 4, muntert zur Verallgemeinerung der Methode auf, die auf der allgemeineren und exakteren Mie-Theorie der Lichtstreuung aufbaut und folglich auch die Charakterisierung von Teilchen mit Größen außerhalb der RGDA Grenzen erlauben würde. Eine weitere wünschenswerte Option ist die Verallgemeinerung der beschriebenen optischen Messmethode auf die lichtabsorbierenden und nicht nur lichtstreuenden kolloidalen Systeme.

7

References

- [1] V. Wagner, A. Dullaart, A.-K. Bock, A. Zweck. The emerging nanomedicine landscape. *Nat. Biotechnol.* 24 (2006) 1211-1217.
- [2] J. Shi, A.R. Votruba, O.C. Farokhzad, R. Langer. Nanotechnology in drug delivery and tissue engineering: From discovery to applications. *Nano Lett.* 10 (2010) 3223-3230.
- [3] S. Kim, I.K. Kwon, I.C. Kwon, K. Park. Nanotechnology in drug delivery: Past, present, and future, in: M.M. de Villiers, P. Aramwit, G.S. Kwon (Eds.), *Nanotechnology in drug delivery*, Springer, New York, 2009, pp. 581-596.
- [4] M.E. Davis, Z.G. Chen, D.M. Shin. Nanoparticle therapeutics: an emerging treatment modality for cancer. *Nat. Rev. Drug Discov.* 7 (2008) 771-782.
- [5] *Nano Drug Delivery*, in, NanoMarkets, Glen Allen, 2005.
- [6] *The Nanoparticle Drug Delivery Market*, in, Cientifica Ltd., London, 2007, pp. 300.
- [7] M.M. de Villiers, P. Aramwit, G.S. Kwon (Eds.), *Nanotechnology in drug delivery*, Springer, New York, 2009.
- [8] M. Fanun (Ed.) *Colloids in drug delivery*, CRC Press, Boca Raton, 2010.
- [9] V.P. Torchilin (Ed.) *Nanoparticulates as drug carriers*, Imperial College Press, London, 2006.
- [10] D.D. Lasic, Y. Barenholz (Eds.), *Handbook of nonmedical applications of liposomes: From gene delivery and diagnostics to ecology*, CRC Press, Inc., Boca Raton, 1996.
- [11] D.D. Lasic, D. Papahadjopoulos (Eds.), *Medical applications of liposomes*, Elsevier Science B.V., Amsterdam, 1998.
- [12] M.-C. Jones, J.-C. Leroux. Polymeric micelles – a new generation of colloidal drug carriers. *Eur. J. Pharm. Biopharm.* 48 (1999) 101-111.
- [13] S. Svenson, D.A. Tomalia. Dendrimers as nanoparticulate drug carriers, in: V.P. Torchilin (Ed.), *Nanoparticulates as drug carriers*, Imperial College Press, London, 2006, pp. 277-306.

- [14] C.C. Lee, J.A. MacKay, J.M.J. Fréchet, r.C. Szoka. Designing dendrimers for biological applications. *Nat. Biotechnol.* 23 (2005) 1517-1526.
- [15] K. Mäder. Solid lipid nanoparticles as drug carriers, in: V.P. Torchilin (Ed.), *Nanoparticulates as drug carriers*, Imperial College Press, London, 2006, pp. 187-212.
- [16] W. Mehnert, K. Mäder. Solid lipid nanoparticles: Production, characterization and applications. *Adv. Drug Deliv. Rev.* 47 (2001) 165-196.
- [17] M.J. Lawrence, W. Warisnoicharoen. Recent advances in microemulsions as drug delivery vehicles, in: V.P. Torchilin (Ed.), *Nanoparticulates as drug carriers*, Imperial College Press, London, 2006, pp. 125-171.
- [18] J.M. Gutiérrez, C. González, A. Maestro, I. Solè, C.M. Pey, J. Nolla. Nano-emulsions: New applications and optimization of their preparation. *Curr. Opin. Colloid Interface Sci.* 13 (2008) 245-251.
- [19] C. Solans, P. Izquierdo, J. Nolla, N. Azemar, M.J. Garcia-Celma. Nano-emulsions. *Curr. Opin. Colloid Interface Sci.* 10 (2005) 102-110.
- [20] H. Chen, C. Khemtong, X. Yang, X. Chang, J. Gao. Nanonization strategies for poorly water-soluble drugs. *Drug Discovery Today* (2010) In press.
- [21] G. Blume, G. Cevc. Liposomes for the sustained drug release in vivo. *Biochim. Biophys. Acta* 1029 (1990) 91-97.
- [22] E. Mastrobattista, G.A. Koning, G. Storm. Immunoliposomes for the targeted delivery of antitumor drugs. *Adv. Drug Deliv. Rev.* 40 (1999) 103-127.
- [23] J.D. Byrne, T. Betancourt, L. Brannon-Peppas. Active targeting schemes for nanoparticle systems in cancer therapeutics. *Adv. Drug Deliv. Rev.* 60 (2008) 1615-1626.
- [24] C. Oerlemans, W. Bult, M. Bos, G. Storm, J.F.W. Nijssen, W.E. Hennink. Polymeric micelles in anticancer therapy: Targeting, imaging and triggered release. *Pharm. Res.* 27 (2010) 2569-2589.
- [25] P. Rivera Gil, D. Hühn, L.L. del Mercato, D. Sasse, W.J. Parak. Nanopharmacy: Inorganic nanoscale devices as vectors and active compounds. *Pharmacol. Res.* 62 (2010) 115-125.
- [26] P. Cherukuri, E.S. Glazer, S.A. Curley. Targeted hyperthermia using metal nanoparticles. *Adv. Drug Deliv. Rev.* 62 (2010) 339-345.
- [27] R. Pecora (Ed.) *Dynamic light scattering: Applications of photon correlation spectroscopy*, Plenum Press, New York, 1985.
- [28] F.R. Hallett, J. Watton, P. Krygsman. Vesicle sizing: Number distributions by

- dynamic light scattering. *Biophys. J.* 59 (1991) 357-362.
- [29] N. Ostrowsky. Liposome size measurements by photon correlation spectroscopy. *Chem. Phys. Lipids* 64 (1993) 45-56.
- [30] O. Glatter, O. Kratky (Eds.), *Small angle x-ray scattering*, Academic Press, London, 1982.
- [31] A. Guinier, G. Fournet. *Small-angle scattering of x-rays*, John Wiley & Sons, Inc., New York, 1955.
- [32] D.I. Svergun, M.H.J. Koch. Small-angle scattering studies of biological macromolecules in solution. *Rep. Prog. Phys.* 66 (2003) 1735-1782.
- [33] C. Augsten, M.A. Kiselev, R. Gehrke, G. Hause, K. Mäder. A detailed analysis of biodegradable nanospheres by different techniques—A combined approach to detect particle sizes and size distributions. *J. Pharm. Biomed. Anal.* 47 (2008) 95-102.
- [34] M.A. Kiselev, E.V. Zemlyanaya, V.K. Aswal, R.H.H. Neubert. What can we learn about the lipid vesicle structure from the small-angle neutron scattering experiment? *Eur. Biophys. J.* 35 (2006) 477-493.
- [35] M.R. Brzustowicz, A.T. Brunger. X-ray scattering from unilamellar lipid vesicles. *J. Appl. Cryst.* 38 (2005) 126-131.
- [36] L.C. Li, Y. Tian. Zeta potential, in: J. Swarbrick (Ed.), *Encyclopedia of pharmaceutical technology*, Third Edition, Vol. 6, Informa Healthcare, Inc., New York, 2007, pp. 4117-4128.
- [37] R.W. O'Brien, D.W. Cannon, W.N. Rowlands. Electroacoustic determination of particle size and zeta potential *J. Colloid Interface Sci.* 173 (1995) 406-418.
- [38] R. Greenwood. Review of the measurement of zeta potentials in concentrated aqueous suspensions using electroacoustics. *Adv. Colloid Interface Sci.* 106 (2003) 55-81.
- [39] H. Carstensen, B.W. Müller, R.H. Müller. Adsorption of ethoxylated surfactants on nanoparticles. I. Characterization by hydrophobic interaction chromatography *Int. J. Pharm.* 67 (1991) 29-37.
- [40] K.-i. Ogawara, K. Furumoto, Y. Takakura, M. Hashida, K. Higaki, T. Kimura. Surface hydrophobicity of particles is not necessarily the most important determinant in their in vivo disposition after intravenous administration in rats. *J. Control. Release* 77 (2001) 191-198.
- [41] A. Gessner, R. Waicz, A. Lieske, B.-R. Paulke, K. Mäder, R.H. Müller. Nanoparticles with decreasing surface hydrophobicities: influence on plasma protein adsorption. *Int. J. Pharm.* 196 (2000) 245-249.

- [42] M. Fröhlich, V. Brecht, R. Peschka-Süss. Parameters influencing the determination of liposome lamellarity by ^{31}P -NMR. *Chem. Phys. Lipids* 109 (2001) 103-112.
- [43] K.A. Edwards, A.J. Baeumner. Analysis of liposomes. *Talanta* 68 (2006) 1432-1441.
- [44] K. Riehemann, S.W. Schneider, T.A. Luger, B. Godin, M. Ferrari, H. Fuchs. Nanomedicine—Challenge and Perspectives. *Angew. Chem. Int. Ed.* 48 (2009) 872-897.
- [45] A. De La Zerda, C. Zavaleta, S. Keren, S. Vaithilingam, S. Bodapati, Z. Liu, J. Levi, B.R. Smith, T.-J. Ma, O. Oralkan, Z. Cheng, X. Chen, H. Dai, B.T. Khuri-Yakub, S.S. Gambhir. Carbon nanotubes as photoacoustic molecular imaging agents in living mice. *Nature Nanotech.* 3 (2008) 557-562.
- [46] S. Kim, Y.T. Lim, E.G. Soltész, A.M. De Grand, J. Lee, A. Nakayama, J.A. Parker, T. Mihaljevic, R.G. Laurence, D.M. Dor, L.H. Cohn, M.G. Bawendi, J.V. Frangioni. Near-infrared fluorescent type II quantum dots for sentinel lymph node mapping. *Nat. Biotechnol.* 22 (2003) 93-97.
- [47] B. Dubertret, P. Skourides, D.J. Norris, V. Noireaux, A.H. Brivanlou, A. Libchaber. In vivo imaging of quantum dots encapsulated in phospholipid micelles. *Science* 298 (2002) 1759-1762.
- [48] S.M. Janib, A.S. Moses, J.A. MacKay. Imaging and drug delivery using theranostic nanoparticles. *Adv. Drug Deliv. Rev.* 62 (2010) 1052-1063.
- [49] J. Xie, S. Lee, X. Chen. Nanoparticle-based theranostic agents. *Adv. Drug Deliv. Rev.* 62 (2010) 1064-1079.
- [50] M. Goldberg, R. Langer, X. Jia. Nanostructured materials for applications in drug delivery and tissue engineering. *J. Biomater. Sci. Polym. Ed.* 18 (2007) 241-268.
- [51] M. Gaumet, A. Vargas, R. Gurny, F. Delie. Nanoparticles for drug delivery: The need for precision in reporting particle size parameters. *Eur. J. Pharm. Biopharm.* 69 (2008) 1-9.
- [52] A. Nagayasu, K. Uchiyama, H. Kiwada. The size of liposomes: a factor which affects their targeting efficiency to tumors and therapeutic activity of liposomal antitumor drugs. *Adv. Drug Deliv. Rev.* 40 (1999) 75-87.
- [53] X. Wu, K. Landfester, A. Musyanovych, R.H. Guy. Disposition of charged nanoparticles after their topical application to the skin. *Skin Pharmacol. Physiol.* 23 (2010) 117-123.
- [54] N. Dragicevic-Curic, S. Gräfe, B. Gitter, S. Winter, A. Fahr. Surface charged temoporfin-loaded flexible vesicles: In vitro skin penetration studies and stability. *Int.*

- J. Pharm. 384 (2010) 100-108.
- [55] H.J. Gruber, H. Schindler. External surface and lamellarity of lipid vesicles: a practice-oriented set of assay methods. *Biochim. Biophys. Acta* 1189 (1994) 212-224.
- [56] H. Schmiedel, L. Almásy, G. Klose. Multilamellarity, structure and hydration of extruded POPC vesicles by SANS. *Eur. Biophys. J.* 35 (2006) 181-189.
- [57] J.A. Bouwstra, G.S. Gooris, W. Bras, H. Talsma. Small angle X-ray scattering: possibilities and limitations in characterization of vesicles. *Chem. Phys. Lipids* 64 (1993) 83-98.
- [58] H.L. Wong, R. Bendayan, A.M. Rauth, Y. Li, X.Y. Wu. Chemotherapy with anticancer drugs encapsulated in solid lipid nanoparticles. *Adv. Drug Deliv. Rev.* 59 (2007) 491-504.
- [59] A. Helenius, K. Simons. Solubilization of membranes by detergents. *Biochim. Biophys. Acta* 415 (1975) 29-79.
- [60] M. Ollivon, S. Lesieur, C. Grabielle-Madellmont, M. Paternostre. Vesicle reconstitution from lipid-detergent mixed micelles. *Biochim. Biophys. Acta* 1508 (2000) 34-50.
- [61] M.-T. Paternostre, M. Roux, J.-L. Rigaud. Mechanisms of membrane protein insertion into liposomes during reconstitution procedures involving the use of detergents. 1. Solubilization of large unilamellar liposomes (prepared by reverse-phase evaporation) by triton X-100, octyl glucoside, and sodium cholate. *Biochemistry* 27 (1988) 2668-2677.
- [62] J.-L. Rigaud, B. Pitard, D. Levy. Reconstitution of membrane proteins into liposomes: application to energy-transducing membrane proteins. *Biochim. Biophys. Acta* 1231 (1995) 223-246.
- [63] C.J. Alcorn, R.J. Simpson, D.E. Leahy, T.J. Peters. Partition and distribution coefficients of solutes and drugs in brush border membrane vesicles. *Biochem. Pharmacol.* 45 (1993) 1775-1782.
- [64] R.P. Austin, A.M. Davis, C.N. Manners. Partitioning of ionizing molecules between aqueous buffers and phospholipid vesicles. *J. Pharm. Sci.* 84 (1995) 1180-1183.
- [65] A. Avdeef. *Absorption and Drug Development: Solubility, Permeability, and Charge State*, John Wiley & Sons, Inc., New Jersey, 2003.
- [66] R.P. Austin, P. Barton, A.M. Davis, C.N. Manners, M.C. Stansfield. The effect of ionic strength on liposome-buffer and 1-octanol-buffer distribution coefficients. *J. Pharm. Sci.* 87 (1998) 599-607.

- [67] A. Avdeef, K.J. Box, J.E. Comer, C. Hibbert, K.Y. Tam. pH-metric logP 10. Determination of liposomal membrane-water partition coefficients of ionizable drugs. *Pharm. Res.* 15 (1998) 209-215.
- [68] B.I. Escher, S.R. P., J.C. Westall. Evaluation of liposome-water partitioning of organic acids and bases. 2. Comparison of experimental determination methods. *Environ. Sci. Technol.* 34 (2000) 3962-3968.
- [69] S.D. Krämer, J.C. Gautier, P. Saudemon. Considerations on the potentiometric log P determination. *Pharm. Res.* 15 (1998) 1310-1313.
- [70] C. Ottiger, H. Wunderli-Allenspach. Partition behaviour of acids and bases in a phosphatidylcholine liposome-buffer equilibrium dialysis system. *Eur. J. Pharm. Sci.* 5 (1997) 223-231.
- [71] A.V. Thomae, T. Koch, C. Panse, H. Wunderli-Allenspach, S.D. Kramer. Comparing the lipid membrane affinity and permeation of drug-like acids: The intriguing effects of cholesterol and charged lipids. *Pharm. Res.* 24 (2007) 1457-1472.
- [72] B. de Castro, P. Gameiro, J.L.F.C. Lima, C. Matos, S. Reis. A Fast and reliable spectroscopic method for the determination of membrane-water partition coefficients of organic compounds. *Lipids* 36 (2001) 89-96.
- [73] C. Rodrigues, P. Gameiro, S. Reis, J.L.F.C. Lima, B. de castro. Derivative spectrophotometry as a tool for the determination of drug partition coefficients in water/dimyristoyl- α -phosphatidylglycerol (DMPG) liposomes. *Biophys. Chem.* 94 (2001) 97-106.
- [74] N.C. Santos, M. Prieto, M.A.R.B. Castanho. Quantifying molecular partition into model systems of biomembranes: an emphasis on optical spectroscopic methods. *Biochim. Biophys. Acta* 1612 (2003) 123-135.
- [75] R.P. Austin, P. Barton, A.M. Davis, R.E. Fessey, M.C. Wenlock. The thermodynamics of the partitioning of ionizing molecules between aqueous buffers and phospholipid membranes. *Pharm. Res.* 22 (2005) 1649-1657.
- [76] X.Y. Liu, Q. Yang, N. Kamo, J. Miyake. Effect of liposome type and membrane fluidity on drug-membrane partitioning analyzed by immobilized liposome chromatography. *J. Chromatogr. A.* 913 (2001) 123-131.
- [77] Q. Yang, X.Y. Liu, S. Ajiki, M. Hara, P. Lundahl, J. Miyake. Avidin-biotin immobilization of unilamellar liposomes in gel beads for chromatographic analysis of drug-membrane partitioning. *J. Chromatogr. B. Biomed. Sci. Appl.* 707 (1998) 131-141.

- [78] C. Matos, B. de Castro, P. Gameiro, J.L. Lima, S. Reis. Zeta-potential measurements as a tool to quantify the effect of charged drugs on the surface potential of egg phosphatidylcholine liposomes. *Langmuir* 20 (2004) 369-377.
- [79] M. Ikonen, L. Murtomäki, K. Kontturia. An electrochemical method for the determination of liposome–water partition coefficients of drugs. *J. Electroanal. Chem.* 602 (2007) 189-194.
- [80] T. Hata, T. Sakamoto, H. Matsuki, S. Kaneshina. Partition coefficients of charged and uncharged local anesthetics into dipalmitoylphosphatidylcholine bilayer membrane: estimation from pH dependence on the depression of phase transition temperatures. *Colloids Surf. B Biointerfaces* 22 (2001) 77-84.
- [81] C. Rodrigues, P. Gameiro, S. Reis, J.L.F.C. Lima, B. De Castro. Spectrophotometric determination of drug partition coefficients in dimyristoyl-L- α -phosphatidylcholine/water: a comparative study using phase separation and liposome suspensions. *Anal. Chim. Acta* 428 (2001) 103-109.
- [82] A. Hildebrand, K. Beyer, R. Neubert, P. Garidel, A. Blume. Temperature dependence of the interaction of cholate and deoxycholate with fluid model membranes and their solubilization into mixed micelles. *Colloids Surf. B: Biointerfaces* 32 (2003) 335-351.
- [83] K. Balon, B.U. Riebesehl, B.W. Muller. Drug liposome partitioning as a tool for the prediction of human passive intestinal absorption. *Pharm. Res.* 16 (1999) 882-888.
- [84] J. Lasch. Interaction of detergents with lipid vesicles. *Biochim. Biophys. Acta* 1241 (1995) 269-292.
- [85] F.H. Clarke. Ionization constants by curve fitting: application to the determination of partition coefficients. *J. Pharm. Sci.* 73 (1984) 226-230.
- [86] F.H. Clarke, N.M. Cahoon. Ionization constants by curve fitting: determination of partition and distribution coefficients of acids and bases and their ions. *J. Pharm. Sci.* 76 (1987) 611-620.
- [87] S. Ohki. Adsorption of local anesthetics on phospholipid membranes. *Biochim. Biophys. Acta* 777 (1984) 56-66.
- [88] P.G. Thomas, J. Seelig. Binding of the calcium antagonist flunarizine to phosphatidylcholine bilayers: charge effects and thermodynamics. *Biochem. J.* 291 (1993) 397-402.
- [89] M.S. Fernandez, P. Fromherz. Lipoid pH indicators as probes of electrical potential and polarity in micells. *J. Phys. Chem.* 81 (1977) 1755-1761.
- [90] E. Kuchinka, J. Seelig. Interaction of melittin with phosphatidylcholine membranes.

- Binding isotherm and lipid head-group conformation. *Biochemistry* 28 (1989) 4216-4221.
- [91] H.D. Bäuerle, J. Seelig. Interaction of charged and uncharged calcium channel antagonists with phospholipid membranes. Binding equilibrium, binding enthalpy, and membrane location. *Biochemistry* 30 (1991) 7203-7211.
- [92] A. Hildebrand, R. Neubert, P. Garidel, A. Blume. Bile salt induced solubilization of synthetic phosphatidylcholine vesicles studied by isothermal titration calorimetry *Langmuir* 18 (2002) 2836-2847.
- [93] A. Seelig, P.R. Allegrini, J. Seelig. Partitioning of local anesthetics into membranes: surface charge effects monitored by the phospholipid head-group. *Biochim. Biophys. Acta* 939 (1988) 267-276.
- [94] P. Friberger, G. Aberg. Some physicochemical properties of the racemates and the optically active isomers of two local anaesthetic compounds. *Acta Pharm. Suec.* 8 (1971) 361-364.
- [95] M. Meloun, S. Bordovská, L. Galla. The thermodynamic dissociation constants of four non-steroidal anti-inflammatory drugs by the least-squares nonlinear regression of multiwavelength spectrophotometric pH-titration data. *J. Pharm. Biomed. Anal.* 45 (2007) 552-564.
- [96] A. Avdeef, C.M. Berger, C. Brownell. pH-metric solubility. 2: correlation between the acid-base titration and the saturation shake-flask solubility-pH methods. *Pharm. Res.* 17 (2000) 85-89.
- [97] J.M. Carrozzino, Drug Partitioning and Solvation Environments in Lipid Bilayers, in: Department of Chemistry, North Carolina State University, Raleigh, 2004, pp. 224.
- [98] K. Ohsawa, H. Ohshima. Electrophoretic mobility and isoelectric point of purified brush border membrane vesicles. *Electrophoresis* 5 (1984) 148-154.
- [99] M. Sugawara, H. Oikawa, M. Kobayashi, K. Iseki, K. Miyazaki. Effect of membrane surface potential on the uptake and the inhibition of cationic compounds in rat intestinal brush-border membrane vesicles and liposomes. *Biochim. Biophys. Acta* 1234 (1995) 22-28.
- [100] C. Engvall, P. Lundahl. Drug partition chromatography on immobilized porcine intestinal brush border membranes. *J. Chromatogr. A* 1031 (2004) 107-112.
- [101] G. Cevc. Electrostatic characterization of liposomes. *Chem. Phys. Lipids* 64 (1993) 163-186.
- [102] P. Garidel, A. Hildebrand, K. Knauf, A. Blume. Membranolytic activity of bile salts:

- Influence of biological membrane properties and composition. *Molecules* 12 (2007) 2292-2326.
- [103] R. Schubert, Relationship between the structure of bile salts and their interaction with membrane lipids, in: *Proceedings of M.o.B.B.E.L.*, Tannheim, Austria, 1989, pp. 1-17.
- [104] P. Garidel, J. Lasch. Mixed vesicles and mixed micelles: Formation, thermodynamic stability, and pharmaceutical aspects, in: G. Gregoriadis (Ed.), *Liposome technology, Volume I: Liposome preparation and related techniques*, Third Edition, Informa Healthcare USA, Inc., New York, 2007, pp. 209-239.
- [105] G. Cevc. Lipid vesicles and other colloids as drug carriers on the skin. *Adv. Drug Deliv. Rev.* 56 (2004) 675-711.
- [106] M.M.A. Elsayed, O.Y. Abdallah, V.F. Naggar, N.M. Khalafallah. Lipid vesicles for skin delivery of drugs: Reviewing three decades of research. *Int. J. Pharm.* 332 (2007) 1-16.
- [107] J. Guo, Q. Ping, L. Zhang. Transdermal delivery of insulin in mice by using lecithin vesicles as a carrier. *Drug Deliv.* 7 (2000) 113-116.
- [108] G. Cevc. Transfersomes, liposomes and other lipid suspensions on the skin: Permeation enhancement, vesicle penetration, and transdermal drug delivery. *Crit. Rev. Ther. Drug Carrier Syst.* 13 (1996) 257-388.
- [109] G. Cevc. Transdermal drug delivery of insulin with ultradeformable carriers. *Clin. Pharmacokinet.* 42 (2003) 461-474.
- [110] G. Cevc, D. Gebauer, J. Stieber, A. Schätzlein, G. Blume. Ultraflexible vesicles, transfersomes, have an extremely low pore penetration resistance and transport therapeutic amounts of insulin across the intact mammalian skin. *Biochim. Biophys. Acta* 1368 (1998) 201-215.
- [111] M.M.A. Elsayed, O.Y. Abdallah, V.F. Naggar, N.M. Khalafallah. Deformable liposomes and ethosomes as carriers for skin delivery of ketotifen. *Pharmazie* 62 (2007) 133-137.
- [112] A. Paul, G. Cevc. Noninvasive administration of protein antigens: Transdermal immunization with bovine serum albumin in transfersomes. *Vaccine Res.* 4 (1995) 145-164.
- [113] A. Paul, G. Cevc, B.K. Bachhawat. Transdermal immunisation with an integral membrane component, gap junction protein, by means of ultradeformable drug carriers, transfersomes. *Vaccine* 16 (1998) 188-195.

- [114] S. Almog, T. Kushnir, S. Nir, D. Lichtenberg. Kinetic and structural aspects of reconstitution of phosphatidylcholine vesicles by dilution of phosphatidylcholine-sodium cholate mixed micelles. *Biochemistry* 25 (1986) 2597-2605.
- [115] A. De la Maza, J.L. Parra. Vesicle to micelle phase transitions involved in the interaction of sodium cholate with phosphatidylcholine liposomes. *Colloids Surf. A* 127 (1997) 125-134.
- [116] M.A. Long, E.W. Kaler, S.P. Lee. Structural characterization of the micelle-vesicle transition in lecithin-bile salt solutions. *Biophys. J.* 67 (1994) 1733-1742.
- [117] D. Meyuhas, A. Bor, I. Pinchuk, A. Kaplun, Y. Talmon, M.M. Kozlov, D. Lichtenberg. Effect of Ionic Strength on the Self-Assembly in Mixtures of Phosphatidylcholine and Sodium Cholate. *J. Colloid Interface Sci.* 188 (1997) 351-362.
- [118] R. Schubert, K.H. Schmidt. Structural changes in vesicle membranes and mixed micelles of various lipid compositions after binding of different bile salts. *Biochemistry* 27 (1988) 8787-8794.
- [119] D.M. Small. A classification of biologic lipids based upon their interaction in aqueous systems. *J. Am. Oil Chem. Soc.* 45 (1968) 108-119.
- [120] A. Walter, P.K. Vinson, A. Kaplun, Y. Talmon. Intermediate structures in the cholate-phosphatidylcholine vesicle-micelle transition. *Biophys. J.* 60 (1991) 1315-1325.
- [121] J.S. Pedersen, S.U. Egelhaaf, P. Schurtenberger. Formation of polymerlike mixed micelles and vesicles in lecithin-bile salt solutions: A small-angle neutron-scattering study. *J. Phys. Chem.* 99 (1995) 1299-1305.
- [122] R.P. Hjelm Jr., P. Thiyagarajan, H. Alkan-Onyuksel. Organization of phosphatidylcholine and bile salt in rodlike mixed micelles. *J. Phys. Chem.* 96 (1992) 8653-8661.
- [123] N.A. Mazer, G.B. Benedek, M.C. Carey. Quasielastic light-scattering studies of aqueous biliary lipid systems. Mixed micelle formation in bile salt-lecithin solutions. *Biochemistry* 19 (1980) 601-615.
- [124] M.C. Carey, D.M. Small. Micelle formation by bile salts. Physical-chemical and thermodynamic considerations. *Arch. Intern. Med.* 130 (1972) 506-527.
- [125] A. Alonso, R. Sáez, A. Villena, F.M. Goñi. Increase in size of sonicated phospholipid vesicles in the presence of detergents. *J. Membr. Biol.* 67 (1982) 55-62.
- [126] W. Shankland. The equilibrium and structure of lecithin-cholate mixed micelles. *Chem. Phys. Lipids* 4 (1970) 109-130.

- [127] D.M. Small, M.C. Bourgès, D.G. Dervichian. The biophysics of lipidic associations: I. The ternary systems lecithin-bile salt-water. *Biochim. Biophys. Acta* 125 (1966) 563-580.
- [128] A. Nasner, L. Kraus. Quantitative Bestimmung von Phosphatidylcholin mit Hilfe der HPLC. *Fette, Seifen, Anstrichmittel* 83 (1981) 70-73.
- [129] M. Grit, D.J.A. Crommelin, J. Lang. Determination of phosphatidylcholine, phosphatidylglycerol and their lyso forms from liposome dispersions by high-performance liquid chromatography using high-sensitivity refractive index detection. *J. Chromatogr.* 585 (1991) 239-246.
- [130] S.W. Provencher. CONTIN: A general purpose constrained regularization program for inverting noisy linear algebraic and integral equations. *Comput. Phys. Commun.* 27 (1982) 229-242.
- [131] S.W. Provencher. A constrained regularization method for inverting data represented by linear algebraic or integral equations. *Comput. Phys. Commun.* 27 (1982) 213-227.
- [132] G. Pereira, R. Moreira, M.J. Vázquez, F. Chenlo. Kinematic viscosity prediction for aqueous solutions with various solutes. *Chem. Eng. J.* 81 (2001) 35-40.
- [133] T. Wang, T.-C. Bai, W. Wang, J.-J. Zhu, C.-W. Zhu. Viscosity and activation parameters of viscous flow of sodium cholate aqueous solution. *J. Mol. Liq.* 142 (2008) 150-154.
- [134] M.J. Hope, M.B. Bally, G. Webb, P.R. Cullis. Production of large unilamellar vesicles by a rapid extrusion procedure. Characterization of size distribution, trapped volume and ability to maintain a membrane potential. *Biochim. Biophys. Acta* 812 (1985) 55-65.
- [135] W. Helfrich. Size distributions of vesicles: the role of the effective rigidity of membranes. *J. Physique* 47 (1986) 321-329.
- [136] J.F. Faucon, M.D. Mitov, P. Méléard, I. Bivas, P. Bothorel. Bending elasticity and thermal fluctuations of lipid membranes. Theoretical and experimental requirements. *J. Physique* 50 (1989) 2389-2414.
- [137] H.I. Petrache, N. Gouliarov, S. Tristram-Nagle, R. Zhang, R.M. Suter, J.F. Nagle. Interbilayer interactions from high-resolution x-ray scattering. *Phys. Rev. E* 57 (1998) 7014-7024.
- [138] W. Rawicz, K.C. Olbrich, T. McIntosh, D. Needham, E. Evans. Effect of chain length and unsaturation on elasticity of lipid bilayers. *Biophys. J.* 79 (2000) 328-339.
- [139] T. Nakashima, T. Anno, H. Kanda, Y. Sato, T. Kuroi, H. Fujii, S. Nagadome, G.

- Sugihara. Potentiometric study on critical micellization concentrations (CMC) of sodium salts of bile acids and their amino acid derivatives. *Colloids Surf. B: Biointerfaces* 24 (2002) 103-110.
- [140] D.J. Cabral, J.A. Hamilton, D.M. Small. The ionization behavior of bile acids in different aqueous environments. *J. Lipid. Res.* 27 (1986) 334-343.
- [141] D.M. Small, D.J. Cabral, D.P. Cistola, J.S. Parks, J.A. Hamilton. The ionization behavior of fatty acids and bile acids in micelles and membranes. *Hepatology* 4 (1984) 77S-79S.
- [142] G. Cevc. Membrane electrostatics. *Biochim. Biophys. Acta* 1031 (1990) 311-382.
- [143] M. Grit, D.J. Crommelin. The effect of surface charge on the hydrolysis kinetics of partially hydrogenated egg phosphatidylcholine and egg phosphatidylglycerol in aqueous liposome dispersions. *Biochim. Biophys. Acta* 1167 (1993) 49-55.
- [144] M. Grit, J.H. de Smidt, A. Struijke, D.J. Crommelin. Hydrolysis of phosphatidylcholine in aqueous liposome dispersions. *Int. J. Pharm.* 50 (1989) 1-6.
- [145] F. Ollila, J.P. Slotte. A thermodynamic study of bile salt interactions with phosphatidylcholine and sphingomyelin unilamellar vesicles. *Langmuir* 17 (2001) 2835-2840.
- [146] H. Heerklotz. Interactions of surfactants with lipid membranes. *Q. Rev. Biophys.* 41 (2008) 205-264.
- [147] C. Sun, Y. Sano, H. Kashiwagi, M. Ueno. Characterization of aggregate structures of phospholipid in the process of vesicle solubilization with sodium cholate using laser light scattering method. *Coll. Polym. Sci.* 280 (2002) 900-907.
- [148] P.K. Vinson, Y. Talmon, A. Walter. Vesicle-micelle transition of phosphatidylcholine and octyl glucoside elucidated by cryo-transmission electron microscopy. *Biophys. J.* 56 (1989) 669-681.
- [149] E. Evans, W. Rawicz, A.F. Hoffman. Lipid bilayer expansion and mechanical disruption in solution of water-soluble bile acid, in: A.F. Hoffman, G. Paumgartner, A. Stiehl (Eds.), *Bile acids in gastroenterology: Basic and clinical advances: proceedings of the 80th Falk Symposium* Kluwer Academic Publishers, Lancaster, 1995, pp. 59-68.
- [150] G. Cevc, A.G. Schätzlein, H. Richardsen, U. Vierl. Overcoming semipermeable barriers, such as the skin, with ultradeformable mixed lipid vesicles, transfersomes, liposomes, or mixed lipid micelles. *Langmuir* 19 (2003) 10753-10763.
- [151] G. Cevc, G. Blume, A. Schätzlein, D. Gebauer, A. Paul. The skin: A pathway for

- systemic treatment with patches and lipid-based agent carriers. *Adv. Drug Deliv. Rev.* 18 (1996) 349-378.
- [152] G. Cevc, D. Gebauer. Hydration-driven transport of deformable lipid vesicles through fine pores and the skin barrier. *Biophys. J.* 84 (2003) 1010-1024.
- [153] F. Nomura, M. Nagata, T. Inaba, H. Hiramatsu, H. Hotani, K. Takiguchi. Capabilities of liposomes for topological transformation. *Proc. Natl. Acad. Sci. U. S. A.* 98 (2001) 2340-2345.
- [154] M.F. Brown, R.L. Thurmond, S.W. Dodd, D. Otten, K. Beyer. Elastic deformation of membrane bilayers probed by deuterium NMR relaxation. *J. Am. Chem. Soc.* 124 (2002) 8471-8484.
- [155] S. Leibler. Curvature instability in membranes. *J. Physique* 47 (1986) 507-516.
- [156] C. Wachter, U. Vierl, G. Cevc. Adaptability and elasticity of the mixed lipid bilayer vesicles containing non-ionic surfactant designed for targeted drug delivery across the skin. *J. Drug Target.* 16 (2008) 611-625.
- [157] D.J. Cabral, D.M. Small, H.S. Lilly, J.A. Hamilton. Transbilayer movement of bile acids in model membranes. *Biochemistry* 26 (1987) 1801-1804.
- [158] J.M. Donovan, A.A. Jackson. Transbilayer movement of fully ionized taurine-conjugated bile salts depends upon bile salt concentration, hydrophobicity, and membrane cholesterol content. *Biochemistry* 36 (1997) 11444-11451.
- [159] M. Ueno, N. Hirota, H. Kashiwagi, S. Sagasaki. Process of destruction of large unilamellar vesicles by a nonionic detergent, octylglucoside, and size growth factor in vesicle formation from phospholipid-detergent mixed micelles. *Coll. Polym. Sci.* 282 (2003) 69-75.
- [160] P. Fromherz. Modulation of the edge-tension of lipid membranes by cholate and cholesterol and the micelle-vesicle transition in model bile systems, in: W. Swobodnik, H. Ditschuneit, R.D. Soloway (Eds.), *Gallstone Disease*, Springer, Berlin, 1990, pp. 27-33.
- [161] P. Fromherz. Lipid-vesicle structure: Size control by edge-active agents. *Chem. Phys. Lett.* 94 (1983) 259-266.
- [162] P. Schurtenberger, N. Mazer, S. Waldvogel, W. Känzig. Preparation of monodisperse vesicles with variable size by dilution of mixed micellar solutions of bile salt and phosphatidylcholine. *Biochim. Biophys. Acta* 775 (1984) 111-114.
- [163] D.D. Lasič. A molecular model for vesicle formation. *Biochim. Biophys. Acta* 692 (1982) 501-502.

- [164] R. Schubert. Liposome preparation by detergent removal. *Methods Enzymol.* 367 (2003) 46-70.
- [165] H.G. Weder, O. Zumbuehl. The preparation of variably sized homogenous liposomes for laboratory, clinical, and industrial use by controlled detergent dialysis, in: G. Gregoriadis (Ed.), *Liposome technology, Volume I: Preparation of liposomes*, CRC press, Boca Raton, 1984, pp. 79-107.
- [166] Y. Roth, E. Opatowski, D. Lichtenberg, M.M. Kozlov. Phase behavior of dilute aqueous solutions of lipid-surfactant mixtures: Effects of finite size of micelles. *Langmuir* 16 (2000) 2052-2061.
- [167] M.M. Elsayed, U. Vierl, G. Cevc. Accurate potentiometric determination of lipid membrane-water partition coefficients and apparent dissociation constants of ionizable drugs: Electrostatic corrections. *Pharm. Res.* 26 (2009) 1332-1343.
- [168] C.S. Chong, K. Colbow. Light scattering and turbidity measurements on lipid vesicles. *Biochim. Biophys. Acta* 436 (1976) 260-282.
- [169] M.E. Cates, S.J. Candau. Statics and dynamics of worm-like surfactant micelles. *J. Phys.: Condens. Matter* 2 (1990) 6869-6892.
- [170] M.M. Kozlov, D. Lichtenberg, D. Andelman. Shape of phospholipid/surfactant mixed micelles: Cylinders or Disks? Theoretical analysis. *J. Phys. Chem. B* 101 (1997) 6600-6606.
- [171] H. Ohshima, T.W. Healy, L.R. White. Accurate analytic expressions for the surface charge density/surface potential relationship and double-layer potential distribution for a spherical colloidal particle. *J. Colloid Interface Sci.* 90 (1982) 17-26.
- [172] E. Merisko-Liversidge, G.G. Liversidge, E.R. Cooper. Nanosizing: a formulation approach for poorly-water-soluble compounds. *Eur. J. Pharm. Sci.* 18 (2003) 113-120.
- [173] C. Peetla, A. Stine, V. Labhasetwar. Biophysical interactions with model lipid membranes: applications in drug discovery and drug delivery. *Mol. Pharmaceutics* 6 (2009) 1264-1276.
- [174] K. Fowler, L.A. Bottomley, H. Schreier. Surface topography of phospholipid bilayers and vesicles (liposomes) by scanning tunneling microscopy (STM). *J. Control. Release* 22 (1992) 283-291.
- [175] B. Ruozi, G. Tosi, E. Leo, M.A. Vandelli. Application of atomic force microscopy to characterize liposomes as drug and gene carriers. *Talanta* 73 (2007) 12-22.
- [176] J. Sitterberg, A. Özçetin, C. Ehrhardt, U. Bakowsky. Utilising atomic force microscopy for the characterisation of nanoscale drug delivery systems. *Eur. J. Pharm.*

- Biopharm. 74 (2010) 2-13.
- [177] A. Guinier. X-ray diffraction in crystals, imperfect crystals and amorphous bodies, W. H. Freeman and Company, San Francisco, 1963.
- [178] B.H. Zimm. The Scattering of Light and the Radial Distribution Function of High Polymer Solutions. *J. Chem. Phys.* 16 (1948) 1093-1099.
- [179] B.H. Zimm. Apparatus and Methods for Measurement and Interpretation of the Angular Variation of Light Scattering; Preliminary Results on Polystyrene Solutions. *J. Chem. Phys.* 16 (1948) 1099-1116.
- [180] A.J. Jin, D. Huster, K. Gawrisch, R. Nossal. Light scattering characterization of extruded lipid vesicles. *Eur. Biophys. J.* 28 (1999) 187-199.
- [181] J. Pencer, G.F. White, F.R. Hallett. Osmotically induced shape changes of large unilamellar vesicles measured by dynamic light scattering. *Biophys. J.* 81 (2001) 2716-2728.
- [182] J. Pencer, F.R. Hallett. Effects of vesicle size and shape on static and dynamic light scattering measurements. *Langmuir* 19 (2003) 7488-7497.
- [183] J.H. Van Zanten, H.G. Monbouquette. Characterization of vesicles by classical light scattering. *J. Colloid Interface Sci.* 146 (1991) 330-336.
- [184] J.H. Van Zanten, H.G. Monbouquette. Phosphatidylcholine vesicle diameter, molecular weight and wall thickness determined by static light scattering *J. Colloid Interface Sci.* 165 (1994) 512-518.
- [185] B.A. Korgel, J.H.v. Zanten, H.G. Monbouquette. Vesicle size distributions measured by flow field-flow fractionation coupled with multiangle light scattering. *Biophys. J.* 74 (1998) 3264-3272.
- [186] W. Heller. Theoretical Investigations on the Light Scattering of Spheres. XV. The Wavelength Exponents at Small α Values. *J. Chem. Phys.* 40 (1964) 2700-2705.
- [187] W. Heller, H.L. Bhatnagar, M. Nakagaki. Theoretical Investigations on the Light Scattering of Spheres. XIII. The "Wavelength Exponent" of Differential Turbidity Spectra. *J. Chem. Phys.* 36 (1962) 1163-1170.
- [188] W. Heller, H.B. Klevens, H. Oppenheimer. The Determination of Particle Sizes from Tyndall Spectra. *J. Chem. Phys.* 14 (1946) 566-567.
- [189] W. Heller, E. Vassy. Tyndall Spectra, Their Significance and Application. *J. Chem. Phys.* 14 (1946) 565-566.
- [190] B.N. Khlebtsov, L.A. Kovler, V.A. Bogatyrev, N.G. Khlebtsov, S.Y. Shchyogolev. Studies of phosphatidylcholine vesicles by spectroturbidimetric and dynamic light

- scattering methods *J. Quant. Spectrosc. Radiat. Transf.* 79-80 (2003) 825-838.
- [191] K. Matsuzaki, O. Murase, K. Sugishita, S. Yoneyama, K. Akada, M. Ueha, A. Nakamura, S. Kobayashi. Optical characterization of liposomes by right angle light scattering and turbidity measurement. *Biochim. Biophys. Acta* 1467 (2000) 219-226.
- [192] B.N. Khlebtsov, V.A. Khanadeev, N.G. Khlebtsov. Determination of the size, concentration, and refractive index of silica nanoparticles from turbidity spectra. *Langmuir* 24 (2008) 8964-8970.
- [193] H.I. Petrache, S. Tristram-Nagle, J.F. Nagle. Fluid phase structure of EPC and DMPC bilayers. *Chem. Phys. Lipids*. 95 (1998) 83-94.
- [194] P. Balgavý, M. Dubnicková, N. Kucerka, M.A. Kiselev, S.P. Yaradaikin, D. Uhríková. Bilayer thickness and lipid interface area in unilamellar extruded 1,2-diacylphosphatidylcholine liposomes: a small-angle neutron scattering study. *Biochim. Biophys. Acta* 1512 (2001) 40-52.
- [195] N. Kučerka, J. Gallová, D. Uhríková, P. Balgavý, M. Bulacu, S.-J. Marrink, J. Katsaras. Areas of monounsaturated diacylphosphatidylcholines. *Biophys. J.* 97 (2009) 1926-1932.
- [196] G. Cevc (Ed.) *Phospholipids Handbook*, Marcel Dekker, Inc., New York, 1993.
- [197] M. Kerker. *The scattering of light and other electromagnetic radiation*, Academic Press, Inc., New York, 1969.
- [198] H.C. van de Hulst. *Light scattering by small particles*, Dover Publications, Inc., New York, 1981.
- [199] W. Heller, M. Nakagaki, M.L. Wallach. Theoretical Investigations on the Light Scattering of Colloidal Spheres. V. Forward Scattering. *J. Chem. Phys.* 30 (1959) 444-450.
- [200] J.H. Van Zanten. Characterization of vesicles and vesicular dispersions via scattering techniques, in: M. Rosoff (Ed.), *Vesicles*, Tenth Edition, Marcel Dekker, Inc., New York, 1996, pp. 239-294.
- [201] L. Rayleigh. On the diffraction of light by spheres of small relative index. *Proc. R. Soc. Lond. A* 90 (1914) 219-225.
- [202] L. Rayleigh. On the scattering of light by spherical shells, and by complete spheres of periodic structure, when the refractivity is small. *Proc. R. Soc. Lond. A* 94 (1918) 296-300.
- [203] M. Kerker, J.P. Kratochvil, E. Matijević. Light scattering functions for concentric spheres. Total scattering coefficients, $m_1 = 2.1050$, $m_2 = 1.4821$. *J. Opt. Soc. Am.* 52

- (1962) 551-561.
- [204] R. Pecora, S.R. Aragón. Theory of light scattering from hollow spheres. *Chem. Phys. Lipids* 13 (1974) 1-10.
- [205] B.G. Tenchov, T.K. Yanev, M.G. Tihova, R.D. Koynova. A probability concept about size distributions of sonicated lipid vesicles. *Biochim Biophys Acta* 816 (1985) 122-130.
- [206] B.G. Tenchov, T.K. Yanev. Weibull distribution of particle sizes obtained by uniform random fragmentation. *J. Colloid Interface Sci.* 111 (1986) 1-7.
- [207] M.M.A. Elsayed, G. Cevc. The vesicle-to-micelle transformation of phospholipid–cholate mixed aggregates: A state of the art analysis including membrane curvature effects. *Biochim. Biophys. Acta* 1808 (2011) 140-153.
- [208] L.D. Mayer, M.J. Hope, P.R. Cullis. Vesicles of variable sizes produced by a rapid extrusion procedure. *Biochim. Biophys. Acta* 858 (1986) 161-168.
- [209] W. Yoshikawa, H. Akutsu, Y. Kyogoku. Light-scattering properties of osmotically active liposomes. *Biochim. Biophys. Acta* 735 (1983) 397-406.
- [210] M.A.R.B. Castanho, N.C. Santos, M.S. Loura. Separating the turbidity spectra of vesicles from the absorption spectra of membrane probes and other chromophores. *Eur. Biophys. J.* 26 (1997) 53-59.
- [211] M. Kerker, W.A. Farone, E. Matijevic. Applicability of Rayleigh-Gans Scattering to spherical particles. *J. Opt. Soc. Am.* 53 (1963) 758-759.
- [212] P. Schiebener, J. Straub, J.M.H.L. Sengers, J.S. Gallagher. Refractive index of water and steam as function of wavelength, temperature and density. *J. Phys. Chem. Ref. Data* 19 (1990) 677-717.
- [213] D.R. Lide (Ed.) *CRC Handbook of Chemistry and Physics*, CRC Press/Taylor and Francis, Boca Raton, FL, 2009.
- [214] A. Erbe, R. Sigel. Tilt angle of lipid acyl chains in unilamellar vesicles determined by ellipsometric light scattering. *Eur. Phys. J. E* 22 (2007) 303-309.
- [215] P.N. Yi, R.C. MacDonald. Temperature dependence of optical properties of aqueous dispersions of phosphatidylcholine. *Chem. Phys. Lipids* 11 (1973) 114-134.
- [216] A.F. Behof, R.A. Koza, L.E. Lach, P.N. Yi. Phase transitions in phosphatidylcholine dispersion observed with an interference refractometer. *Biophys. J.* 22 (1978) 37-48.
- [217] H.J. van Staveren, C.J.M. Moes, J.v. Marie, S.A. Prahl, M.J.C. van Gemert. Light scattering in Intralipid-10% in the wavelength range of 400–1100 nm. *Appl. Opt.* 30 (1991) 4507-4514.

LIST OF TABLES

Table 1.1	Selected marketing authorization holding therapeutics employing colloidal carriers for drug delivery	05
Table 1.2	Key characteristics of colloidal drug carriers	06
Table 2.1	Effect of the drug-dependent electrostatic potential on measured apparent lipid membrane-water distribution coefficient, D	20
Table 2.2	The aqueous dissociation constants (pK_a) of tested drugs at 37 °C	22
Table 2.3	The lipid membrane-water partition coefficients of tested drugs at 37 °C	23
Table 3.1	The average diameter of the studied SPC vesicles, as determined with the dynamic light scattering	39
Table 3.2	The calculated bending rigidity, κ , of the mixed amphipat bilayers as a function of total cholate concentration	46
Table 3.3	The mixed aggregate composition, the corresponding aqueous cholate concentration, and the cholate partition coefficient into the mixed aggregates at the total cholate concentration ensuring complete soybean phosphatidylcholine solubilisation into small mixed micelles	57
Table 4.1	Characteristics of the simulated suspensions used to generate the spectra shown in Fig. 4.3	81
Table 4.2	Size characterization of the tested extruded lipid vesicles	88
Table 4.3	Different analytical methods sensitivity to changes in vesicle size distribution	90

LIST OF FIGURES

Figure 1.1	Development of selected colloidal aggregates of pharmaceutical interest as drug delivery carriers over the past five decades	03
Figure 2.1	Schematic illustration of dissociation and partitioning equilibria for acids and bases in a lipid membrane-water system	14
Figure 2.2	The apparent dissociation constant, pK_a^{app} , of acidic and basic drugs as a function of the lipid-aqueous compartment volumes ratio, r	19
Figure 2.3	Terbinafine and diclofenac apparent dissociation constant, pK_a^{app} , as a function of the lipid-aqueous compartment volumes ratio, r , at 37 °C and 150 mM bulk ionic strength	24
Figure 2.4	The effect of the drug-dependent Coulombic electrostatic interactions on the ionized drug form partitioning as a function of the drug-lipid molar ratio and the intrinsic partition coefficient of the ionized drug form, expressed as $\log P_0^{\text{I}}$	26
Figure 2.5	The effect of the bulk ionic strength on the ionized drug form apparent partition coefficient, P^{I} , modeled for a lipid-drug molar ratio of 5 at 37 °C	26
Figure 2.6	The effect of membrane charges on the apparent dissociation constant, pK_a^{app} , of bupivacaine and ketoprofen at 37 °C	28
Figure 3.1	The structural and chemical formula of a cholate molecule, showing the hydrophobic surface and the hydrophilic groups on the other molecular side ..	35
Figure 3.2	Upper panel: The quasi-steady state molar optical density of the mixed aggregate suspension resulting from the LUV after addition of sodium cholate to the given total concentration. Lower panel: The mean hydrodynamic diameter (quasi-steady state) of the mixed aggregates formed from the LUV after addition of sodium cholate to the given total concentration	41
Figure 3.3	Upper panel: The quasi-steady state molar optical density of the mixed aggregate suspension resulting from the SUV after addition of sodium cholate to the given total concentration. Lower panel: The mean hydrodynamic diameter (quasi-steady state) of the mixed aggregates formed from the SUV after addition of sodium cholate to the given total concentration	42

- Figure 3.4 Left panel: The quasi-steady state molar optical density of the mixed aggregate suspension resulting from the LUV, the IUV or the SUV after addition of sodium cholate to the given total concentration. Right panel: The derivative of the molar optical densities shown in the left panel vs. the total cholate concentration 43
- Figure 3.5 The temporal evolution of molar optical density of the LUV (left panel) or the SUV (right panel) suspensions after addition of sodium cholate to the given total concentration 44
- Figure 3.6 The cholate (total concentration = 0–2 mmol kg⁻¹) induced (mixed) vesicle hydrodynamic diameter changes 46
- Figure 3.7 Schematic representation of the most typical structures that can appear, and typically coexist, during progressive vesicle-to-micelle transformation 49
- Figure 3.8 Total cholate concentration required to solubilise the LUV bilayer vesicles into small mixed amphipat micelles as a function of total phospholipid (SPC) concentration 55
- Figure 3.9 The sum of two sigmoidal curves, described by Eqs. 3.19–3.20, can mimic all the basic forms of the experimental optical density vs. cholate concentration curves which we measured 65
- Figure 4.1 Effect of light scattering particle diameter (monodisperse) on the particle suspension turbidity (upper panels) and wavelength exponent (lower panels) spectra 77
- Figure 4.2 Effect of particle size distribution width on suspension turbidity (upper panel) and wavelength exponent (lower panel) spectra 79
- Figure 4.3 Turbidity (upper panel) and wavelength exponent (lower panel) spectra calculated for suspensions of homogeneous spheres with constant number concentration and variable geometric mean diameter and standard deviation. The suspensions have either identical turbidity (upper panel) or wavelength exponent (lower panel) at $\lambda = 600$ nm. The figure illustrates how quantitative analysis of turbidity or wavelength exponent spectra can resolve the mean diameter as well as the standard deviation 80

Figure 4.4	Influence of particle and dispersion medium refractive indices on suspension turbidity	82
Figure 4.5	Effect of spherical lipid bilayer thickness on turbidity (upper panel) and wavelength exponent (lower panel) of a monodisperse lipid vesicle suspension	84
Figure 4.6	Effect of lamellarity on turbidity (upper panel) and wavelength exponent (lower panel) of a suspension of monodisperse lipid vesicles	85
Figure 4.7	Vesicle diameter calculated from wavelength exponent spectra ($\lambda = 400\text{--}600$ nm) presuming unilamellarity as a function of the weight fraction of oligolamellar vesicles	86
Figure 4.8	Effect of sodium cholate concentration on size of extruded lipid vesicles (preparation V80 and V50), as measured with turbidity spectroscopy relying on wavelength exponent analysis or with the dynamic light scattering	91
Figure 4.9	The error contour chart for the scattering coefficient, Q_{sca}	93

Erklärung

Hiermit erkläre ich, dass ich mich mit der vorliegenden Arbeit erstmals um die Erlangung eines Doktorgrades bewerbe.

Ferner erkläre ich, dass ich die vorliegende Arbeit selbständig und ohne fremde Hilfe verfasst, andere als die von mir angegebenen Quellen und Hilfsmittel nicht benutzt und die den benutzten Werken wörtlich oder inhaltlich entnommenen Stellen als solche kenntlich gemacht habe.

Halle (Saale), Februar 2011

Mustafa Elsayed

Acknowledgement

Praise is first due to Allah for guiding me, supporting me, and giving me the power to do this work. Allah! May this thesis be helpful to others.

I would like to express my deepest gratitude and sincere appreciation to Prof. Dr. Gregor Cevc for offering me the chance to join IDEA AG and to work under his supervision. I can not forget his whole-hearted guidance, sincere concern, and fruitful discussions throughout the course of my PhD study. Many thanks for giving me the opportunity to improve my skills, broaden my knowledge, and develop my carrier. Thanks for your trust, your confidence and your never-ending encouragement and moral support.

I am also greatly indebted to Prof. Dr. Dr. Reinhard Neubert for his willingness to accept me as a PhD student, his continuous willingness to help whenever I approach him, the encouraging discussions, the academic support, and the guidance on finishing this thesis.

Many thanks to my colleagues in IDEA AG, especially Dr. Christian Wachter, Dr. Ulrich Vierl, and Markus Koschlig, for their cooperation, valuable suggestions, kind help, and support.

Special thanks to my wife Ghada and my son Muadh for sharing this 'adventure' with me with fascinating courage and patience and for bearing my hard times, my sadness, and my nervousity.

My everlasting gratitude goes to my great father and my great mother. Anything I achieve in my life is a result of their sacrifice in raising me. I remain indebted to them throughout my wholelife. Many thanks to my whole family for the encouragement, love, and kind support.

I would like also to thank my dear professors, friends and colleagues back home in the Department of Pharmaceutics, Faculty of Pharmacy, Alexandria University, Egypt, for encouragement and continuous support. Special thanks to Prof. Dr. Nawal Khalafallah, who prepared me and put me on the track. You share part in every success I achieve here in Germany and in my whole life, with all what I learned from you, your guidance, and support.

I gratefully acknowledge IDEA AG for the financial support and for giving me the chance to conduct this scientific work.

To everyone who helped me throughout the course of my PhD study and who is not mentioned, please forgive me and accept my respect, appreciation, and thanks.

Mustafa Elsayed

Halle (Saale), February 2011

Curriculum Vitae

1. Personal information:

Name: **Mustafa Mohammed Abdelaziz Elsayed**

Birth date: 13 July 1981.

Place of birth: Alexandria, Egypt.

Nationality: Egyptian.

Address: Department of Pharmaceutics, Faculty of Pharmacy, Alexandria University, El-Khartoum Square, El-Azarita, Alexandria 21521, Egypt.

E-mail address: mus.elsayed@gmail.com

2. Education:

2004 – 2006 Master degree of Pharmaceutical Sciences (Pharmaceutics), Faculty of Pharmacy, Alexandria University, Egypt.
Thesis title: A pharmaceutical study of some vesicular drug delivery systems.

1998 – 2003 Bachelor of Pharmaceutical Sciences, Faculty of Pharmacy, Alexandria University, Egypt, Grade: Distinction Honour.

3. Professional Experience:

08.2007 – 10.2010 Scientist / Ph.D. Student, IDEA AG, München, Germany

10.2006 – 08.2007 Assistant lecturer, Department of Pharmaceutics, Faculty of Pharmacy, Alexandria University, Alexandria, Egypt.

01.2004 – 09.2006 Teaching assistant, Department of Pharmaceutics, Faculty of Pharmacy, Alexandria University, Alexandria, Egypt.

List of publications:

1. M.M.A. Elsayed, G. Cevc. Turbidity spectroscopy for characterization of submicroscopic drug carriers, such as nanoparticles and lipid vesicles: Size Determination. *Pharm. Res.* In press.
<http://dx.doi.org/10.1007/s11095-011-0448-z>
2. M.M.A. Elsayed, G. Cevc. The vesicle-to-micelle transformation of phospholipid–cholate mixed aggregates: A state of the art analysis including membrane curvature effects. *Biochim. Biophys. Acta* 1808 (2011) 140–153.
<http://dx.doi.org/10.1016/j.bbamem.2010.09.002>
3. M.M.A. Elsayed, U. Vierl, G. Cevc. Accurate potentiometric determination of lipid membrane-water partition coefficients and apparent dissociation constants of ionizable drugs: Electrostatic corrections. *Pharm. Res.* 26 (2009) 1332–1343.
<http://dx.doi.org/10.1007/s11095-009-9842-1>
4. M.M.A. Elsayed, O.Y. Abdallah, V.F. Naggar, N.M. Khalafallah. PG-liposomes: Novel lipid vesicles for skin delivery of drugs. *J. Pharm. Pharmacol.* 59 (2007) 1447–1450.
<http://dx.doi.org/10.1211/jpp.59.10.0017>
5. M.M.A. Elsayed. Rapid determination of cinchocaine in skin by high-performance liquid chromatography. *Biomed. Chromatogr.* 21 (2007) 491-496.
<http://dx.doi.org/10.1002/bmc.782>
6. M.M.A. Elsayed, O.Y. Abdallah, V.F. Naggar, N.M. Khalafallah. Lipid vesicles for skin delivery of drugs: Reviewing three decades of research. *Int. J. Pharm.* 332 (2007) 1-16.
<http://dx.doi.org/10.1016/j.ijpharm.2006.12.005>
7. M.M.A. Elsayed, O.Y. Abdallah, V.F. Naggar, N.M. Khalafallah. Deformable liposomes and ethosomes as carriers for skin delivery of ketotifen. *Pharmazie* 62 (2007) 133-137.
<http://dx.doi.org/10.1691/ph.2007.2.6082>
8. M.M.A. Elsayed, O.Y. Abdallah, V.F. Naggar, N.M. Khalafallah. Deformable liposomes and ethosomes: Mechanism of enhanced skin delivery. *Int. J. Pharm.* 322 (2006) 60-66.
<http://dx.doi.org/10.1016/j.ijpharm.2006.05.027>

9. M.M.A. Elsayed. Development and validation of a rapid HPLC method for the determination of ketotifen in pharmaceuticals. *Drug Dev. Ind. Pharm.* 32 (2006) 457-461.

<http://dx.doi.org/10.1080/03639040500529135>

Poster presentations:

1. M.M.A. Elsayed, U. Vierl, G. Cevc. Accurate potentiometric determination of lipid membrane-water partition coefficients and apparent dissociation constants of ionizable drugs: Electrostatic corrections. Poster, The 4th LogP Symposium: PhysChem and ADMET Profiling in Drug Research, February 8-11, 2009, ETH Zürich, Switzerland.